Modeling and Control of Tensegrity-Membrane Systems

Shu Yang

Dissertation submitted to the faculty of the Virginia Polytechnic Institute and State University in partial fulfillment of the requirements for the degree of

Doctor of Philosophy

In

Aerospace Engineering

Cornel Sultan, Chair

Craig A. Woolsey

Rakesh K. Kapania

Mazen H. Farhood

March 23, 2016

Blacksburg, Virginia

Keywords: tensegrity-membrane systems, nonlinear finite element model, control-oriented model, nonlinear adaptive control, linear parameter-varying control

Modeling and Control of Tensegrity-Membrane Systems

Shu Yang

ABSTRACT

Tensegrity-membrane systems are a class of new bar-tendon-membrane systems. Such novel systems can be treated as extensions of tensegrity structures and are generally lightweight and deployable. These two major advantages enable tensegrity-membrane systems to become one of the most promising candidates for lightweight space structures and gossamer spacecraft.

In this dissertation, modeling and control of tensegrity-membrane systems is studied. A systematic method is developed to determine the equilibrium conditions of general tensegrity-membrane systems. Equilibrium conditions can be simplified when the systems are in symmetric configurations. For one-stage symmetric systems, analytical equilibrium conditions can be determined.

Three mathematical models are developed to study the dynamics of tensegrity-membrane systems. Two mathematical models are developed based on the nonlinear finite element method. The other model is a control-oriented model, which is suitable for control design. Numerical analysis is conducted using these three models to study the mechanical properties of tensegrity-membrane systems.

Two control strategies are developed to regulate the deployment process of tensegrity-membrane systems. The first control strategy is to deploy the system by a nonlinear adaptive controller and use a linear H_∞ controller for rapid system stabilization. The second control strategy is to regulate the dynamics of tensegrity-membrane systems using a linear parameter-varying (LPV) controller during system deployment. A gridding method is employed to discretize the system operational region in order to carry out the LPV control synthesis.

Acknowledgement

I would like to thank my advisor Dr. Cornel Sultan for the guidance and support he provided throughout my research. Also my other committee members, Dr. Craig Woolsey, Dr. Rakesh Kapania, and Dr. Mazen Farhood, gave priceless advice and contributed in many ways to the improvement of my work.

This work is supported by the National Science Foundation (NSF) under the grant CMMI-0952558. I would like to express my gratitude to NSF for the financial support.

Table of Contents

List of Tables

List of Figures

Chapter 1: Introduction

1.1. Motivation

1.1.1. Gossamer Spacecraft

The space exploration era opened up multiple opportunities for lightweight space structures and gossamer spacecraft, which have excited researchers' interest. The primary driver behind this interest is the growing need of introducing lighter and much less expensive space structures that can be packaged in much smaller volume. A major survey work published in 1995 is the paper of Cassapakis and Thomas [1]. These researchers discussed topics such as design variable selection for large, inflatable spacecraft, considerations on new deployment and rigidization techniques, and multiple applications for large, inflatable spacecraft. Most importantly, they discussed the lessons learned from their research and mentioned the areas of research deserving further attention and the technologies needed for the future development of space inflatable structures. Pappa et al. [2] reported completed structural dynamics experimental activities of gossamer space structures performed by researchers at NASA Langley Research Center, Marshall Space Flight Center, and Goddard Space Flight Center. The survey work covered research topics such as inflatable/rigidizable tubes, tensioned membranes, active control experiments, modal tests, and deployment tests. Issues and difficulties related to ground testing of ultra-lightweight and inflatable spacecraft were discussed, as well as the need of nontraditional structural measurement approaches to understand the dynamical responses of gossamer-type structures. A recent survey work on gossamer spacecraft was conducted by Ruggiero and Inman [3]. They discussed the recent trends in gossamer spacecraft design and

analysis, advances in experimental analysis, and the development of membrane mirror technology. Moreover, they reported and discussed the advances in membrane wrinkle analysis and gossamer control systems.

Membranes are key components in gossamer spacecraft. The major benefit that membranes offer is the possibility of introducing system components of large dimensions and low mass into spacecraft. Therefore, membranes in gossamer spacecraft usually serve as solar sail surfaces, mirrors, reflectors, and antennas. In general, ultra-lightweight solar sails for deep space satellite propulsion, large spacecraft optics, and space-based antennas are the three major areas of gossamer spacecraft research.

Since the propulsion efficiency of solar sails depends on a very low ratio of overall spacecraft mass to solar sail area, in-orbit deployable, ultra-lightweight sail surfaces are required. Greschik and Mikulas [4] presented a design study of square solar sails. They compared their novel sail suspension design, named stripped sail architecture, to other sail design concepts, like the four- and five-point sail suspension architecture and the sail design of separate quadrants. Several observations related to design efficiency and structural economy and issues of sail structure design and analysis were concluded and discussed. Mikulas and Adler [5] provided a simplified approach for assessing square solar sails in a preliminary design procedure. Kukathasan and Pellegrino [6] studied the vibration of tensioned membranes, showing the feasibility of simplifying the ground testing of large deployable membrane structures by performing the finite element analysis introduced in their work. Air effects on membranes were included in the analysis. Kukathasan and Pellegrino [7] conducted a high-fidelity finite element simulation for wrinkled membranes using thin-shell elements and a very careful simulation of the static wrinkling process. They found that using unwrinkled membrane model could accurately predict

the vibration of a moderately wrinkled membrane, but not of a heavily wrinkled membrane, both in vacuum and in air. Adetona et al. [8] designed and developed a hexapod structure with a tensioned membrane as a test bed to study the issues of large inflatable structures, such as static shape control of membranes and vibration mitigation. Adetona et al. [9] and Berger et al. [10] followed up their previous work by conducting static testing and vibration studies of the hexapod structure. Leipold et al. [11] presented the development and demonstration of solar sail technology by DLR and ESA.

Because of the similarity between solar sails and space antennas, many design aspects and technological solutions developed for solar sails can be transferred to applications involving large microwave membrane antennas. For example, inflatable membrane structures were designed as large space-based reflectarray antennas [12]. Leipold et al. [13] reported a concept for SAR membrane antennas. This concept originated from the solar sail development technology developed by ESA, DLR, and the company Kayser-Threde.

Most membrane structures were studied merely to exploit their lightweightness in the deployed configurations. Only a few researchers studied system deployment. Deployment is the process of changing system configurations, which is a key requirement for space structures. Pellegrino [14] designed and tested a deployable membrane reflector consisting of a central expandable hub, thin-walled foldable ribs, and a precision-shaped membrane. Its deployment behavior was measured experimentally and it only took 1.3 seconds to complete the deployment process. The Air Force Research Laboratory Space Vehicles Directorate has developed multiple deployable architectures including a boom utilizing rollable composite tape spring members [15-17]. Footdale et al. [18] designed and studied a freely-deploying support structure which positions and tensions a membrane primary optic. The deployment of the membrane optic

support structure was implemented by rollable composite tape spring members. The experimental tests showed that the deployment duration was very short (approximately 0.65 seconds). These researchers indicated that the high deployment rate introduces rapid deceleration on the membrane. Therefore, the deployment rate should be better controlled and the related control techniques need to be studied.

Most membrane systems studied and implemented to date are structures with membranes installed on support frames. The primary objective of designing these structures is to determine the shape and behavior of membranes under certain tensile forces [19-21]. Cables are usually attached to the edges of membranes in order to achieve certain stress distributions in membranes. These systems are called "catenary systems" for membranes. The inflatable membrane structures [12], as well as some tensioned fabric roofs [22] and tents, belong to this type of structures. Therefore, the mechanical behavior of these systems is mainly determined by the support frame and membranes have little effect on the statics and dynamics of the support frame and the whole system. This fact simplifies system design, since the frame and the membrane can be designed separately and each design problem can be solved by the well-developed design and analysis methods in structural mechanics and solid mechanics. However, to change the configurations of these traditional membrane systems it is necessary to change the shape of the support frames. Thus, numerous additional components, such as actuators and rigid/flexible mechanical connecting parts, are usually required for *rigid* support frames to actively control system components and to achieve system deployment. As a result, system weight increases, diminishing the benefit of lightweightness due to the membranes. Moreover, the resulting systems turn out to be more complex, leading to higher risk of deployment failure [23]. To alleviate these problems, some space membrane system designs employ the inflation technology,

leading to systems with membranes attached to *inflatable* support frames. Such systems are free from mechanical connecting parts, like hinges and joints, but system configurations during inflation may not be accurately controlled. Therefore, additional control devices are required to achieve precise control of system components during deployment [24]. It should also be noted that the design separation concept used for traditional space membrane systems may not give a comprehensive understanding of the behavior of the whole system. Additional analyses/experiments and sophisticated models are required to study the coupling between system components and to examine whether undesired coupled dynamics is introduced.

1.1.2. Tensegrity-Membrane Systems

The main goal of this work is to present a comprehensive study of a class of bar-tendon-membrane structures that we call "tensegrity-membrane systems". The key idea of creating such novel structures is to introduce membranes in tensegrity structures. There are several motivations behind this innovation that originate in the field of biology and engineering. It has long been established and accepted by biologists that tensegrity architectures are fundamental design principles selected via natural evolution [25]. Assemblies of bones, tendons, and muscles are encountered in micro and marco organisms, resembling tensegrity. It has been found that tensegrity models can accurately describe the mechanics of a number of biological structures, such as cell cytoskeletons [26] and red blood cell membranes [27]. On the other hand, mechanical behaviors of tensegrity structures also draw researchers' attention. Some mechanical properties of tensegrity structures are employed to solve engineering problems. Skelton [28] showed that a tensegrity structure can be designed optimally strong and stiff through suitable adjustment of the prestress of tensile members and these tensile members may serve as sensors or actuators. Fraternali et al. [29] explored the use of tensegrity prisms as networks supporting

energy transport through solitary waves. Fraternali et al. [30] further studied the nonlinear behavior of tensegrity prisms under axial loads. What makes tensegrity special compared to other bar-tendon assemblies are their infinitesimal mechanisms that are stiffened by tendon pretension. Sultan [31] showed the feasibility of using this unique mechanical property to deploy tensegrity structures.

It has been shown by many researchers that tensegrity systems are generally lightweight and easy to deploy [32-35]. Significant efforts have been expended on applying tensegrity systems in the field of lightweight space system design. Successful applications, for example tensegrity masts [36] and tensegrity reflectors [37], have been studied and reported, which illustrate the possibility of designing deployable lightweight spacecraft based on tensegrity systems.

As extensions of classical tensegrity systems, tensegrity-membrane systems inherit most of the advantages of tensegrity structures and can meet the requirements of lightweightness and deployment capacity at the same time. This fact makes tensegrity-membrane systems one of the most promising candidates for gossamer spacecraft and lightweight space structures. Moreover, the attached membranes contribute tensile forces to the whole system and play a similar role to the tendons in tensegrity systems. This feature complicates the design of tensegrity-membrane systems, since system design has to be performed for the whole system, including bars, tendons, and membranes. For mechanics studies on a tensegrity-membrane system, the attached membrane cannot be separated from the rest of the structure compared to traditional membrane systems discussed previously.

With rigid bars included, stiffness properties of tensegrity-membrane systems are improved, so the shape and motion of tensegrity-membrane structures can be controlled accurately, for example, by changing the rest-lengths of tendons. Other strategies for deployment which use

telescopic struts can be implemented [37]. However, they are complex, usually lead to slack tendons and introduce significant damping. Compared with these methods, tendon force/rest-length control can make deployable structures free from these issues [38].

Modeling and control of tensegrity-membrane systems is a very recent research topic. Actually, in contrast with the literature on tensegrity systems, the literature on tensegrity-membranes is very limited because these are very recent, emerging structural systems. The paper of Sunny et al. [39] was the first study on tensegrity-membrane systems, where a passive one-stage tensegrity-membrane system with four bars was studied. Those researchers primarily investigated the feasibility of harvesting energy from such a passive system with piezoelectric transducers attached to the membrane. However, there was no comprehensive discussion on the mechanics of tensegrity-membrane systems.

1.2. Research Objectives and Contributions

The research objectives of this work are: 1) to study the equilibrium conditions of tensegrity-membrane systems, 2) to develop mathematical models of tensegrity-membrane systems, and 3) to develop control strategies for system control and deployment.

The major contributions of this dissertation are listed as follows:

1) A systematic method is developed to determine the equilibriums of tensegrity-membrane systems.

2) Explicit equilibrium conditions of symmetric tensegrity-membrane systems are derived.

3) Two nonlinear finite element models and a control-oriented model are developed to study the dynamics of tensegrity-membrane systems.

4) Two control strategies are designed for system deployment: a nonlinear adaptive controller combined with an H_∞ controller and a linear parameter varying (LPV) controller.

1.3. Outline of Dissertation

The outline of this dissertation is as follows. Descriptions of tensegrity-membrane systems and the modeling assumptions used in this work are presented in Chapter 2. A systematic method of finding the equilibriums of tensegrity-membrane systems is developed in Chapter 3. This method is first used to determine the equilibrium conditions for general tensegrity-membrane system. Then, it is shown that the equilibrium conditions can be significantly simplified when tensegrity-membrane systems are in symmetric configurations. In Chapter 4, two nonlinear finite element models of tensegrity-membrane systems are developed. These two models are referred to as the shell-beam-cable model and the membrane-truss-cable model, respectively. In Chapter 5, the development of a control-oriented model for tensegrity-membrane systems is presented. The resulting equations of motion are a set of differential-algebraic equations. A coordinate partitioning and coordinate mapping method is used to convert the differential-algebraic equations of motion to a set of ordinary differential equations. In Chapter 6, numerical analysis is conducted to study the mechanical properties of tensegrity-membrane systems using the three mathematical models developed in this work. In Chapter 7, a nonlinear control strategy is developed for system deployment. A nonlinear adaptive controller is used to deploy tensegrity-membrane systems and an H_∞ controller is used for rapid system stabilization. In Chapter 8, the development of a linear parameter-varying controller for system deployment is discussed. Finally, conclusions of the work and a discussion of future work are presented in Chapter 9.

Chapter 2: System Description and Modeling Assumptions

2.1. Introduction

Tensegrity-membrane systems are created by introducing membranes into classical tensegrity systems. Such systems are complex assemblies of tendons, bars, and membranes. The assembly pattern of system components should be studied and defined, since different component assembly patterns will result in different systems with different properties. In this chapter, detailed descriptions of tensegrity-membrane systems are first presented. Then, the modeling assumptions which are used for model development are introduced and discussed.

2.2. Physical System Description

A tensegrity-membrane system is defined as a prestressed system composed of bars, tendons, and membranes. In this work, we focus on a generic tensegrity-membrane system with M stages, N bars in each stage, and one membrane attached to the top of the system. This system is referred to as an M-N tensegrity-membrane system. The bars are labeled b_{ij} and a stage contains the bars with the same first index. For the j-th bar in the i-th stage, i.e. b_{ij}, the lower end and the upper end of the bar b_{ij} are labeled A_{ij} and B_{ij}, respectively. The length of bar b_{ij} is labeled l_{ij}.

The system is located at a fixed base by connecting the lower ends of the bars in the first stage to the base through frictionless rotational joints. The membrane is attached on the top of the system and the membrane corners are connected to the upper ends of the bars in the M-th stage.

To illustrate the shape of tensegrity-membrane systems, a tensegrity-membrane system with one stage and four bars in the stage (a 1-4 system) is depicted in Figure 2.1.

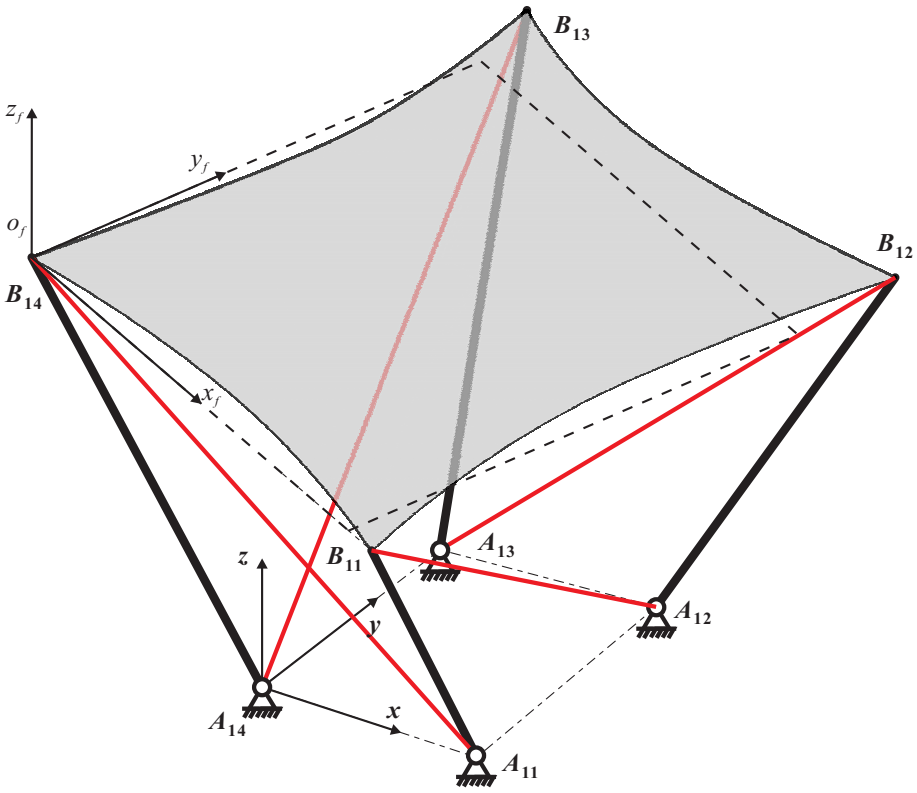

Figure 2.1. The sketch of a one-stage four-bar tensegrity-membrane system

For the 1-4 system in Figure 2.1, it can be seen that after replacing the membrane with 4 tendons $B_{11}B_{12}$, $B_{12}B_{13}$, $B_{13}B_{14}$, and $B_{14}B_{11}$, the tensegrity-membrane system can be converted to a tensegrity system (see Figure 2.2). In other words, the attached membrane plays a similar role in a tensegrity-membrane system as the tendons connecting the upper ends of bars in a tensegrity system. Moreover, when prestressed the membrane adds more tension to the system. It is also in agreement with the classical definition of a tensegrity system [40-42] as a system in which tension provides integrity to the system. Therefore, tensegrity-membrane systems share the same concept of tensegrity systems and can be

treated as extensions of tensegrity systems. Hence, the denomination "tensegrity-membrane system" is used here.

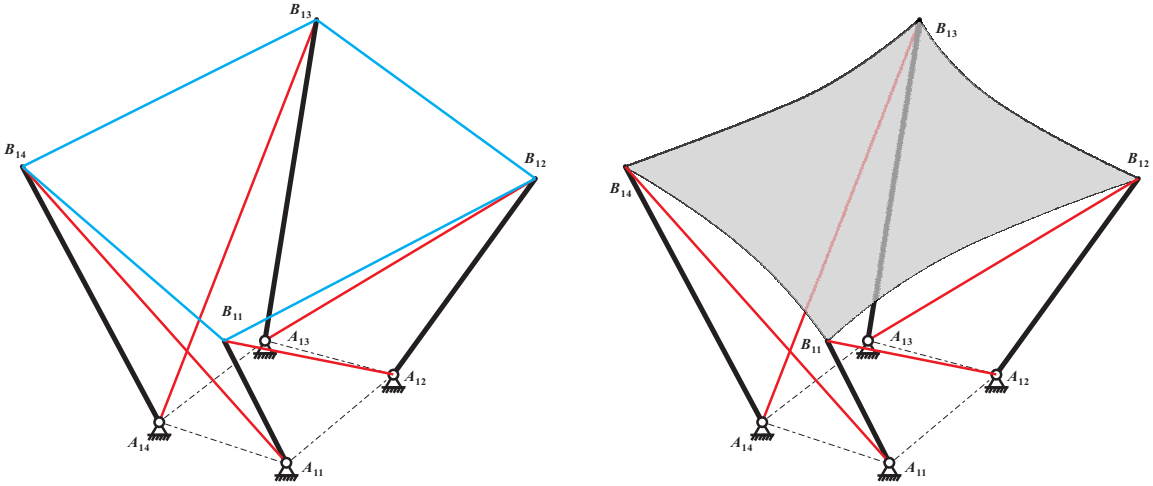

Figure 2.2. The sketch of a tensegrity system and a tensegrity-membrane system

The inertial reference frame *O-xyz* is fixed at the base where the system is located. The origin of *O-xyz* is located at point A_{1N}. The *Ox* axis goes through point A_{1N} and A_{11}. The *Oy* axis is perpendicular to the *Ox* axis in the base plane. The *Oz* axis is perpendicular to *O-xy* plane, determined by the right-hand rule.

The tendons of a tensegrity-membrane system can be classified into 6 different types based on the connection pattern, as shown in Figure 2.3:

a) Tendon S_{ij} connects the bar ends A_{ij} and $B_{i,\,j\text{-}1}$

b) Tendon V_{ij} connects the bar ends A_{ij} and $B_{i\text{-}1,\,j+1}$

c) Tendon D_{ij} connects the bar ends A_{ij} and $B_{i\text{-}1,\,j\text{-}1}$

d) Tendon C_{ij} connects the bar ends A_{ij} and $A_{i\text{-}1,\,j\text{-}1}$

e) Tendon P_{ij} connects the bar ends B_{ij} and $B_{i\text{-}1,\,j}$

f) Tendon R_{ij} connects the bar ends B_{ij} and $B_{i\text{-}1,\,j\text{-}1}$

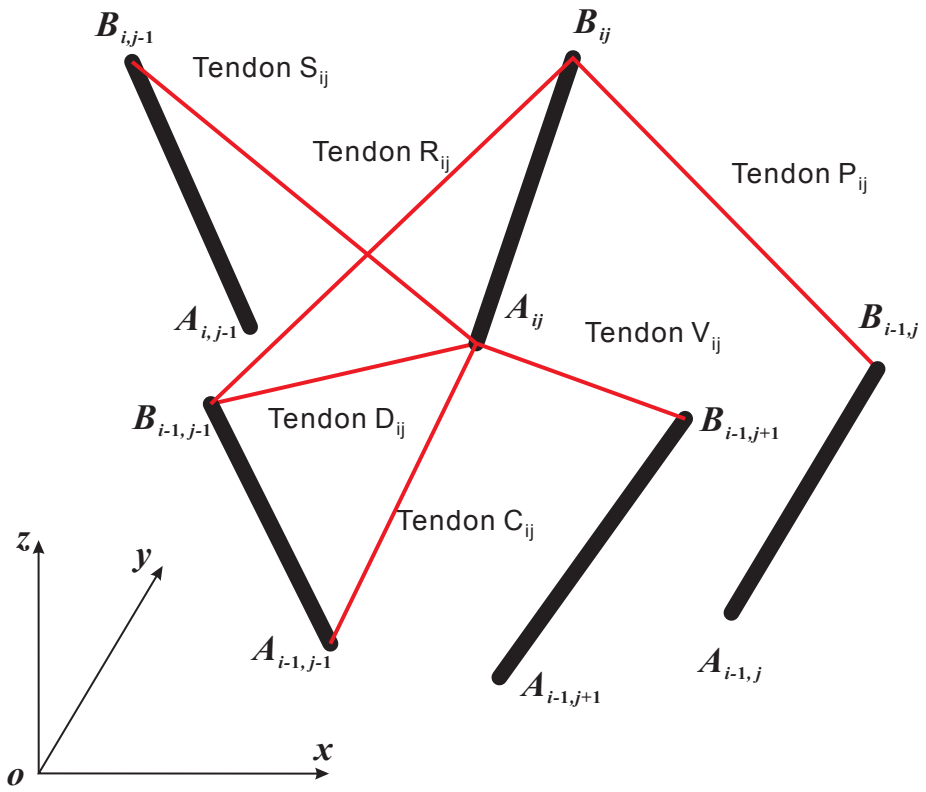

Figure 2.3. Tendon connection pattern of *M*-*N* systems

When $M = 1$, i.e. for a one-stage system, there are only N tendons in the system. Note that, if the rotational motion of each bar about its longitudinal axis is ignored, the attitudes of the bars in a one-stage system can be determined by $2N$ generalized coordinates. Clearly, if the control elements are all of the N tendons, the control authority provided by these tendons might be limited. Therefore, a new tendon connection pattern is introduced for one-stage systems. The resulting systems are referred to as 1-*N*(D) systems.

The tendon connection pattern of a 1-*N*(D) system, shown in Figure 2.4, is defined as follows:

a) Tendon SL_j connects A_{1j} and $H_{1,j-1}$

b) Tendon SU_j connects B_{1j} and $H_{1,j-1}$

The point H_{1j} is located on the j-th bar. The distance from the A_{1j} to H_{1j} is $k_H l_{1j}$ ($0 < k_H < 1$).

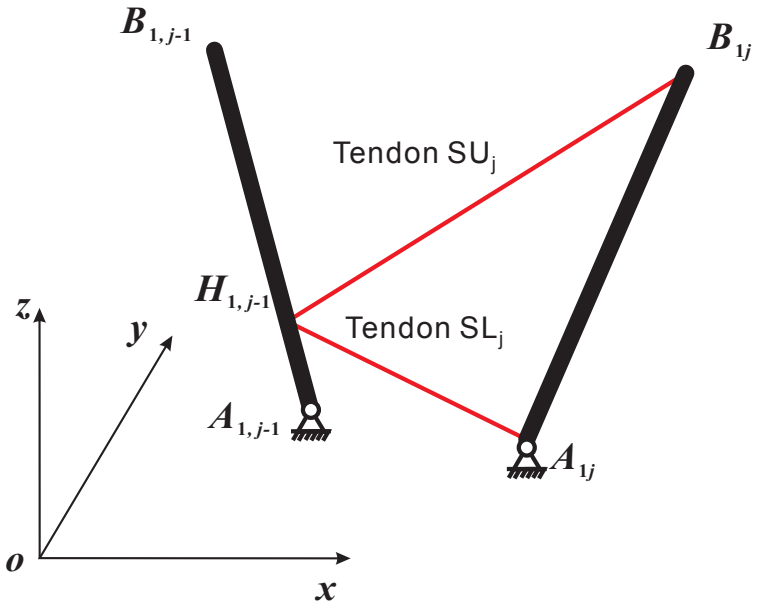

Figure 2.4. Tendon connection pattern of 1-N(D) systems

2.3. Modeling Assumptions

The basic modeling assumptions used in this work are as follows:

a) Linear elastic constitutive laws are used for the attached membranes, the bars, and the tendons.

b) The gravitational field is ignored. No external force is applied to the system.

c) A homogeneous membrane in the shape of a convex polygon in the undeformed configuration is used.

d) Tendons and membranes cannot be compressed (i.e. they can carry only tensile loads).

Modeling assumptions listed above are general assumptions for tensegrity-membrane systems, which will be strictly followed in this work. Note that specific modeling assumptions can be also made for each system component based on its mechanical properties. Implementing different specific modeling assumptions for system components leads to different mathematical models.

For the attached membranes, we can model them as thin shells. This is a modeling assumption of great generality, since membrane thickness, membrane curvature, and the transverse bending and shear stiffness are all taken into account. Therefore, this assumption can be used when the membrane thickness is not uniform or membranes are affected by bending moments. However, it should be noted that membranes used in practice are generally very thin. Thus, their transverse bending stiffness and transverse shear stiffness can be ignored, which is a commonly used modeling assumption in most work on membrane design and analysis.

It is also important to remark that different modeling assumptions can be used for bars. On one hand, the bars can be assumed to be rigid bodies. This is a widely used assumption in most research work on tensegrity systems [34]. On the other hand, we can treat bars as flexible bodies by either modeling them as rods or treating them as beams.

For the tendons in tensegrity-membrane systems, considering tendon dynamics will yield a general mathematical model of tensegrity-membrane systems, since the contribution of tendons to the dynamics of the whole system can be examined. Note that tendons are usually much lighter than bars and membranes. Thus, we may ignore the dynamics of tendons for simplicity.

In this work, specific modeling assumptions for system components used for three different mathematical models are as follows:

Shell-beam-cable model: membranes are modeled as shells; bars are modeled as beams; the dynamics of tendons is considered.

Membrane-truss-cable model: the transverse bending stiffness and the transverse shear stiffness of membranes are ignored; bars are modeled as rods; the dynamics of tendons is considered.

Control-oriented model: the transverse bending stiffness and the transverse shear stiffness of membranes are ignored; bars are treated as rigid bodies; the dynamics of tendons is ignored.

It can be seen that the shell-beam-cable model is a general mathematical model for tensegrity-membrane systems, since there is no specific modeling assumptions introduced for system components to simplify the modeling problem. Thus, the shell-beam-cable model can be treated as an effective tool for studying mechanical properties of tensegrity-membrane systems and validating other simplified mathematical models.

2.4. Conclusions

In this chapter, the detailed descriptions of tensegrity-membrane systems are presented. Since tensegrity-membrane systems are composed of bars, tendons, and membranes, the component assembly pattern, especially the tendon connection pattern, is discussed in detail. Modeling assumptions, which are used for different mathematical models, are introduced and discussed. These assumptions will be strictly followed in the model development for tensegrity-membrane systems in the following chapters.

Chapter 3: Equilibrium Conditions of Tensegrity-Membrane Systems

3.1. Introduction

Tensegrity-membrane systems are prestressed systems. The characterization of system's equilibrium configurations is the prerequisite for system design and system analysis. In this chapter, a systematic method is used to study the static configurations of tensegrity-membrane systems. The total strain energy of a tensegrity-membrane system consists of two parts: the strain energy of the tensioned membrane and the strain energy stored in tendons. After implementing the principle of virtual work, the equilibrium conditions of the system can be determined. It is also shown that the resulting equilibrium conditions can be further simplified if the systems are in symmetric configurations.

3.2. Equilibrium Conditions for General Systems

Since bars are generally very rigid compared with membranes and tendons, rigid body assumption is used for bars to study the equilibrium conditions of a generic tensegrity-membrane system. The rotational motion of each bar about its longitudinal axis is also ignored for simplicity. Therefore, for bar b_{ij} ($i \geq 2$), five generalized coordinates x_{ij}, y_{ij}, z_{ij}, θ_{ij}, and ψ_{ij} are used to determine its position and attitude. For bar b_{1j}, only two generalized coordinates θ_{1j} and ψ_{1j} are needed. The coordinates x_{ij}, y_{ij}, and z_{ij} are the coordinates of the bar's lower end A_{ij}. The declination angle θ_{ij} is measured from the Oz axis to the bar b_{ij}. The azimuth angle ψ_{ij} is measured from the Ox axis to the projection of

the bar on the base. Note that $\theta_{ij} \in (0, \pi/2)$ and $\psi_{ij} \in (-\pi, \pi)$. The generalized coordinates of bar b_{ij} are shown in Figure 3.1.

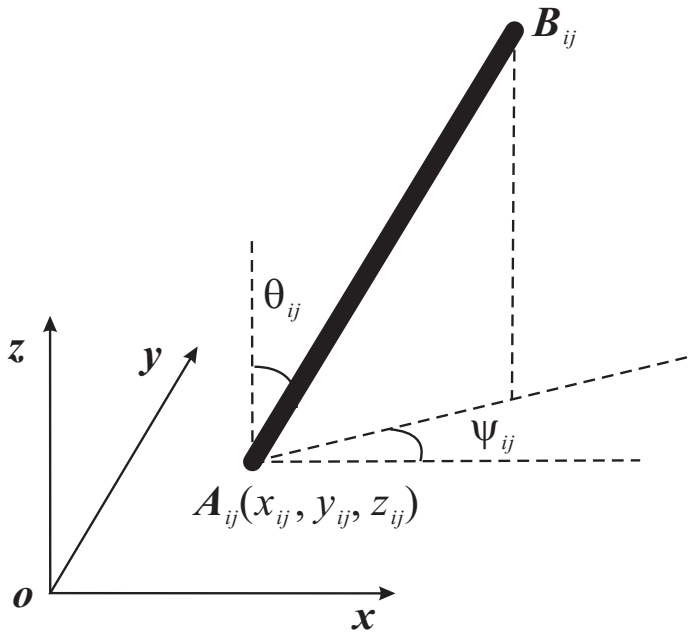

Figure 3.1. Generalized coordinates of bar b_{ij}

The generalized coordinates for the locations and attitudes of bars are:

$$\boldsymbol{q} = \left[\boldsymbol{q}_{11}{}^T \quad \cdots \quad \boldsymbol{q}_{1N}{}^T \quad \boldsymbol{q}_{21}{}^T \quad \cdots \quad \boldsymbol{q}_{MN}{}^T \right]^T \tag{3.1}$$

where

$$\begin{aligned} \boldsymbol{q_{1j}} &= \left[\theta_{1j} \quad \psi_{1j} \right]^T; \quad (j = 1, 2, \ldots N) \\ \boldsymbol{q_{ij}} &= \left[x_{ij} \quad y_{ij} \quad z_{ij} \quad \theta_{ij} \quad \psi_{ij} \right]^T; \quad (i = 2, 3, \ldots M; \quad j = 1, 2, \ldots N) \end{aligned} \tag{3.2}$$

Here $\boldsymbol{q_{1j}}$ is the vector of the generalized coordinates for the j-th bar in the first stage and $\boldsymbol{q_{ij}}$ is the vector of the generalized coordinates for the j-th bar in the i-th stage ($i \geq 2$). Since tendons connect the lower and upper ends of bars, tendon lengths can be expressed as functions of $\boldsymbol{q}$.

The displacement boundary conditions of the membrane can be fully determined by the location of B_{Mi}, since the membrane corners are attached to the upper ends of bar b_{Mi}. To facilitate the analysis of the membrane, we will release the displacement constraints at membrane corners B_{Mi} (i = 2, 3, ..., N), then apply these constraints. To carry out the analysis, we first introduce a floating reference frame labeled O_f-$x_fy_fz_f$.

The origin of O_f-$x_fy_fz_f$ is located at B_{MN}, i.e. $O_f \equiv B_{MN}$. The plane O_f-x_fy_f is identical with the plane determined by B_{MN}, B_{M1}, and $B_{M,\,N\text{-}1}$. The axis O_fx_f goes through B_{MN} and B_{M1}. The axis O_fy_f is perpendicular to O_fx_f. The O_fz_f axis can be determined based on the right-hand rule. According to the definition, O_f-$x_fy_fz_f$ is fixed on the undeformed membrane. The floating reference frame O_f-$x_fy_fz_f$ for a 1-4 tensegrity membrane system is depicted in Figure 2.1. For each generic point P on the membrane, three variables u, v, and w are used to describe its deflections in the O_fx_f, O_fy_f, and O_fz_f axes.

A 3-2-1 Euler angle sequence [43] is used to convert coordinates from the inertial frame O-xyz to the floating frame O_f-$x_fy_fz_f$. This gives the rotation matrix $\boldsymbol{R}^{fe}$. The corresponding rotation matrix $\boldsymbol{R}^{ef}$ is:

$$\boldsymbol{R}^{ef} = \left(\boldsymbol{R}^{fe}\right)^T = \begin{bmatrix} \cos\gamma_1\cos\gamma_2 & \cos\gamma_1\sin\gamma_2\sin\gamma_3 - \cos\gamma_3\sin\gamma_1 & \cos\gamma_1\cos\gamma_3\sin\gamma_2 + \sin\gamma_1\sin\gamma_3 \\ \cos\gamma_2\sin\gamma_1 & \cos\gamma_1\cos\gamma_3 + \sin\gamma_1\sin\gamma_2\sin\gamma_3 & \cos\gamma_3\sin\gamma_1\sin\gamma_2 - \cos\gamma_1\sin\gamma_3 \\ -\sin\gamma_2 & \cos\gamma_2\sin\gamma_3 & \cos\gamma_2\cos\gamma_3 \end{bmatrix} \quad (3.3)$$

In the O_f-$x_fy_fz_f$ frame, the displacement boundary conditions of the membrane are: a) B_{M1} is free in O_fx_f axis, b) $B_{M,\,N\text{-}1}$ is free in O_fx_f and O_fy_f axes, and c) B_{Mi} (i = 2, 3, ..., N−2) are free in O_fx_f, O_fy_f and O_fz_f axes. Therefore, we introduce coordinates associated with the membrane corners expressed in the O_f-$x_fy_fz_f$ frame, named membrane corner displacements. These corner displacements of the membrane are labeled Δ_{ui}, Δ_{vi}, and Δ_{wi}.

If the coordinates of membrane corner B_{Mi} in the undeformed membrane are x_{Mi}, y_{Mi}, and z_{Mi}, the corner displacements of B_{Mi} can be expressed as:

$$\begin{aligned}
\Delta_{ui} &= u\left(x_f,\, y_f,\, z_f\right)\Big|_{x_f=x_{Mi},\, y_f=y_{Mi},\, z_f=z_{Mi}} \\
\Delta_{vi} &= v\left(x_f,\, y_f,\, z_f\right)\Big|_{x_f=x_{Mi},\, y_f=y_{Mi},\, z_f=z_{Mi}} \\
\Delta_{wi} &= w\left(x_f,\, y_f,\, z_f\right)\Big|_{x_f=x_{Mi},\, y_f=y_{Mi},\, z_f=z_{Mi}}
\end{aligned} \tag{3.4}$$

In the inertial frame *O-xyz*, the coordinates of B_{Mi} in the deformed membrane can be either expressed as functions of the generalized coordinates of the position and orientation of each bar, $\boldsymbol{q}$, or expressed as functions of the Euler's angles, γ_1, γ_2, and γ_3, and the corner displacements of the membrane, Δ_{ui}, Δ_{vi}, and Δ_{wi}. Clearly, the coordinates of membrane corners given by these functions must be identical. These equalities provide a set of displacement constraint equations formally written as:

$$\begin{aligned}
&\boldsymbol{OB_{Mi}}\left(\boldsymbol{q}\right) = \boldsymbol{OO_f}\left(\boldsymbol{q}\right) + \boldsymbol{R^{ef}}\left(\gamma_1,\gamma_2,\gamma_3\right)\cdot\boldsymbol{O_f B_{Mi}}(\Delta_{ui},\Delta_{vi},\Delta_{wi}) \\
&\left(i = 1,2,...,N-1\right)
\end{aligned} \tag{3.5}$$

By solving Eq. (3.5), the membrane corner displacements, Δ_{ui}, Δ_{vi}, and Δ_{wi}, and the Euler's angles, γ_1, γ_2, and γ_3, can be expressed as functions of $\boldsymbol{q}$.

The strain energy of tendons, U_{td}, is:

$$U_{td} = \sum_{i,j,d} \frac{1}{2} k_{ij}^{d} \left(\left|d_{ij}\right| - r_{ij}^{d}\right)^2 \tag{3.6}$$

where the symbol d denotes the type of tendons defined in Chapter 2, i.e. $d = S, V, D, C, P, R$. The symbol $|d_{ij}|$ represents the length of tendon d_{ij}.

The variation of U_{td} can be written as:

$$\delta U_{td} = \sum_{i,j,d} k_{ij}^{d} \left(\left|d_{ij}\right| - r_{ij}^{d}\right) \delta\left|d_{ij}\right| = \sum_{i,j,d} T_{ij}^{d} \delta\left|d_{ij}\right| \tag{3.7}$$

where k_{ij}^d and r_{ij}^d are the spring constant and the rest-length of tendon d_{ij}, respectively. Here, T_{ij}^d is the magnitude of the elastic force in tendon d_{ij}:

$$T_{ij}^d = k_{ij}^d \left(\left| d_{ij} \right| - r_{ij}^d \right) \tag{3.8}$$

The spring constant k_{ij}^d is defined as:

$$k_{ij}^d = \frac{E_{ij}^d A_{ij}^d}{r_{ij}^d} \tag{3.9}$$

where E_{ij}^d and A_{ij}^d are the Young's Modulus and the area of the cross section of tendon d_{ij}, respectively.

Let the strain energy of the tensioned membrane be labeled U_{mb}. According to Castigliano's first theorem [44], the variation of U_{mb} is:

$$\begin{aligned} \delta U_{mb} &= \frac{\partial U_{mb}}{\partial \Delta_{u1}} \delta \Delta_{u1} + \sum_{i=2}^{N-2} \left(\frac{\partial U_{mb}}{\partial \Delta_{ui}} \delta \Delta_{ui} + \frac{\partial U_{mb}}{\partial \Delta_{vi}} \delta \Delta_{vi} + \frac{\partial U_{mb}}{\partial \Delta_{wi}} \delta \Delta_{wi} \right) \\ &\quad + \left(\frac{\partial U_{mb}}{\partial \Delta_{u,N-1}} \delta \Delta_{u,N-1} + \frac{\partial U_{mb}}{\partial \Delta_{v,N-1}} \delta \Delta_{v,N-1} \right) \\ &= F_{u1} \delta \Delta_{u1} + \sum_{i=2}^{N-2} \left(F_{ui} \delta \Delta_{ui} + F_{vi} \delta \Delta_{vi} + F_{wi} \delta \Delta_{wi} \right) \\ &\quad + \left(F_{u,N-1} \delta \Delta_{u,N-1} + F_{v,N} \delta \Delta_{v,N-1} \right) \end{aligned} \tag{3.10}$$

where F_{ui}, F_{vi}, and F_{wi} are the forces exerted on the i-th corner of the membrane along $O_f x_f$, $O_f y_f$ and $O_f z_f$ axes. The variation of the membrane corner displacements can be formally written as:

$$\begin{cases} \delta \Delta_{jl} = \dfrac{\partial \Delta_{jl}}{\partial x_{Mi}} \delta x_{Mi} + \dfrac{\partial \Delta_{jl}}{\partial y_{Mi}} \delta y_{Mi} + \dfrac{\partial \Delta_{jl}}{\partial z_{Mi}} \delta z_{Mi} + \dfrac{\partial \Delta_{jl}}{\partial \theta_{Mi}} \delta \theta_{Mi} + \dfrac{\partial \Delta_{jl}}{\partial \psi_{Mi}} \delta \psi_{Mi}; & (M \geq 2) \\ \delta \Delta_{jl} = \dfrac{\partial \Delta_{jl}}{\partial \theta_{1i}} \delta \theta_{1i} + \dfrac{\partial \Delta_{jl}}{\partial \psi_{1i}} \delta \psi_{1i}; & (M = 1) \end{cases} \tag{3.11}$$
$$(j = u, v, w; \quad l = 1, 2, .., N-1; \quad i = 1, 2, .., N)$$

Since there is no external force exerted on the system, according to the principle of virtual work, the virtual work done by the internal forces, i.e. δW_{int}, should be zero when the system is at equilibrium:

$$\delta W_{int} = \delta U = 0 \tag{3.12}$$

where δU is the variation of the total strain energy of a tensegrity-membrane system.

Then, according to Eqs. (3.6) - (3.11), when $M \geq 2$, the variation of the total strain energy can be written as:

$$\begin{aligned} \delta U &= \delta(U_{mb} + U_{td}) \\ &= \sum_{i=1}^{N} \left(Q_{\theta}^{1i} \delta\theta_{1i} + Q_{\psi}^{1i} \delta\psi_{1i} \right) \\ &\quad + \sum_{k=2}^{M} \sum_{i=1}^{N} \left(Q_x^{ki} \delta x_{ki} + Q_y^{ki} \delta y_{ki} + Q_z^{ki} \delta z_{ki} + Q_{\theta}^{ki} \delta\theta_{ki} + Q_{\psi}^{ki} \delta\psi_{ki} \right) \end{aligned} \tag{3.13}$$

When $M = 1$, Eq. (3.13) can be simplified as:

$$\delta U = \sum_{i=1}^{N} \left(Q_{\theta}^{1i} \delta\theta_{1i} + Q_{\psi}^{1i} \delta\psi_{1i} \right) \tag{3.14}$$

When $M \geq 2$, since the variations of the independent generalized coordinates, δx_{ij}, δy_{ij}, δz_{ij}, $\delta\theta_{ij}$, and $\delta\psi_{ij}$, are arbitrary, the generalized forces, Q_x^{ij}, Q_y^{ij}, Q_z^{ij}, Q_{θ}^{ij}, and Q_{ψ}^{ij}, must be zero. Then, we have $(5M-3)N$ algebraic equations for static configurations:

$$\begin{aligned} & Q_{\theta}^{1,j} = 0; \quad Q_{\psi}^{1,j} = 0 \\ & Q_x^{ij} = 0; \quad Q_y^{ij} = 0; \quad Q_z^{ij} = 0; \quad Q_{\theta}^{ij} = 0; \quad Q_{\psi}^{ij} = 0 \\ & \left(i = 2,3,..,M; \quad j = 1,2,..,N \right) \end{aligned} \tag{3.15}$$

Arranging Eq. (3.15) in matrix form, we have

$$\begin{aligned} & \boldsymbol{A}(\boldsymbol{q})\boldsymbol{T}_{\boldsymbol{q}} = \boldsymbol{O} \\ & \boldsymbol{T}_{\boldsymbol{q}} = \left[F_{u1} \quad \boldsymbol{F}_2^{\,T} \quad \cdots \quad \boldsymbol{F}_{N-1}^{\,T} \quad T_{11}^{S} \quad \ldots \quad T_{1N}^{S} \quad \boldsymbol{T}_{21}^{\,T} \quad \ldots \quad \boldsymbol{T}_{MN}^{\,T} \right]^T \end{aligned} \tag{3.16}$$

where the vector $\boldsymbol{F}_i$ is:

$$\begin{aligned} \boldsymbol{F}_i &= \begin{bmatrix} F_{ui} & F_{vi} & F_{wi} \end{bmatrix}^T; \quad (2 \le i \le N-2) \\ \boldsymbol{F}_{N-1} &= \begin{bmatrix} F_{u,N-1} & F_{v,N-1} \end{bmatrix}^T \end{aligned} \tag{3.17}$$

When $i \geq 2$, the vector $\boldsymbol{T}_{ij}$ can be expressed as:

$$\boldsymbol{T}_{ij} = \begin{bmatrix} T_{ij}^S & T_{ij}^V & T_{ij}^D & T_{ij}^C & T_{ij}^P & T_{ij}^R \end{bmatrix}^T; \quad (i \ge 2) \tag{3.18}$$

Since the membrane and tendons must provide tensile forces at equilibrium, the null space of matrix $\boldsymbol{A}(\boldsymbol{q})$ should not be empty, and the tendons and the membrane must be tensioned.

When M =1, we only need to make $Q_\theta^{1,j}$ and $Q_\psi^{1,j}$ be zero. The procedure of converting the equations for static configurations into matrix form is the same as the one described above.

After solving Eq. (3.16) for equilibrium conditions, the value of $\boldsymbol{q}$ at the equilibrium can be found. Then, according to Eq. (3.5), the membrane corner displacements, Δ_{ui}, Δ_{vi}, and Δ_{wi}, at the equilibrium can be easily determined, since they can be expressed as functions of $\boldsymbol{q}$. The corresponding membrane corner forces, F_{ui}, F_{vi}, and F_{wi}, can be calculated based on the stress distribution in the membrane via, for example, the linear finite element method. Since the null space vector of matrix $\boldsymbol{A}(\boldsymbol{q})$ gives the relationship between tendon forces and membrane corner forces, after determining the membrane corner forces, the tendon forces can be also found. Then, tendon rest-lengths can be calculated by inserting the corresponding tendon forces into Eq. (3.8) and solving for r_{ij}^d.

3.3. Equilibrium Conditions for Symmetric Systems

In general, solving the nonlinear displacement constraints in Eq. (3.5) explicitly is not an easy task. Thus, equilibrium conditions of general tensegrity-membrane systems and

their static configurations have to be determined numerically. However, in many practical applications, symmetric structures are desired. Therefore, equilibrium conditions for symmetric tensegrity-membrane systems are of great importance. In the following, we show how symmetry conditions can greatly simplify the equilibrium conditions, eventually leading to analytical solutions.

3.3.1. Symmetric Tensegrity-Membrane Systems

For symmetric systems, the following additional assumptions are required:

a) The bases of all stages are parallel to each other.

b) The base of the i-th stage may only rotate with respect to the inertial reference frame along the Oz axis by the angle σ_i ($\sigma_1 = 0$); the z location of the i-th base is z_i ($z_1 = 0$).

c) The lengths of the bars in the i-th stage are identical, i.e. $l_{ij} = l_i$.

d) The declination angle θ_{ij} and azimuth angle ψ_{ij} of each bar in the i-th stage satisfy:

$$\theta_{ij} = \theta_i; \quad (i = 1,2,...M; \quad j = 1,2,...N) \tag{3.19}$$

and

$$\psi_{ij} = \begin{cases} \psi_i + 2j\pi/N; & (i = 1,2,...M; \quad j = 1,2,...N) \\ \psi_i; & (i = 1,2,...M; \quad j = N) \end{cases} \tag{3.20}$$

where θ_i and ψ_i are notations for the values of θ_{ij} and ψ_{ij} for bar b_{iN} at a symmetric equilibrium configuration.

e) The base of each stage is a regular convex polygon with N edges. The radius of the polygon's circumscribed circle for the base of the i-th stage is r_i.

f) The undeformed membrane is in the shape of a regular convex polygon with N edges; the radius of the polygon's circumscribed circle is r_{mb}.

The symmetry assumptions imply that, when the system is at equilibrium, the attached membrane is symmetrically tensioned. In other words, the total force exerted on the membrane corner B_{Mi} is pointing away from the geometrical center of the membrane, O_{GC}, towards B_{Mi}, and the magnitude of the total force exerted on each membrane corner is the same, labeled F_{Δ}. A sketch of a hexagonal membrane which is symmetrically tensioned is shown in Figure 3.2.

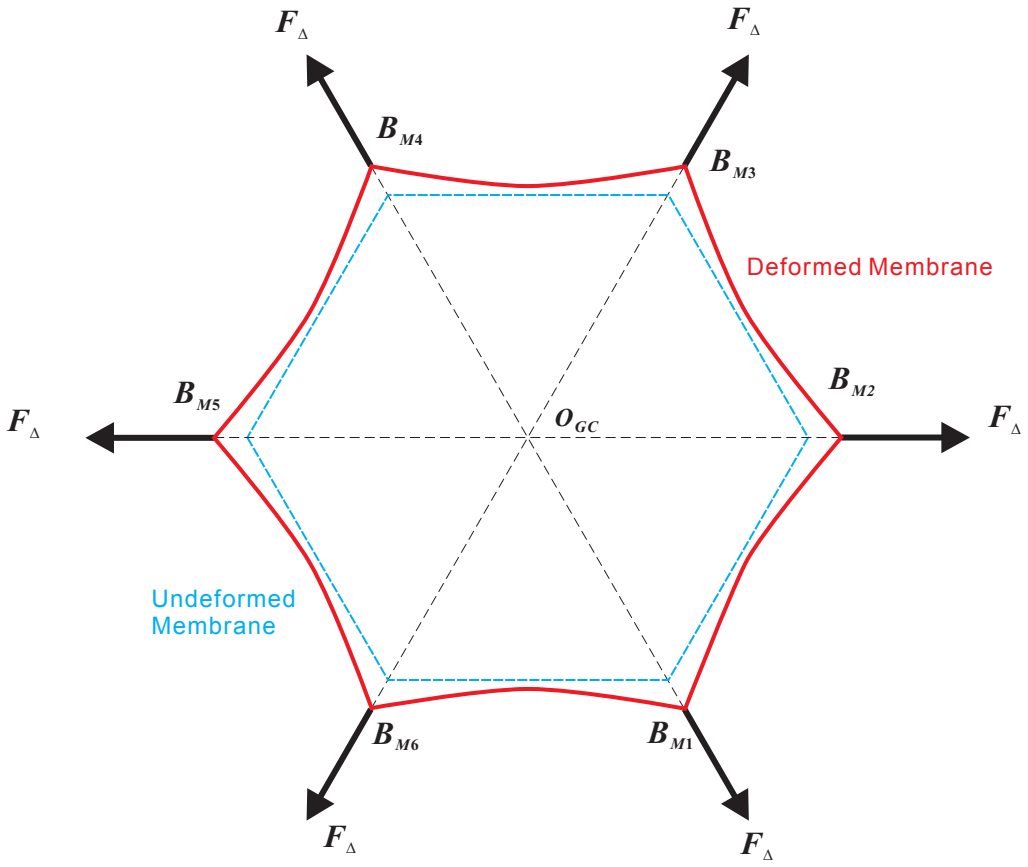

Figure 3.2. A symmetrically tensioned hexagonal membrane

Thus, the expressions of corner displacements and corner forces are

$$
\begin{cases}
\Delta_{ui} = \Delta\left(\cos\beta_i - \cos\beta_N\right) \\
\Delta_{vi} = \Delta\left(\sin\beta_i - \sin\beta_N\right) \\
\Delta_{wi} = 0
\end{cases}
$$

$$
\begin{cases}
F_{ui} = F_\Delta \cos\beta_i \\
F_{vi} = F_\Delta \sin\beta_i \\
F_{wi} = 0
\end{cases}
\tag{3.21}
$$

$$
\beta_i = -\frac{N+2}{2N}\pi + \frac{2i}{N}\pi; \quad \left(i = 1, 2, ..., N\right)
$$

The explicit expression of Δ obtained by applying symmetry conditions and solving Eq. (3.5) is:

$$
\Delta = -r_{mb} + \sqrt{{l_M}^2 \sin^2\theta_M + {r_M}^2 - 2r_M l_M \sin\theta_M \sin(\psi_M - \sigma_M + \frac{\pi}{N})}
\tag{3.22}
$$

where l_M is the length of each bar in the M-th stage.

For symmetric systems, the length of the tendons of the same type in the i-th stage is identical. This is also true for the corresponding tendon forces:

$$
\begin{aligned}
&\left|d_{ij}\right| = \left|d_i\right| \\
&T_{ij}^d = T_i^d = k_i^d\left(\left|d_i\right| - r_i^d\right) \\
&\left(i = 1, 2, ..., M; \quad d = S, V, D, P, C, R\right)
\end{aligned}
\tag{3.23}
$$

3.3.2. Equilibrium Conditions for *M-N* Symmetric Systems

After applying the symmetry assumptions to Eq. (3.15), it can be found that, for a given i, the algebraic equations satisfy the following conditions:

$$
\begin{aligned}
&Q_\theta^{1,j} = Q_\theta^1 = 0; \quad Q_\psi^{1,j} = Q_\psi^1 = 0 \\
&\begin{bmatrix} Q_x^{ij} \\ Q_y^{ij} \end{bmatrix} = \boldsymbol{C}_j \begin{bmatrix} Q_x^i \\ Q_y^i \end{bmatrix} = \boldsymbol{O}; \quad \begin{cases} Q_z^{ij} = Q_z^i = 0 \\ Q_\theta^{ij} = Q_\theta^i = 0 \\ Q_\psi^{ij} = Q_\psi^i = 0 \end{cases} \\
&\left(i = 2, 3, ...M; \quad j = 1, 2, \ldots N\right)
\end{aligned}
\tag{3.24}
$$

where

$$\boldsymbol{C}_j = \begin{bmatrix} \cos\alpha_j & \sin\alpha_j \\ \sin\alpha_j & -\cos\alpha_j \end{bmatrix}; \quad \alpha_j = \frac{2j-1}{N}\pi$$

It is obvious that the matrix $\boldsymbol{C_j}$ is always invertible, since the determinant of $\boldsymbol{C_j}$ is $\det \boldsymbol{C}_j = -(\cos^2\alpha_j + \sin^2\alpha_j) = -1$. Therefore, it can be concluded that, for symmetric systems, only 5 equations in the 5N statics equations of the i-th stage are linearly independent when $i \geq 2$, and only 2 equations in the 2N statics equations are linearly independent when $i = 1$.

When $M = 1$, the equilibrium conditions are:

$$\begin{aligned} Q_\theta^{1,j} &= Q_\theta^1 = 0 \\ Q_\psi^{1,j} &= Q_\psi^1 = 0 \end{aligned} \tag{3.25}$$

Clearly, only 2 equations in the 2N statics equations are linearly independent.

According to the results in Eq. (3.23), the vector of forces $\boldsymbol{T_q}$ can be simplified as:

$$\boldsymbol{T_{MN}} = \begin{bmatrix} T_1^S & \boldsymbol{T}_2^T & \cdots & \boldsymbol{T}_M^T & F_\Delta \end{bmatrix}^T \tag{3.26}$$

where

$$\boldsymbol{T}_i = \begin{bmatrix} T_i^S & T_i^V & T_i^D & T_i^C & T_i^P & T_i^R \end{bmatrix}^T; \quad (i \geq 2) \tag{3.27}$$

There are only 6M–4 elements in the vector $\boldsymbol{T_{MN}}$ for symmetric systems, while there are (6M–2)N–6 elements in $\boldsymbol{T_q}$ vector for general systems.

The numbers of rows and columns of the matrix $\boldsymbol{A}(\boldsymbol{q})$ are equal to the numbers of statics equations in Eq. (3.15) and the numbers of forces in $\boldsymbol{T_q}$, respectively. According to the conclusions related to Eq. (3.24) and Eq. (3.26), the number of rows and columns of the matrix $\boldsymbol{A}(\boldsymbol{q})$ can be significantly reduced. Then, $\boldsymbol{A}(\boldsymbol{q})$ can be expressed as a (5M−3)×(6M−4) matrix ($M \geq 1$). Clearly, for symmetric systems, the dimensions of $\boldsymbol{A}(\boldsymbol{q})$

are significantly reduced compared to the dimensions of $\boldsymbol{A}(\boldsymbol{q})$ for general systems, and so is the required computational cost of finding the vectors in the null space of $\boldsymbol{A}(\boldsymbol{q})$.

When $M \geq 2$, the number of the rows of $\boldsymbol{A}(\boldsymbol{q})$ is less than the number of the columns of the matrix. In this case, the null space of the $\boldsymbol{A}(\boldsymbol{q})$ matrix is always not void, and the only requirement is that each element of a vector in the null space must be positive. Due to the mathematical complexity of the matrix $\boldsymbol{A}(\boldsymbol{q})$, in general the equilibrium conditions can be solved numerically.

When $M = 1$, i.e. for one-stage symmetric tensegrity-membrane systems, the equilibrium requirements are different from the equilibrium conditions of M-N symmetric systems discussed in this section. More details can be found in the following sections and explicit solutions can be derived.

3.3.3. Equilibrium Conditions for 1-*N* Symmetric Systems

For symmetric one-stage tensegrity-membrane systems, i.e. 1-N symmetric systems, only the tendons S_{1j} are involved in the system. Therefore, after applying the symmetry assumptions, the force vector is:

$$\boldsymbol{T}_{1N} = \begin{bmatrix} T_1^S & F_\Delta \end{bmatrix}^T \tag{3.28}$$

All tendons of the 1-N symmetric system have the same length, which can be expressed as:

$$\left|S_{1j}\right| = \left|S_1\right| = \sqrt{l_1^2 + 4r_1^2 \sin^2\frac{\pi}{N} - 4r_1 l_1 \sin\frac{\pi}{N}\sin\theta_1 \cos\psi_1} \tag{3.29}$$

where l_1 is the length of each bar in the system, i.e. $l_{1j} = l_1$ ($j = 1, 2, \ldots, N$).

To simplify the expression of the matrix $\boldsymbol{A}(\boldsymbol{q})$, we introduce the averaged tendon and membrane forces, which are defined as:

$$\overline{T_1^S} = \frac{T_1^S}{|S_1|}; \quad \overline{F_\Delta} = \frac{F_\Delta}{\Delta + r_{mb}}$$
$$\overline{\boldsymbol{T}_{1N}} = \left[\overline{T_1^S} \quad \overline{F_\Delta}\right]^T \tag{3.30}$$

Clearly, the physical meaning of the averaged tendon force is the force density in the tendon, while the averaged membrane force has no significant physical meaning.

Inserting the symmetry assumptions into Eq. (3.16), we obtain:

$$\boldsymbol{A}_{1N}\overline{\boldsymbol{T}_{1N}} = \begin{bmatrix} -2r_1 l_1 \sin\frac{\pi}{N}\cos\theta_1\cos\psi_1 & l_1\cos\theta_1\left(l_1\sin\theta_1 - r_1\sin(\psi_1+\frac{\pi}{N})\right) \\ 2r_1 l_1 \sin\frac{\pi}{N}\sin\theta_1\sin\psi_1 & -r_1 l_1\sin\theta_1\cos(\psi_1+\frac{\pi}{N}) \end{bmatrix}\begin{bmatrix}\overline{T_1^S} \\ \overline{F_\Delta}\end{bmatrix} = \boldsymbol{O} \tag{3.31}$$

The null space of $\boldsymbol{A}_{1N}$ is not void if and only if $\det \boldsymbol{A}_{1N} = 0$, which leads to:

$$\det \boldsymbol{A}_{1N} = r_1 l_1^2 \sin 2\theta_1 \sin\frac{\pi}{N}\left(r_1\cos\frac{\pi}{N} - l_1\sin\theta_1\sin\psi_1\right) = 0 \tag{3.32}$$

Considering $\theta_1 \in (0, \pi/2)$, the nontrivial solution to Eq. (3.32) is:

$$r_1 = \frac{l_1\sin\theta_1\sin\psi_1}{\cos(\pi/N)} \tag{3.33}$$

The averaged force vector can be found by determining the null space of $\boldsymbol{A}_{1N}$

$$\overline{\boldsymbol{T}_{1N}} = \begin{bmatrix}\overline{T_1^S} \\ \overline{F_\Delta}\end{bmatrix} = \overline{F_\Delta}\begin{bmatrix}\dfrac{\cos(\psi_1+\pi/N)}{2\sin\psi_1\sin(\pi/N)} \\ 1\end{bmatrix} \tag{3.34}$$

Note that based on the previous discussion and Eq. (3.21), the membrane is tensioned when $F_\Delta > 0$. Since the system is always in tension, each element of the averaged force vector must be greater than 0. Taking into consideration $\psi_1 \in (-\pi, \pi)$, this requirement is equivalent to the following conditions:

$$\overline{F_\Delta} > 0; \quad \cot\psi_1 > \tan\frac{\pi}{N} \tag{3.35}$$

After applying the assumptions for symmetric systems and considering that membranes must be tensioned, Eq. (3.22) and the related requirement for the membrane corner displacement can be expressed as:

$$\Delta = -r_{mb} + l_1 \sin\theta_1 \frac{\cos\left(\pi/N + \psi_1\right)}{\cos(\pi/N)} > 0 \tag{3.36}$$

Thus, the equilibrium conditions for 1-*N* symmetric systems are:

$$\begin{cases} r_1 = \dfrac{l_1 \sin\theta_1 \sin\psi_1}{\cos(\pi/N)} \\ r_{mb} < l_1 \sin\theta_1 \dfrac{\cos\left(\pi/N + \psi_1\right)}{\cos(\pi/N)} \\ \overline{F_\Delta} > 0 \\ \cot\psi_1 > \tan\dfrac{\pi}{N} \end{cases} \tag{3.37}$$

3.3.4. Equilibrium Conditions of 1-*N*(D) Symmetric Systems

For 1-*N*(D) symmetric tensegrity-membrane systems, after applying the symmetry assumptions, the tendon lengths of tendon *SU* and tendon *SL* are:

$$\begin{aligned} \left|SL_j\right| &= \left|SL\right| = \sqrt{4r_1^2 \sin^2\frac{\pi}{N} + {k_H}^2 l_1^2 - 4k_H r_1 l_1 \sin\theta_1 \cos\psi_1 \sin\frac{\pi}{N}} \\ \left|SU_j\right| &= \left|SU\right| = \\ &\sqrt{\begin{aligned} &4r_1 \sin\frac{\pi}{N}\left(r_1 \sin\frac{\pi}{N} + l_1 \sin\theta_1 \left(\cos\left(\psi_1 + \frac{2\pi}{N}\right) - k_H \cos\psi_1\right)\right) \\ &+ l_1^2 \left(1 + {k_H}^2 - 2k_H \left(\cos^2\frac{\pi}{N} + \sin^2\frac{\pi}{N}\cos 2\theta_1\right)\right) \end{aligned}} \end{aligned} \tag{3.38}$$

The averaged tendon and membrane forces are defined as:

$$\overline{T_{SL}}=\frac{T_{SL}}{|SL|};\quad \overline{T_{SU}}=\frac{T_{SU}}{|SU|};\quad \overline{F_{\Delta}}=\frac{F_{\Delta}}{\Delta+r_{mb}}$$
$$\overline{\boldsymbol{T}_{1N}^{D}}=\begin{bmatrix}\overline{T_{SL}} & \overline{T_{SU}} & \overline{F_{\Delta}}\end{bmatrix}^{T} \tag{3.39}$$

After applying these assumptions, Eq. (3.16) can be simplified as:

$$\boldsymbol{A}_{1N}^{D}\overline{\boldsymbol{T}_{1N}^{D}}=\begin{bmatrix}A_{11} & A_{12} & A_{13}\\ A_{21} & A_{22} & A_{23}\end{bmatrix}\begin{bmatrix}\overline{T_{SL}}\\ \overline{T_{SU}}\\ \overline{F_{\Delta}}\end{bmatrix}=\boldsymbol{O}$$
$$A_{11}=-2k_H r_1 l_1\cos\theta_1\cos\psi_1$$
$$A_{12}=2l_1\cos\theta_1\left(r_1\left(\cos\left(\psi_1+2\pi/N\right)-k_H\cos\psi_1\right)+2k_H l_1\sin\theta_1\sin\left(\pi/N\right)\right)$$
$$A_{13}=l_1\cos\theta_1\left(l_1\sin\theta_1-r_1\sin\left(\psi_1+\pi/N\right)\right)/\sin\left(\pi/N\right) \tag{3.40}$$
$$A_{21}=2k_H r_1 l_1\sin\theta_1\sin\psi_1$$
$$A_{22}=-2r_1 l_1\sin\theta_1\left(\sin\left(\psi_1+2\pi/N\right)-k_H\sin\psi_1\right)$$
$$A_{23}=-r_1 l_1\sin\theta_1\cos\left(\psi_1+\pi/N\right)/\sin\left(\pi/N\right)$$

The null space of $\boldsymbol{A}(\boldsymbol{q})$ has nonzero components always. The elements of $\overline{\boldsymbol{T}_{1N}^{D}}$ are required to be positive, to enable tensioned tendons and tensioned membrane. After imposing this condition, we obtain analytical equilibrium conditions for 1-N(D) systems:

$$\begin{cases}k_H\dfrac{l_1\sin\theta_1\sin\psi_1}{\cos\left(\pi/N\right)}<r_1<\dfrac{l_1\sin\theta_1\sin\psi_1}{\cos\left(\pi/N\right)}\\ \overline{F_{\Delta}}>0\\ r_{mb}<l_1\sin\theta_1\dfrac{\cos\left(\pi/N+\psi_1\right)}{\cos(\pi/N)}\end{cases} \tag{3.41}$$

3.4. Conclusions

In this chapter, a systematic method is developed to find equilibriums of tensegrity-membrane systems. Due to mathematical complexity, the equilibrium conditions for general *M*-*N* tensegrity-membrane systems have to be solved numerically. For symmetric

tensegrity-membrane systems, the equilibrium conditions can be greatly simplified. Furthermore, analytical equilibrium conditions can be found for one-stage symmetric tensegrity-membrane systems.

Chapter 4: Nonlinear Finite Element Models

4.1. Introduction

Tensegrity-membrane systems are assemblies of bars, tendons, and membranes. The attached membranes should be treated as deformable bodies and the bars can be either treated as rigid bodies or as flexible bodies. Therefore, tensegrity-membrane systems fall into the class of flexible multibody systems. Broadly speaking, flexible multibody systems can be divided into two categories: linear flexible multibody systems and nonlinear flexible multibody systems [45]. Linear flexible multibody systems are usually studied by introducing floating reference frames and applying linear elastic models to the flexible components. For nonlinear flexible multibody systems, since the flexible components will experience large deformations, the nonlinear finite element method is commonly used for analysis. Tensegrity-membrane systems may experience large amplitude vibrations and significant shape changes, so they should be categorized as nonlinear flexible multibody systems and the nonlinear finite element method should be employed in the analysis of system dynamics.

The nonlinear finite element method is an extension of the linear finite element method. After the linear finite element method became known through the work of the Boeing group and the paper of Tuner, et al. [46], researchers and engineers began extending the method to nonlinear problems. Oden's work [47] is particularly noteworthy since it pioneered the field of nonlinear finite element analysis of solids and structures. Other excellent books (e.g. [48, 49]) provide useful introductions to nonlinear finite element analysis. For nonlinear continuum mechanics and nonlinear finite element

analysis, several stress and strain measures and different formulations are introduced. Generally speaking, the total Lagrangian formulation and the updated Lagrangian formulation are the two major formulations for nonlinear solid analysis. For the total Lagrangian formulation, the second Piola-Kirchhoff stress and Green-Lagrange strain are used, while for the updated Lagrangian formulation, Cauchy stress and Almansi strain are used. For small strain problems, these two formulations give similar results, and the choice of different formulations depends on the different nature of the problems in practice.

In this chapter, two nonlinear finite element models are developed to study the dynamics of tensegrity-membrane systems, namely the shell-beam-cable model and the membrane-truss-cable model. The dynamics of tendons is taken into account in these two models, leading to the possibility of examining the effects of tendons on the whole system. The shell-beam-cable model is a model of great generality, since the transverse bending stiffness and transverse shear stiffness of the membrane are considered and the bars are modeled as beams. For the membrane-truss-cable model, the transverse bending and shear effects of the membrane are ignored since the membrane is very thin. Each bar is assumed to only experience deformation along its longitudinal axis. For these two models, the total Lagrangian formulation is used to perform the nonlinear finite element analysis. Details of the structural elements used for the two nonlinear finite element models are presented. Then, numerical examples are used to test the structural elements discussed in this work.

Note that all of the coordinates and displacements used in this chapter are measured with respect to the inertial reference frame *O*-*xyz*. The notations used in this chapter are locally defined and tensor notations are used for simplicity.

4.2. Total Lagrangian Formulation

In this section, the strain and stress components are expressed in the curvilinear coordinate system O-$r_1r_2r_3$, and a tilde (~) is placed over the terms express in the O-$r_1r_2r_3$ frame.

The principle of virtual work applied to the configuration at time $t+\Delta t$ is:

$$\int_{{}^0V} {}^{t+\Delta t}_{\ 0}\tilde{S}^{ij}\,\delta\,{}^{t+\Delta t}_{\ 0}\tilde{\varepsilon}_{ij}\ {}^0dV = {}^{t+\Delta t}\mathcal{R} \tag{4.1}$$

where ${}^{t+\Delta t}_{\ 0}\tilde{S}^{ij}$ is the contravariant component of the second Piola-Kirchhoff stress tensor at time $t+\Delta t$ with respect to the configuration at time 0, and ${}^{t+\Delta t}_{\ 0}\tilde{\varepsilon}_{ij}$ is the covariant component of the Green-Lagrange strain at time $t+\Delta t$ with respect to time 0. The term ${}^{t+\Delta t}\mathcal{R}$ is the virtual work due to external forces and torques.

The stress and strain components can be decomposed as:

$$\begin{aligned} {}^{t+\Delta t}_{\ 0}\tilde{S}^{ij} &= {}^{t}_{\ 0}\tilde{S}^{ij} + {}_0\tilde{S}^{ij} \\ {}^{t+\Delta t}_{\ 0}\tilde{\varepsilon}_{ij} &= {}^{t}_{\ 0}\tilde{\varepsilon}_{ij} + {}_0\tilde{\varepsilon}_{ij} \end{aligned} \tag{4.2}$$

In addition, the strain increment ${}_0\tilde{\varepsilon}_{ij}$ can be written as the combination of linear part ${}_0\tilde{e}_{ij}$ and a nonlinear part ${}_0\tilde{\eta}_{ij}$:

$${}_0\tilde{\varepsilon}_{ij} = {}_0\tilde{e}_{ij} + {}_0\tilde{\eta}_{ij} \tag{4.3}$$

After linearization, Eq. (4.1) is:

$$\int_{{}^0V} {}_0\tilde{C}^{ijrl}\,{}_0\tilde{e}_{rl}\delta\,{}_0\tilde{e}_{ij}\,{}^0dV + \int_{{}^0V} {}_0^t\tilde{S}^{ij}\delta\,{}_0\tilde{\eta}_{ij}\,{}^0dV = {}^{t+\Delta t}\mathcal{R} - \int_{{}^0V} {}_0^t\tilde{S}^{ij}\delta\,{}_0\tilde{\varepsilon}_{ij}\,{}^0dV \tag{4.4}$$

In Eq. (4.4), the incremental solution at $t+\Delta t$ can be computed. To improve the accuracy, an iteration procedure is applied, and the equation is:

$$\begin{aligned}
&\int_{{}^0V} {}_0\tilde{C}^{ijrl(k-1)}\,{}_0\tilde{e}_{rl}^{\,(k)}\delta\,{}_0\tilde{e}_{ij}\,{}^0dV + \int_{{}^0V} {}_0^t\tilde{S}^{ij(k-1)}\delta\,{}_0\tilde{\eta}_{ij}^{\,(k)}\,{}^0dV = {}^{t+\Delta t}\mathcal{R} - \int_{{}^0V} {}_0^t\tilde{S}^{ij(k-1)}\delta\,{}_0\tilde{\varepsilon}_{ij}^{\,(k-1)}\,{}^0dV \\
&{}^{t+\Delta t}u_i^{(k)} = {}^{t+\Delta t}u_i^{(k-1)} - \Delta u_i^{(k)}; \quad {}^{t+\Delta t}u_i^{(0)} = {}^t u_i
\end{aligned} \tag{4.5}$$

Note that the virtual work ${}^{t+\Delta t}\mathcal{R}$ includes the virtual work of inertia forces and damping forces. Arranging Eq. (4.5) in matrix form gives the matrix equation for finite element analysis:

$$\begin{aligned}
&\boldsymbol{M}\,{}^{t+\Delta t}\ddot{\boldsymbol{U}}^{(k)} + \left({}_0^t\boldsymbol{K}_{\boldsymbol{L}}^{(k-1)} + {}_0^t\boldsymbol{K}_{\boldsymbol{NL}}^{(k-1)}\right)\Delta\boldsymbol{U}^{(k)} = {}^{t+\Delta t}\boldsymbol{R} - {}_0^{t+\Delta t}\boldsymbol{F}^{(k-1)} \\
&{}^{t+\Delta t}\boldsymbol{U}^{(k)} = {}^{t+\Delta t}\boldsymbol{U}^{(k-1)} + \Delta\boldsymbol{U}^{(k)}; \quad {}^{t+\Delta t}\boldsymbol{U}^{(0)} = {}^t\boldsymbol{U}
\end{aligned} \tag{4.6}$$

where $\boldsymbol{M}$ is the mass matrix. $\boldsymbol{K_L}$ and $\boldsymbol{K_{NL}}$ represent the linear strain incremental stiffness matrix and the nonlinear strain incremental stiffness matrix, respectively. Here, ${}^{t+\Delta t}\boldsymbol{R}$ is the vector of externally applied nodal point loads at time $t+\Delta t$, $\boldsymbol{F}$ represents the vector of nodal point forces equivalent to element stresses, and $\boldsymbol{U}$ represents the vector of nodal displacements.

In the curvilinear coordinate system, the Green-Lagrange strain components can be written as:

$${}_0^t\tilde{\varepsilon}_{ij} = \frac{1}{2}\left({}^t\vec{g}_i \cdot {}^t\vec{g}_j - {}^0\vec{g}_i \cdot {}^0\vec{g}_j\right) \tag{4.7}$$

Note that the symbol $\vec{v}$ represents the Gibbs' vector, while $\boldsymbol{v}$ is the corresponding column vector. In other words, if $\boldsymbol{v}$ is expressed as $\boldsymbol{v} = \begin{bmatrix} v_1 & v_2 & v_3 \end{bmatrix}^T$, then $\vec{v}$ can be written as

$\vec{v} = v_1\vec{e}_x + v_2\vec{e}_y + v_3\vec{e}_z$, where $\vec{e}_x$, $\vec{e}_y$, and $\vec{e}_z$ are the basis vectors of the inertial reference frame *O-xyz*.

The covariant basis vectors of the curvilinear coordinate system ${}^k\vec{g}_i$ are defined as:

$${}^k\vec{g}_i = \frac{\partial {}^k\vec{x}}{\partial r_i}; \quad \left(k = 0,\ ...,\ t,\ t+\Delta t,\ ...\right) \tag{4.8}$$

To apply Eq. (4.5), we need the appropriate constitutive law in the curvilinear coordinate system:

$$\tilde{S}_{ij} = \tilde{C}^{ijrl}\tilde{\varepsilon}_{rl} \tag{4.9}$$

where $\tilde{C}^{ijrl}$ is the contravariant constitutive tensor in the curvilinear coordinates r_i, which is not known directly. Since the constitutive tensor C^{mnop} in the local Cartesian coordinates of orthonormal basis vectors $\vec{e}_i$ is known, the constitutive tensor in Eq.(4.9) can be obtained using the transformation:

$$\tilde{C}^{ijrl} = \left({}^0\vec{g}^{\,i}\cdot\vec{e}_m\right)\left({}^0\vec{g}^{\,j}\cdot\vec{e}_n\right)\left({}^0\vec{g}^{\,r}\cdot\vec{e}_o\right)\left({}^0\vec{g}^{\,l}\cdot\vec{e}_p\right)C^{mnop} \tag{4.10}$$

where the basis vectors of the local Cartesian coordinates $\vec{e}_i$ are defined as:

$$\vec{e}_3 = \frac{{}^0\vec{g}_3}{\left\|{}^0\vec{g}_3\right\|}; \quad \vec{e}_1 = \frac{{}^0\vec{g}_2\times\vec{e}_3}{\left\|{}^0\vec{g}_2\times\vec{e}_3\right\|}; \quad \vec{e}_2 = \vec{e}_3\times\vec{e}_1 \tag{4.11}$$

4.3. Shell-Beam-Cable Model

The goal of developing the shell-beam-cable model is to describe the dynamics of tensegrity-membrane systems without introducing specific modeling assumptions for system components. To achieve this goal, shell elements are used for the attached membrane, the bars are treated as beams, and the tendons are modeled by truss elements. The MITC4 shell element and the four-node beam element introduced in [48] are used in

this work. Transverse bending stiffness and transverse shear stiffness are considered in these two elements.

4.3.1. MICT4 Shell Element

In the MITC4 shell element, the coordinates of a generic point can be written as:

$$ {}^{t}x_i = \sum_{k=1}^{4} h_k \, {}^{t}x_i^k + \frac{r_3}{2} \sum_{k=1}^{4} a_k h_k \, {}^{t}V_{ni}^k \tag{4.12} $$

where the superscript t indicates that the coordinates are measured at time t, the subscript i (i = 1, 2, 3) corresponds to x, y, and z directions in the O-xyz frame, and k corresponds to the k-th node of an element. The symbol a represents the shell thickness, and $\boldsymbol{V_n}$ represents the normal vector. The symbol h_k is the interpolation function for a four-node shell element:

$$ \begin{aligned} h_1 &= \frac{1}{4}(1+r_1)(1+r_2); \quad h_2 = \frac{1}{4}(1-r_1)(1+r_2) \\ h_3 &= \frac{1}{4}(1-r_1)(1-r_2); \quad h_4 = \frac{1}{4}(1+r_1)(1-r_2) \end{aligned} \tag{4.13} $$

Using Eq. (4.12) at times 0, t, and t+Δt, we can express the displacements as:

$$ {}^{t}u_i = {}^{t}x_i - {}^{0}x_i; \quad u_i = {}^{t+\Delta t}x_i - {}^{t}x_i \tag{4.14} $$

After inserting Eq. (4.12) into Eq.(4.14), we obtain:

$$ \begin{aligned} {}^{t}u_i &= \sum_{k=1}^{4} h_k \, {}^{t}u_i^k + \frac{r_3}{2} \sum_{k=1}^{4} a_k h_k \left({}^{t}V_{ni}^k - {}^{0}V_{ni}^k \right) \\ u_i &= \sum_{k=1}^{4} h_k u_i^k + \frac{r_3}{2} \sum_{k=1}^{4} a_k h_k V_{ni}^k \end{aligned} \tag{4.15} $$

where $V_{ni}^k = {}^{t+\Delta t}V_{ni}^k - {}^{t}V_{ni}^k$. The vector $\boldsymbol{V_n^k}$ represents the increments of $\boldsymbol{{}^{t}V_n^k}$. The symbols α_k and β_k are defined as the nodal rotational degrees of freedom for node k. For small

rotations, $\boldsymbol{V_n^k}$ can be approximated as: $\boldsymbol{V_n^k} = -{}^t\boldsymbol{V_2^k}\alpha_k + {}^t\boldsymbol{V_1^k}\beta_k$. The vectors ${}^t\boldsymbol{V_1^k}$ and ${}^t\boldsymbol{V_2^k}$ are defined as:

$$ {}^t\vec{V}_1^k = \frac{\vec{e}_y \times {}^t\vec{V}_n^k}{\left\| \vec{e}_y \times {}^t\vec{V}_n^k \right\|}; \quad {}^t\vec{V}_2^k = {}^t\vec{V}_n^k \times {}^t\vec{V}_1^k \tag{4.16} $$

If ${}^t\boldsymbol{V_n^k}$ is parallel to $\boldsymbol{e_y}$, we set ${}^t\boldsymbol{V_1^k}$ equal to $\boldsymbol{e_z}$.

For the MITC4 shell element, the mixed interpolation technique is employed to eliminate shear locking, and it has been shown that this element does not experience membrane locking. To apply mixed interpolation, the transverse shear strain components are chosen as:

$$ \tilde{\varepsilon}_{13} = \frac{1}{2}(1+r_2)\tilde{\varepsilon}_{13}^A + \frac{1}{2}(1-r_2)\tilde{\varepsilon}_{13}^C; \quad \tilde{\varepsilon}_{23} = \frac{1}{2}(1+r_1)\tilde{\varepsilon}_{23}^D + \frac{1}{2}(1-r_1)\tilde{\varepsilon}_{23}^B \tag{4.17} $$

where

$$ \begin{aligned} \tilde{\varepsilon}_{13}^A &= \tilde{\varepsilon}_{13}\big|_{r_1=0;\ r_2=1;\ r_3=0}; \quad \tilde{\varepsilon}_{23}^C = \tilde{\varepsilon}_{23}\big|_{r_1=0;\ r_2=-1;\ r_3=0} \\ \tilde{\varepsilon}_{13}^D &= \tilde{\varepsilon}_{13}\big|_{r_1=1;\ r_2=0;\ r_3=0}; \quad \tilde{\varepsilon}_{23}^B = \tilde{\varepsilon}_{13}\big|_{r_1=-1;\ r_2=0;\ r_3=0} \end{aligned} \tag{4.18} $$

4.3.2. Beam Element

For the four-node beam element, the coordinates of a generic point can be written as:

$$ {}^t x_i = \sum_{k=1}^{4} h_k\, {}^t x_i^k + \frac{r_2}{2}\sum_{k=1}^{4} a_k h_k\, {}^t V_{1i}^k + \frac{r_3}{2}\sum_{k=1}^{4} b_k h_k\, {}^t V_{2i}^k \tag{4.19} $$

where a and b represent the beam thickness, $\boldsymbol{V_1}$ and $\boldsymbol{V_2}$ represent the normal vectors, and h_k is the interpolation function for a four-node beam element:

$$ \begin{aligned} h_1 &= -\frac{1}{16}(1-r_1)(1-3r_1)(1+3r_1); \quad h_2 = \frac{9}{16}(1-r_1)(1+r_1)(1-3r_1) \\ h_3 &= \frac{9}{16}(1-r_1)(1+r_1)(1+3r_1); \qquad h_4 = -\frac{1}{16}(1+r_1)(1-3r_1)(1+3r_1) \end{aligned} \tag{4.20} $$

After inserting Eq. (4.19) into Eq.(4.14), the displacements can be expressed as:

$$
\begin{aligned}
{}^{t}u_i &= \sum_{k=1}^{4} h_k \, {}^{t}u_i^k + \frac{r_2}{2}\sum_{k=1}^{4} a_k h_k \left({}^{t}V_{1i}^k - {}^{0}V_{1i}^k \right) + \frac{r_3}{2}\sum_{k=1}^{4} b_k h_k \left({}^{t}V_{2i}^k - {}^{0}V_{2i}^k \right) \\
u_i &= \sum_{k=1}^{4} h_k u_i^k + \frac{r_2}{2}\sum_{k=1}^{4} a_k h_k V_{1i}^k + \frac{r_3}{2}\sum_{k=1}^{4} b_k h_k V_{2i}^k
\end{aligned}
\tag{4.21}
$$

where $V_{1i}^k = {}^{t+\Delta t}V_{1i}^k - {}^{t}V_{1i}^k$ and $V_2^k = {}^{t+\Delta t}V_2^k - {}^{t}V_{2i}^k$. The three rotational degrees of freedom in the *x*, *y*, and *z* axes for node *k* are defined as θ_{k1}, θ_{k2}, and θ_{k3}. For small angles, the vectors $\boldsymbol{V_1^k}$ and $\boldsymbol{V_2^k}$ can be expressed as:

$$
\vec{V}_1^k = \vec{\theta}_k \times {}^{t}\vec{V}_1^k; \quad \vec{V}_2^k = \vec{\theta}_k \times {}^{t}\vec{V}_2^k \tag{4.22}
$$

where $\boldsymbol{\theta_k} = \begin{bmatrix} \theta_{k1} & \theta_{k2} & \theta_{k3} \end{bmatrix}^T$.

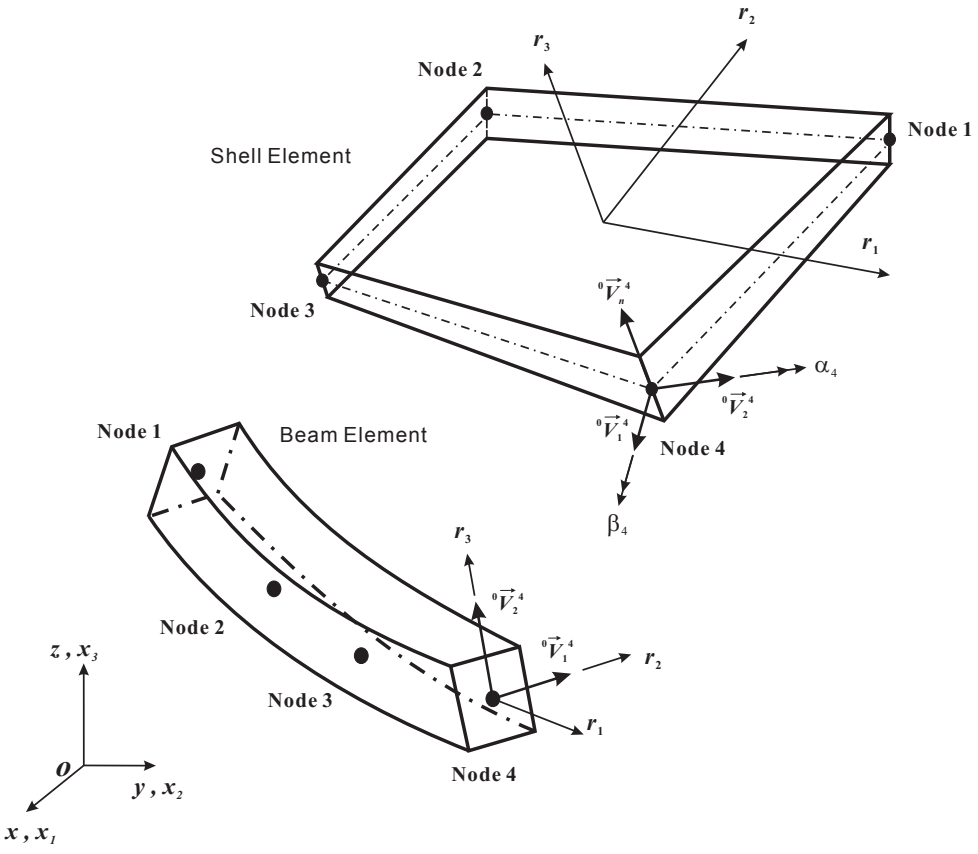

Figure 4.1. MITC4 shell element and four-node beam element

The reduced integration technique is used to eliminate membrane locking and shear locking. It should be noted that this four-node beam element still performs well when the full numerical integration is used [48].

4.3.3. Truss Element

The coordinates of an arbitrary point in the two-node truss element are:

$$ {}^{t}x_i = \sum_{k=1}^{2} h_k \, {}^{t}x_i^k \tag{4.23} $$

The symbol h_k is the interpolation function for a two-node element:

$$ \begin{aligned} h_k &= \frac{1}{2}\left(1 + r_1^k r_1\right); \quad (k = 1, 2) \\ r_1^1 &= -1; \quad r_1^2 = 1 \end{aligned} \tag{4.24} $$

The displacement expressions are the same as the expressions in Eq. (4.28).

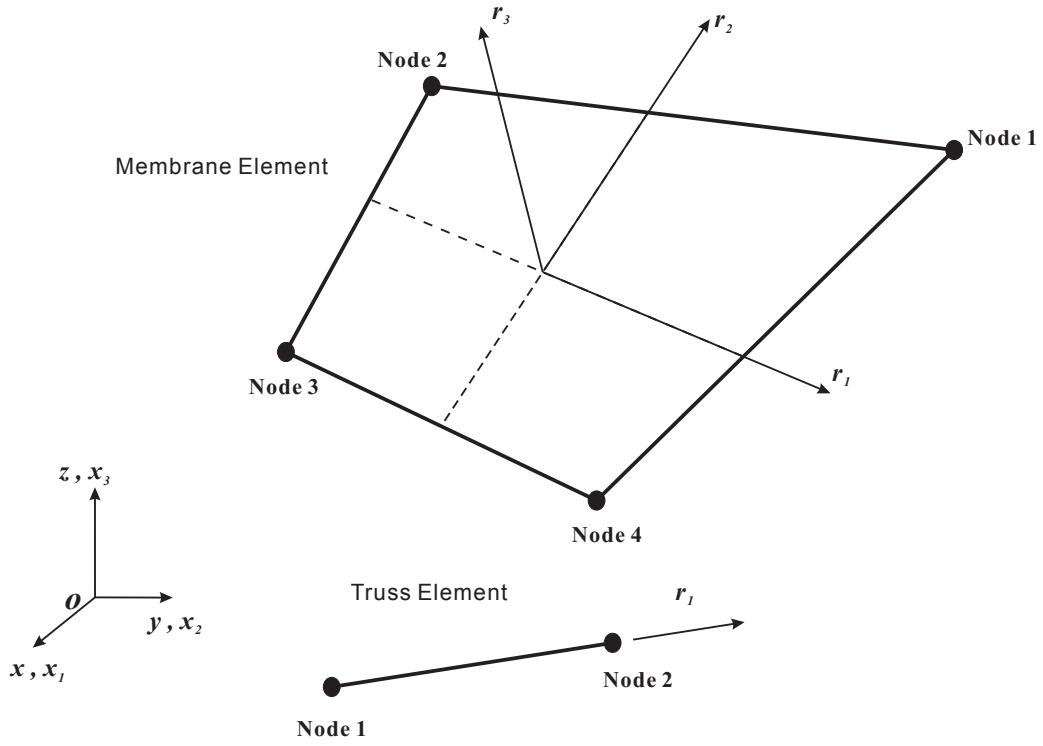

Figure 4.2. Four-node membrane element and two-node truss element

4.4. Membrane-Truss-Cable Model

The shell-beam-cable finite element model discussed in the previous section is a very general model for tensegrity-membrane systems. As a result, the cost of developing and solving such a model of great generality is high. Based on the physical properties of system components, some modeling assumptions can be made to simplify the model.

First note that membranes used in practice are very thin (the thickness of the membranes used in this work is 51 μm, and the ratio of thickness to length/width is around 10^{-5}). As a consequence, the transverse bending stiffness and transverse shear stiffness have little effect on the membrane dynamics and may be ignored. Thus, the attached membrane can be modeled by membrane elements. For the bars of tensegrity-membrane systems, the bar ends are either connected to the system base through frictionless rotational joints or connected to the ends of tendons or the membrane corners. These boundary conditions indicate that the bars in tensegrity-membrane systems are not rigidly constrained. Thus, bending deformation and shear deformation of bars are less likely to occur. Therefore, it may be possible to model the bars without considering the bending and shear stiffness and obtain a sufficiently accurate tensegrity-membrane model at a cost much lower than that for the shell-beam-cable model.

Based on these considerations, the following two additional modeling assumptions are made for the membrane-truss-cable model:

a) The transverse bending stiffness and transverse shear stiffness of the attached membrane are ignored.
b) The bars are assumed to experience axial deformation only.

The two-node truss element, discussed in the previous section, is used to model the bars and the tendons. The membrane element used to model the attached membrane will be discussed in the next section.

4.4.1. Membrane Element

The membrane element can be treated as a simplified nonlinear shell element without transverse bending and shear stiffness. A four-node membrane element is used in this work.

The coordinates of an arbitrary point in the four-node membrane element are:

$$ {}^{t}x_i = \sum_{k=1}^{4} h_k \, {}^{t}x_i^k \tag{4.25} $$

where the superscript t indicates that the coordinates are measured at time t, the subscript i (i = 1, 2, 3) corresponds to x, y, and z directions in the O-xyz frame, and k (i = 1, 2, 3, 4) corresponds to the k-th node of an element. The symbol h_k is the interpolation function for a four-node element:

$$ \begin{cases} h_1 = \dfrac{1}{4}(1+r_1)(1+r_2) \\ h_2 = \dfrac{1}{4}(1-r_1)(1+r_2) \\ h_3 = \dfrac{1}{4}(1-r_1)(1-r_2) \\ h_4 = \dfrac{1}{4}(1+r_1)(1-r_2) \end{cases} \tag{4.26} $$

Using Eq. (4.25) at times 0, t, and t+Δt, we can express the displacements as:

$$ \begin{aligned} {}^{t}u_i &= {}^{t}x_i - {}^{0}x_i \\ u_i &= {}^{t+\Delta t}x_i - {}^{0}x_i \end{aligned} \tag{4.27} $$

After inserting Eq.(4.25) into Eq.(4.27), we obtain:

$$
\begin{aligned}
{}^{t}u_i &= \sum_{k=1}^{4} h_k \, {}^{t}u_i^k \\
u_i &= \sum_{k=1}^{4} h_k u_i^k
\end{aligned}
\tag{4.28}
$$

4.5. Validation of Structural Elements

In this section, several benchmark problems are used to test the MITC4 shell element, the four-node beam element, and the two-node truss element discussed in previous sections. These problems involve the large displacement and large rotation responses of structures. To validate the membrane element, a numerical example of a membrane loaded with corner forces is used. The numerical results given by the membrane element are compared to the results given by the MITC4 shell element.

4.5.1. Large Deflection Analysis of a Simply-Supported Plate

This example is used to test the MITC4 shell element. A simply-supported square plate subjected to a uniformly distributed pressure is shown in Figure 4.3. The plate edges experience no in-plane displacements. The parameters of this problem are: Young's modulus $E = 10^7$ Pa, Poisson's ratio $\mu = 0.316$, plate thickness $h = 0.12$ m, and plate width $a = 24$ m. A 10×10 mesh is used for the plate. The maximum transverse deflection occurs at the center of the plate. Figure 4.4 shows the maximum deflection response given by the MITC4 shell element. This numerical result is very close to the solutions given by Levy [50].

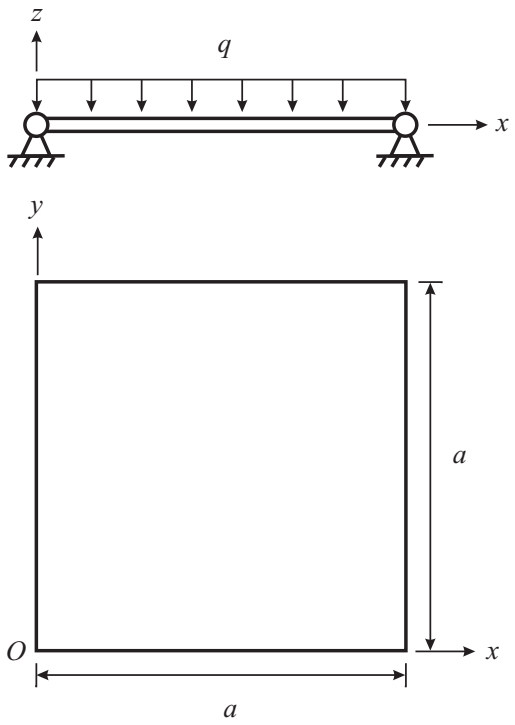

Figure 4.3. A simply-supported plate under pressure loading

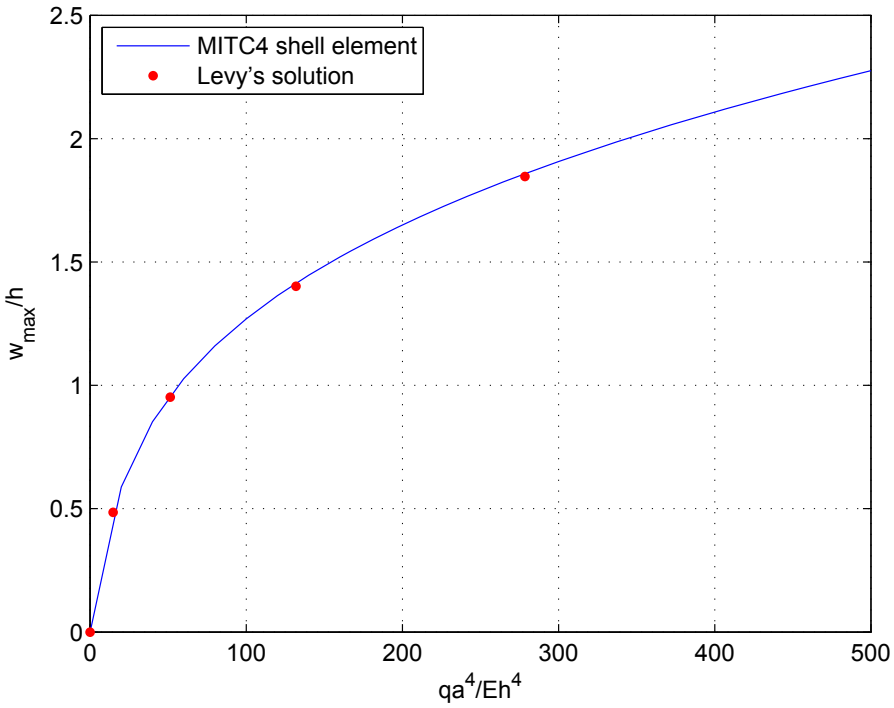

Figure 4.4. Analysis results of a simply-supported square plate subjected to pressure loading

4.5.2. Large Displacement/Rotation Analysis of a Cantilever

This example is used to test the MITC4 shell element and the four-node beam element. A cantilever subjected to an end moment is depicted in Figure 4.5. The parameters are: Young's modulus $E = 1.2\times10^6$ Pa, Poisson's ratio $\mu = 0$, plate length $L = 12$m, plate width $b = 1$ m, and plate thickness $h = 0.1$. When the beam element is used in the analysis, the cantilever is discretized into 5 elements. When the MITC4 shell element is used, the cantilever is modeled by a 16×1 mesh. The numerical results in Figure 4.6 show good agreement with the analytical solution presented in [51].

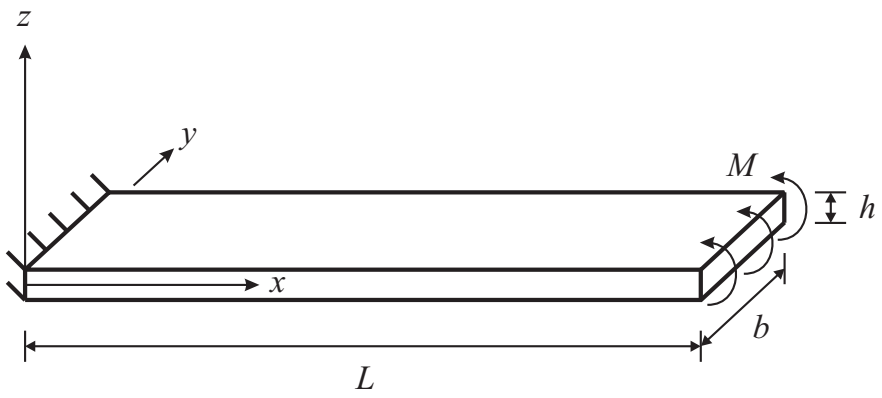

Figure 4.5. A cantilever subjected to an end moment

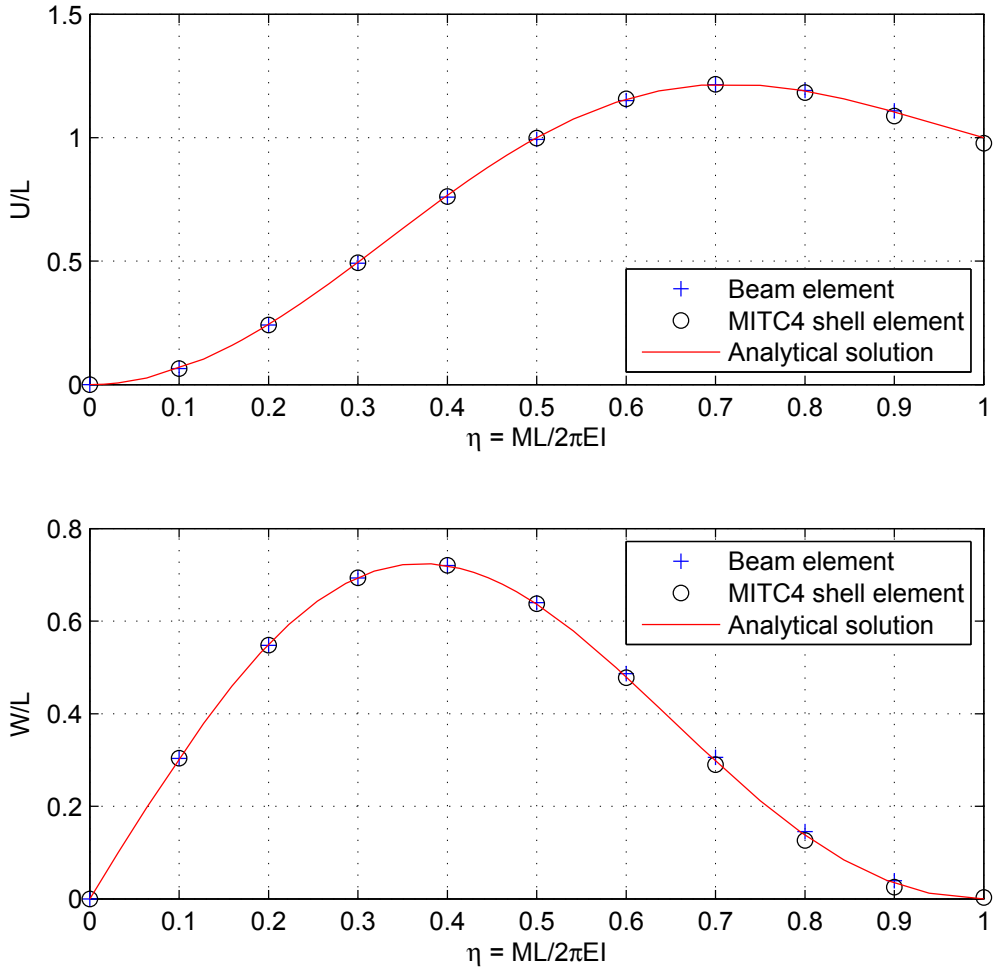

Figure 4.6. Analysis results of a cantilever subjected to an end moment

4.5.3. Nonlinear Analysis of a Simple Arch Structure

This example is used to test the two-node truss element. A two-bar arch structure subjected to a compressive load is shown in Figure 4.7. The parameters are: a = 2500 mm, b = 5 mm, cross section area A = 1 mm^2, and Young's modulus $E = 5\times10^7$ Pa. The numerical results given by the truss element are compared to the analytical solution in [52]. Good agreement can be observed between the finite element result and the analytical solution.

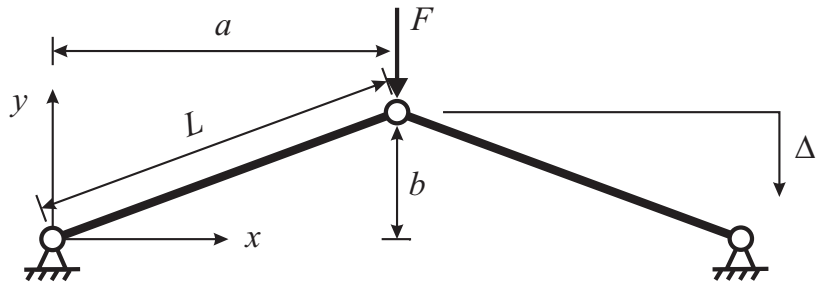

Figure 4.7. A simple arch structure

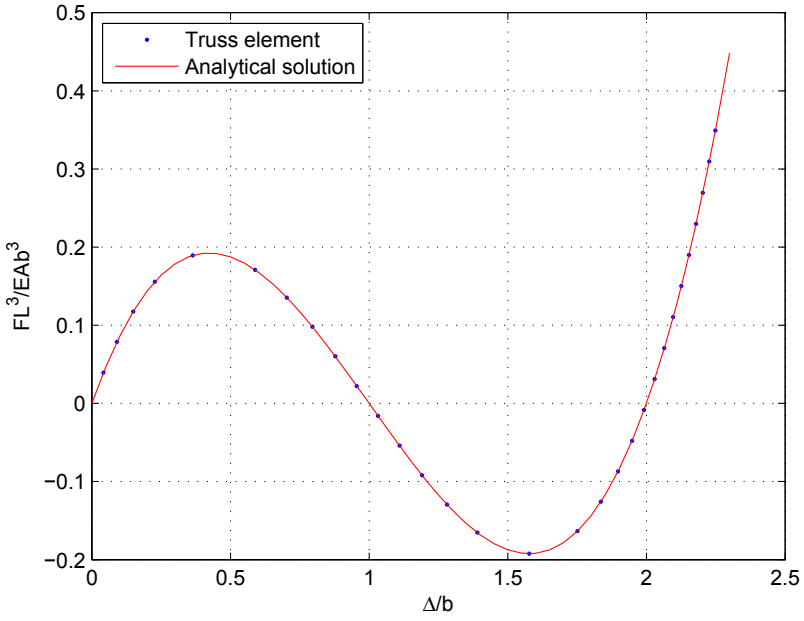

Figure 4.8. Analysis results of a simple arch structure

4.5.4. Large Displacement Analysis of a Square Membrane

This example is used to test the four-node membrane element. A square membrane subjected corner forces is shown in Figure 4.9. The displacement boundary conditions are: corner *O* is fixed, corner *A* is free in *Ox* axis, corner *B* is free in three directions, and corner *C* is free in *Oy* axis. The corner forces are: F = 2.749 N and F_w = 0.1 N. The parameters are: Young's modulus $E = 1.65\times10^8$ Pa, Poisson's ratio $\mu = 0.34$, membrane

width a = 2 m, membrane thickness h = 51 μm. A 20×20 mesh is used to model the membrane. The deflections of the nodes are shown in Figure 4.10 - Figure 4.12. The numerical results given by the membrane element are compared to the results given by the MITC4 shell element. It can be seen that these two sets of results are very close.

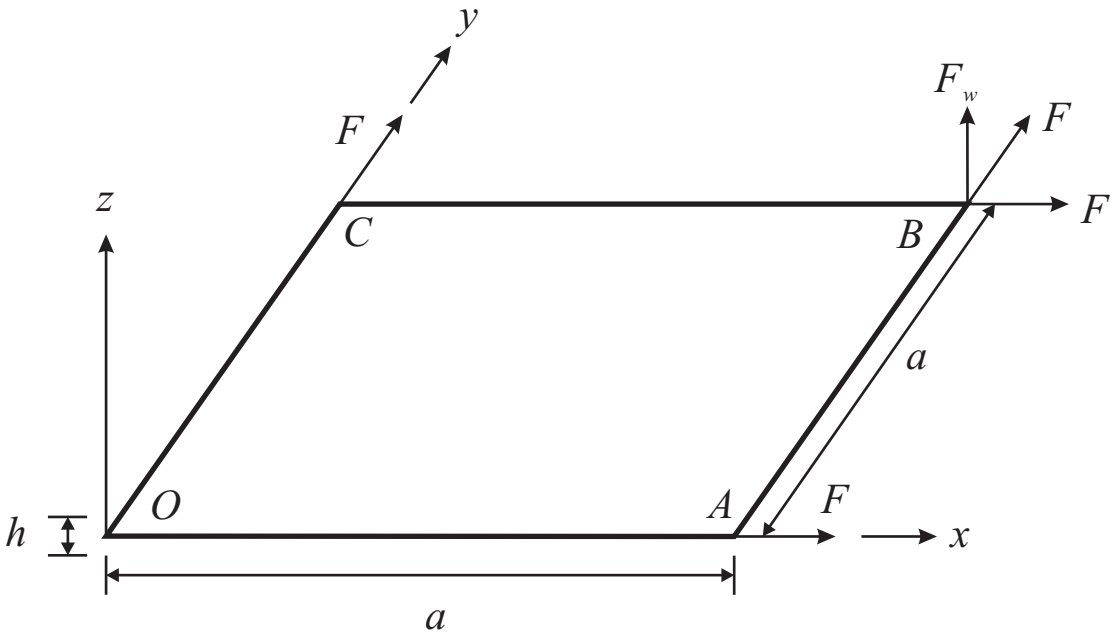

Figure 4.9. A membrane under corner force loading

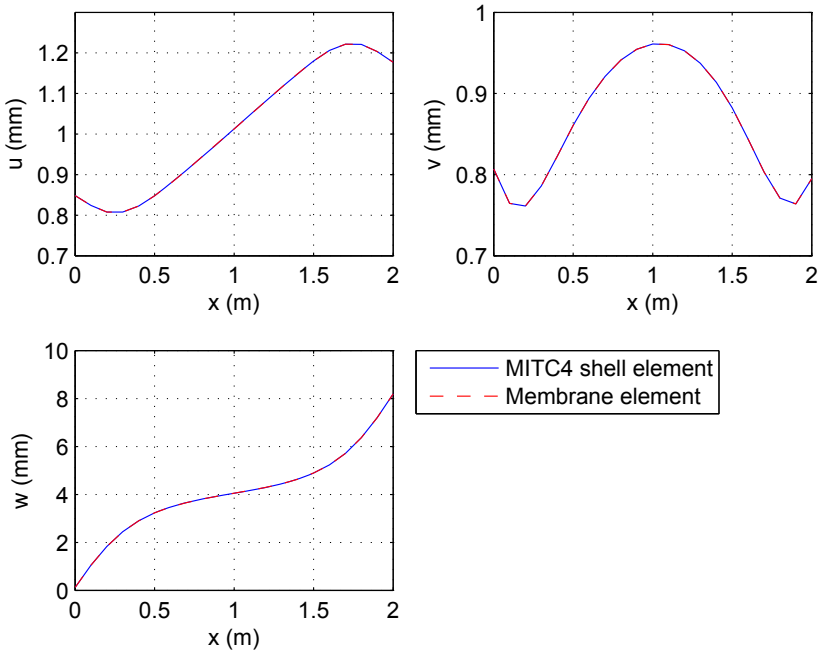

Figure 4.10. Deflections of the nodes on the line $y = 0.4$ m

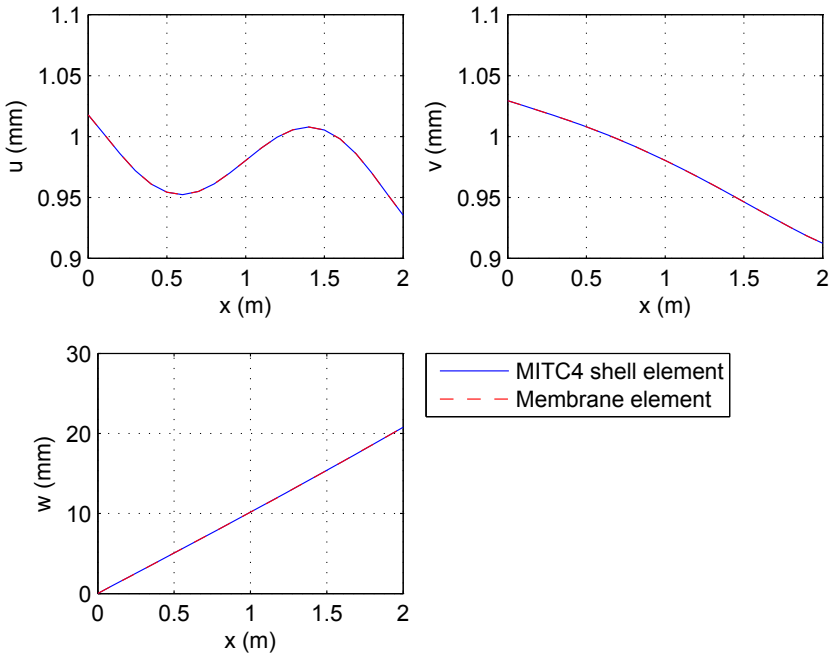

Figure 4.11. Deflections of the nodes on the line $y = 1.0$ m

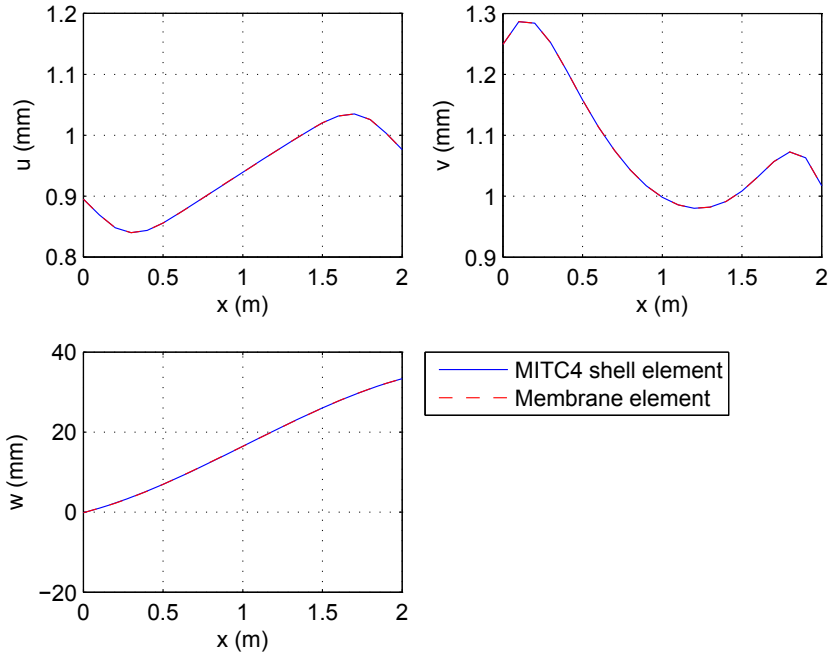

Figure 4.12. Deflections of the nodes on the line $y = 1.6$ m

4.6. Conclusions

In this chapter, two nonlinear finite element models, i.e. the shell-beam-cable model and the membrane-truss-cable model, are developed to study the dynamics of tensegrity-membrane systems. The total Lagrangian formulation is implemented to carry out the nonlinear finite element analysis. The shell-beam-cable model is of great generality, since no specific modeling assumptions are made for system components. Since specific modeling assumptions for the membranes and the bars are introduced to simplify the problem, the membrane-truss-cable model can be treated as a simplified shell-beam-cable model. Four benchmark problems are used to test the structural elements discussed in this work. It can be observed that, in each example, the numerical results given by the structural elements used in this work are very close to the reference results.

Chapter 5: Control-Oriented Model

5.1. Introduction

In Chapter 4, two nonlinear finite element models are developed for tensegrity-membrane systems. These two models can capture most of the system nonlinearities, especially the geometric nonlinearity of the attached membrane. However, the nonlinear finite element method usually requires fine meshes to be implemented for the system, so the resulting mathematical models are high-dimensional. Moreover, the formulation of the nonlinear finite element method is based on an iterative numerical procedure and there is no explicit nonlinear equations of motion in ODE form. Thus, these two features of the nonlinear finite element method prevent the direct use of nonlinear finite element models for system control design.

The necessity of using the nonlinear finite element method for system analysis is mainly due to the flexibility of the attached membrane, especially its geometric nonlinearity. It is well known that the in-plane stiffness of a thin sheet is commonly larger than its transverse bending stiffness and transverse shear stiffness [49]. Furthermore, if appropriate controls are applied, tensegrity-membrane systems can be regulated around equilibriums, so only small amplitude vibrations of the system need to be considered. This means that the linear elastic model and the infinitesimal strain assumption may be applied to the attached membrane, and the modal expansion technique could be used to reduce the number of state variables of the resulting mathematical model. Therefore, tensegrity-membrane systems can be treated as linear

flexible multibody systems based on these assumptions, and a control-oriented model can be developed to facilitate control design.

In this chapter, the development of a control-oriented model for tensegrity-membrane systems is discussed. Lagrange's method, modal coordinates, holonomic constraints, and Lagrange's multiplies are used to derive the equations of motion of the system.

5.2. Model Development

For this control-oriented model, the following four additional modeling assumptions are made:

a) Bars are treated as rigid bodies.

b) The rotational motion of each bar about its longitudinal axis is ignored.

c) The transverse bending stiffness and transverse shear stiffness of the attached membrane are ignored.

d) Tendons are massless (i.e. the dynamics of tendons is ignored).

As mentioned previously, linear elastic laws and infinitesimal strain assumptions are used to model the dynamics of the attached membrane. Therefore, the superposition principle and the modal expansion technique are valid. Also the in-plane deflections and the transverse deflections can be separated in the formulation of membrane strain energy.

Based on the method used in [53], the deflections of the membrane u, v, and w in the $O_f x_f$, $O_f y_f$, and $O_f z_f$ directions can be separated into two parts: the prestressing deflections u^s, v^s, w^s, and the relative deflections u^r, v^r, w^r. Since the membrane is modeled as a continuous body, the resulting equations of motion are a set of partial differential equations. In order to convert these partial differential equations into ordinary differential

equations, modal coordinates are used to discretize the relative deflections. Thus, we can express the deflections in the following form:

$$\begin{aligned}\begin{bmatrix} u & v & w \end{bmatrix}^T &= \begin{bmatrix} u^s + u^r & v^s + v^r & w^s + w^r \end{bmatrix}^T \\ &= \begin{bmatrix} u^s + \sum_{i=1}^{K} \phi_u^i \eta_i & v^s + \sum_{i=1}^{K} \phi_v^i \eta_i & w^s + \sum_{i=1}^{K} \phi_w^i \eta_i \end{bmatrix}^T \\ &= \begin{bmatrix} u^s & v^s & w^s \end{bmatrix}^T + \sum_{i=1}^{K} \boldsymbol{\phi}_i \eta_i \end{aligned} \tag{5.1}$$

where $\boldsymbol{\phi}_i = \begin{bmatrix} \phi_u^i & \phi_v^i & \phi_w^i \end{bmatrix}^T$. Here η_i is the modal coordinate of the relative deflections, and ϕ_u^i, ϕ_v^i, ϕ_w^i are mode shapes of the relative deflections.

The kinetic energy of the membrane can be written as:

$$T_m = \frac{1}{2} \rho \iiint_V \left(\left(\frac{\partial \boldsymbol{r}}{\partial t} \right)^T \frac{\partial \boldsymbol{r}}{\partial t} \right) dv \tag{5.2}$$

where ρ is the density of the membrane and

$$\boldsymbol{r} = \boldsymbol{OO}_f + \boldsymbol{R}_{ef} \boldsymbol{r}_f; \quad \boldsymbol{r}_f = \begin{bmatrix} x_f + u & y_f + v & w \end{bmatrix}^T \tag{5.3}$$

The strain energy of the membrane due to in-plane prestressing can be expressed as:

$$U_{uv}^s = \frac{E}{2\left(1-\mu^2\right)} \iiint_V \left(\varepsilon_{xx}^{s\,2} + 2\mu \varepsilon_{xx}^s \varepsilon_{yy}^s + \varepsilon_{yy}^{s\,2} + 2\left(1-\mu\right) \varepsilon_{xy}^{s\,2} \right) dv \tag{5.4}$$

Here E, μ, and ε represent Young's modulus, Poisson's ratio, and strain components, respectively. Superscript s represents the components due to prestressing.

Since the transverse deflections of membranes are primarily due to the in-plane prestressing effect, which is also known as initial stress, according to the method in [54], the energy due to the transverse prestressing introduced by the free corners B_{Mi} ($i = 2, \ldots, N-2$) can be written as:

$$U_w^s = \frac{1}{2}\iiint_V \left(\tau_{xx}^s \left(\frac{\partial w^s}{\partial x} \right)^2 + 2\tau_{xy}^s \frac{\partial w^s}{\partial x}\frac{\partial w^s}{\partial y} + \tau_{yy}^s \left(\frac{\partial w^s}{\partial y} \right)^2 \right) dv \tag{5.5}$$

where τ represents stress components.

The energy due to the relative motion is:

$$\begin{aligned} U^r &= U_{uv}^r + U_w^r \\ U_{uv}^r &= \frac{E}{2\left(1-\mu^2\right)} \iiint_V \left(\varepsilon_{xx}^{r\,2} + 2\mu\varepsilon_{xx}^r\varepsilon_{yy}^r + \varepsilon_{yy}^{r\,2} + 2\left(1-\mu\right)\varepsilon_{xy}^{r\,2} \right) dv \\ U_w^r &= \frac{1}{2}\iiint_V \left(\tau_{xx}^s \left(\frac{\partial w^r}{\partial x} \right)^2 + 2\tau_{xy}^s \frac{\partial w^r}{\partial x}\frac{\partial w^r}{\partial y} + \tau_{yy}^s \left(\frac{\partial w^r}{\partial y} \right)^2 \right) dv \end{aligned} \tag{5.6}$$

where superscript *r* represents the components due to relative motion.

Note that the in-plane vibration due to the prestressing effect is not considered in Eq. (5.6). This is because in general the vibration frequencies due to the prestressing effect are much higher than the vibration frequencies due to the continuum elasticity. Usually, the vibration modes with higher frequencies are neglected in the modal expansion technique.

The strain components in Eq. (5.4) and Eq. (5.6) are:

$$\varepsilon_{xx}^i = \frac{\partial u^i}{\partial x_f}; \quad \varepsilon_{yy}^i = \frac{\partial v^i}{\partial y_f}; \quad \varepsilon_{xy}^i = \frac{1}{2}\left(\frac{\partial u^i}{\partial y_f} + \frac{\partial v^i}{\partial x_f} \right); \quad \left(i = s, r\right) \tag{5.7}$$

and the stress components are:

$$\tau_{xx}^s = \frac{E}{1-\mu^2}\left(\varepsilon_{xx}^s + \mu\varepsilon_{yy}^s\right); \quad \tau_{yy}^s = \frac{E}{1-\mu^2}\left(\varepsilon_{yy}^s + \mu\varepsilon_{xx}^s\right); \quad \tau_{xy}^s = \frac{E}{\left(1+\mu\right)}\varepsilon_{xy}^s \tag{5.8}$$

The linear finite element method is employed to find the stress and displacement components in Eqs. (5.4), (5.5), and (5.6). Since the geometric nonlinearity of the

membrane is ignored, the domain of integration is chosen to be the shape of the undeformed membrane.

When $M = 1$, the kinetic energy of the bars, T_b, is:

$$T_b = \sum_{j=1}^{N} \frac{1}{6} m_{1j} {l_{1j}}^2 \left({\dot{\theta}_{1j}}^2 + {\dot{\psi}_{1j}}^2 \sin^2 \theta_{1j} \right) \tag{5.9}$$

When $M \geq 2$, T_b can be written as:

$$T_b = m_{ij} \left(\sum_{i=1}^{M} \sum_{j=1}^{N} \frac{1}{6} \tilde{T}_1 + \sum_{i=2}^{M} \sum_{j=1}^{N} \frac{1}{2} \tilde{T}_2 \right) \tag{5.10}$$

where

$$\begin{aligned} \tilde{T}_1 &= {l_{ij}}^2 \left({\dot{\theta}_{ij}}^2 + {\dot{\psi}_{ij}}^2 \sin^2 \theta_{ij} \right) \\ \tilde{T}_2 &= {\dot{x}_{ij}}^2 + {\dot{y}_{ij}}^2 + {\dot{z}_{ij}}^2 + l_{ij} \dot{x}_{ij} \left(\dot{\theta}_{ij} \cos\theta_{ij} \cos\psi_{ij} - \dot{\psi}_{ij} \sin\theta_{ij} \sin\psi_{ij} \right) \\ &\quad + l_{ij} \dot{y}_{ij} \left(\dot{\theta}_{ij} \cos\theta_{ij} \sin\psi_{ij} + \dot{\psi}_{ij} \sin\theta_{ij} \cos\psi_{ij} \right) - l_{ij} \dot{z}_{ij} \dot{\theta}_{ij} \sin\theta_{ij} \end{aligned} \tag{5.11}$$

The symbols m_{ij} and l_{ij} in Eqs. (5.9) - (5.11) represent the mass and the length of bar b_{ij}, respectively.

The strain energy of the tendons, U_{td}, is shown in Eq. (3.6). According to Eq. (3.5), we have $3N-3$ algebraic constraint equations at B_{Mi}, labeled as Φ_i ($i = 1, 2 \ldots 3N-3$). Then, the Lagrangian function of this holonomic system is:

$$L = T_m + T_b - U_{uv}^s - U_w^s - U^r - U_{td} + \sum_{i=1}^{3N-3} \lambda_i \Phi_i \tag{5.12}$$

The Rayleigh dissipation function, R, is used to include damping effect of the membrane. It is assumed that the damping ratio of each modal coordinate, c_m, is the same:

$$R = \frac{1}{2} \rho c_m \iiint_V \left(\left(\frac{\partial u^r}{\partial t} \right)^2 + \left(\frac{\partial v^r}{\partial t} \right)^2 + \left(\frac{\partial w^r}{\partial t} \right)^2 \right) dv \tag{5.13}$$

The generalized coordinates are:

$$\begin{aligned}
&\boldsymbol{x} = \begin{bmatrix} \boldsymbol{z}^T & \boldsymbol{\zeta}^T \end{bmatrix}^T \\
&\boldsymbol{z} = \begin{bmatrix} \boldsymbol{q}^T & \eta_1 & \cdots & \eta_K \end{bmatrix}^T \\
&\boldsymbol{\zeta} = \begin{bmatrix} \Delta_1^u & \Delta_2^u & \Delta_2^v & \Delta_2^w & \cdots & \Delta_{N-1}^u & \Delta_{N-1}^v & \gamma_1 & \gamma_2 & \gamma_3 \end{bmatrix}^T
\end{aligned} \tag{5.14}$$

where $\boldsymbol{z}$ is the vector of independent coordinates and $\boldsymbol{\zeta}$ is the vector of dependent coordinates.

If K modal coordinates are used for membrane relative deflections, we end up with $(5M+3)N+K-6$ differential-algebraic equations:

$$\begin{aligned}
&\frac{d}{dt}\left(\frac{\partial L}{\partial \dot{x}_i}\right) - \frac{\partial L}{\partial x_i} + \frac{\partial R}{\partial \dot{x}_i} = 0; \qquad (i = 1, 2, \ldots 5MN + K - 3) \\
&\frac{\partial L}{\partial \lambda_j} = 0; \qquad (j = 1, 2, \ldots 3N - 3)
\end{aligned} \tag{5.15}$$

Note that the relative deflections of a generic point on the membrane, $P_i\left(x_f^i, y_f^i\right)$, can be expressed as (see Eq. (5.1)):

$$u_i^r = \sum_{j=1}^{K} \phi_u^j\left(x_f^i, y_f^i\right)\eta_j; \quad v_i^r = \sum_{j=1}^{K} \phi_v^j\left(x_f^i, y_f^i\right)\eta_j; \quad w_i^r = \sum_{j=1}^{K} \phi_w^j\left(x_f^i, y_f^i\right)\eta_j \tag{5.16}$$

According to Eq. (5.16), we can find K points on the membrane and get $3K$ membrane relative deflections. Then, if the first K modes are used, we can choose K components from the $3K$ membrane relative deflections and rearrange Eq. (5.16) as:

$$\begin{aligned}
&\boldsymbol{v} = \boldsymbol{T}_{v\eta}\boldsymbol{\eta} \\
&\boldsymbol{v} = \begin{bmatrix} u_1^r & \cdots & u_{k_1}^r & v_1^r & \cdots & v_{k_1}^r & w_1^r & \cdots & w_{k_1}^r \end{bmatrix}^T; \quad \left(k_1 + k_2 + k_3 = K\right) \\
&\boldsymbol{\eta} = \begin{bmatrix} \eta_1 & \cdots & \eta_K \end{bmatrix}^T
\end{aligned} \tag{5.17}$$

These K points and the corresponding membrane relative deflections can be chosen to ensure that matrix $\boldsymbol{T}_{v\eta}$ is invertible. Thus, these K membrane relative deflections can be

used as generalized coordinates instead of the modal coordinates. In other words, another set of generalized coordinates can be expressed as:

$$\begin{aligned}\tilde{\boldsymbol{x}} &= \begin{bmatrix}\tilde{\boldsymbol{z}}^T & \boldsymbol{\zeta}^T\end{bmatrix}^T \\ \tilde{\boldsymbol{z}} &= \begin{bmatrix}\boldsymbol{q}^T & \boldsymbol{v}^T\end{bmatrix}^T \\ \boldsymbol{\zeta} &= \begin{bmatrix}\Delta_1^u & \Delta_2^u & \Delta_2^v & \Delta_2^w & \cdots & \Delta_{N-1}^u & \Delta_{N-1}^v & \gamma_1 & \gamma_2 & \gamma_3\end{bmatrix}^T\end{aligned} \tag{5.18}$$

System dynamics is not affected by the choice of the two sets of generalized coordinates in Eq. (5.14) and Eq. (5.18). The coordinates in Eq. (5.14) are useful for system analysis due to the properties of mode shapes, while the coordinates in Eq. (5.18) are more suitable for numerical computation and control design.

5.3. Coordinate Partitioning and Coordinate Mapping

Since holonomic constraints and Lagrange's multipliers are introduced, the equations of motion of the control-oriented model are a set of differential-algebraic equations (DAEs). Since most control theories are developed based on ordinary differential equations (ODEs), a coordinate partitioning and coordinate mapping technique is used to convert the DAEs to ODEs. This technique is similar to those used in [55- 58].

After rearranging Eq. (5.15) in matrix form, the equations of motion of tensegrity-membrane systems can be written as

$$\begin{aligned}&\boldsymbol{M}(\boldsymbol{x})\ddot{\boldsymbol{x}} + \boldsymbol{F}(\boldsymbol{x}, \dot{\boldsymbol{x}}) + \left(\frac{\partial \boldsymbol{\Phi}(x)}{\partial \boldsymbol{x}}\right)^T \boldsymbol{\lambda} + \boldsymbol{B}(\boldsymbol{x})\boldsymbol{u} = \boldsymbol{O} \\ &\boldsymbol{\Phi}(\boldsymbol{x}) = \boldsymbol{O}\end{aligned} \tag{5.19}$$

where $\boldsymbol{\Phi}(x)$ is the vector of constraint equations and the control input $\boldsymbol{u}$ is the vector of tendon rest-lengths.

Since the strain energy in tendons, U_{td}, in Eq. (3.6) is a function of $\boldsymbol{q}$, the tendon rest-lengths appear in the equations of motion corresponding to $\boldsymbol{q}$. Therefore, for the independent coordinates, $\boldsymbol{z}$, the locations and attitudes of bars, x_{ij}, y_{ij}, z_{ij}, θ_{ij} and ψ_{ij}, can be directly controlled via tendon rest-length control, while the modal coordinates of the membrane η_i are the underactuated coordinates.

Then, the vector of generalized coordinates $\boldsymbol{x}$ can be partitioned as:

$$\boldsymbol{x} = \begin{bmatrix} \boldsymbol{q}^T & \boldsymbol{\eta}^T & \boldsymbol{\zeta}^T \end{bmatrix}^T \tag{5.20}$$

Note that $\boldsymbol{q}$ is the vector of actuated independent coordinates, $\boldsymbol{\eta}$ is the vector of underactuated independent coordinates, and $\boldsymbol{\zeta}$ is the vector of dependent coordinates. After partitioning, the matrices $\boldsymbol{M}(\boldsymbol{x})$, $\boldsymbol{F}(\boldsymbol{x})$, and $\boldsymbol{B}(\boldsymbol{x})$ in Eq. (5.19) are:

$$\boldsymbol{M}(\boldsymbol{x}) = \begin{bmatrix} \boldsymbol{M}_{11} & \boldsymbol{M}_{12} & \boldsymbol{M}_{13} \\ \boldsymbol{M}_{12}{}^T & \boldsymbol{M}_{22} & \boldsymbol{M}_{23} \\ \boldsymbol{M}_{13}{}^T & \boldsymbol{M}_{23}{}^T & \boldsymbol{M}_{33} \end{bmatrix}; \quad \boldsymbol{F}(\boldsymbol{x}) = \begin{bmatrix} \boldsymbol{F}_1 \\ \boldsymbol{F}_2 \\ \boldsymbol{F}_3 \end{bmatrix}; \quad \boldsymbol{B}(\boldsymbol{x}) = \begin{bmatrix} \boldsymbol{B}_1 \\ \boldsymbol{O} \\ \boldsymbol{O} \end{bmatrix} \tag{5.21}$$

The relationship between $\boldsymbol{q}$ and $\boldsymbol{\zeta}$ can be determined based on the constraint equation $\boldsymbol{\Phi}(\boldsymbol{x}) = \boldsymbol{O}$. According to Eq. (3.5), it can be easily found that $\boldsymbol{\Phi}(\boldsymbol{x})$ is a function of $\boldsymbol{q}$ and $\boldsymbol{\zeta}$, i.e. $\boldsymbol{\Phi}(\boldsymbol{x}) = \boldsymbol{\Phi}(\boldsymbol{q}, \boldsymbol{\zeta}) = \boldsymbol{O}$. If $\partial\boldsymbol{\Phi}/\partial\boldsymbol{\zeta}$ is invertible, $\boldsymbol{\Phi}(\boldsymbol{q}, \boldsymbol{\zeta}) = \boldsymbol{O}$ can be at least locally solved for $\boldsymbol{\zeta}$ as a function of $\boldsymbol{q}$, i.e. $\boldsymbol{\zeta} = \boldsymbol{\zeta}(\boldsymbol{q})$.

After taking the variation of the constraint equations, we have:

$$\delta\boldsymbol{\Phi}(\boldsymbol{x}) = \frac{\partial\boldsymbol{\Phi}}{\partial\boldsymbol{q}}\delta\boldsymbol{q} + \frac{\partial\boldsymbol{\Phi}}{\partial\boldsymbol{\zeta}}\delta\boldsymbol{\zeta} = \left(\frac{\partial\boldsymbol{\Phi}}{\partial\boldsymbol{q}} + \frac{\partial\boldsymbol{\Phi}}{\partial\boldsymbol{\zeta}}\frac{\partial\boldsymbol{\zeta}}{\partial\boldsymbol{q}}\right)\delta\boldsymbol{q} = \boldsymbol{O} \tag{5.22}$$

Since $\delta\boldsymbol{q}$ can be arbitrary, its coefficient must be zero. Assuming that $\partial\boldsymbol{\Phi}/\partial\boldsymbol{\zeta}$ is invertible, we get:

$$\frac{\partial \boldsymbol{\zeta}}{\partial \boldsymbol{q}} = -\left(\frac{\partial \boldsymbol{\Phi}}{\partial \boldsymbol{\zeta}}\right)^{-1} \frac{\partial \boldsymbol{\Phi}}{\partial \boldsymbol{q}} \tag{5.23}$$

and the time derivatives of $\boldsymbol{\zeta}$ can be written as:

$$\begin{aligned} \dot{\boldsymbol{\zeta}} &= \frac{\partial \boldsymbol{\zeta}}{\partial \boldsymbol{q}} \dot{\boldsymbol{q}} \\ \ddot{\boldsymbol{\zeta}} &= \frac{\partial}{\partial \boldsymbol{q}}\left(\frac{\partial \boldsymbol{\zeta}}{\partial \boldsymbol{q}} \dot{\boldsymbol{q}}\right)\dot{\boldsymbol{q}} + \frac{\partial \boldsymbol{\zeta}}{\partial \boldsymbol{q}} \ddot{\boldsymbol{q}} \end{aligned} \tag{5.24}$$

The time derivatives of the generalized coordinate $\boldsymbol{x}$ are:

$$\dot{\boldsymbol{x}} = \boldsymbol{T}_z \begin{bmatrix} \dot{\boldsymbol{q}} \\ \dot{\boldsymbol{\eta}} \end{bmatrix}; \quad \ddot{\boldsymbol{x}} = \boldsymbol{G} + \boldsymbol{T}_z \begin{bmatrix} \ddot{\boldsymbol{q}} \\ \ddot{\boldsymbol{\eta}} \end{bmatrix} \tag{5.25}$$

where

$$\begin{aligned} \boldsymbol{T}_z &= \begin{bmatrix} \boldsymbol{I} & \boldsymbol{O} \\ \boldsymbol{O} & \boldsymbol{I} \\ \partial \boldsymbol{\zeta} / \partial \boldsymbol{q} & \boldsymbol{O} \end{bmatrix} \\ \boldsymbol{G} &= \begin{bmatrix} \boldsymbol{O} & \boldsymbol{O} & \boldsymbol{g}^T \end{bmatrix}^T \\ \boldsymbol{g} &= \frac{\partial}{\partial \boldsymbol{q}}\left(\frac{\partial \boldsymbol{\zeta}}{\partial \boldsymbol{q}} \dot{\boldsymbol{q}}\right)\dot{\boldsymbol{q}} \end{aligned}$$

It can be easily verified that:

$$\boldsymbol{T}_z^T \left(\frac{\partial \boldsymbol{\Phi}(x)}{\partial \boldsymbol{x}}\right)^T = \boldsymbol{O} \tag{5.26}$$

Therefore, pre-multiplying the first equation in Eq. (5.19) by $\boldsymbol{T}_z^T$ and substituting Eq. (5.26) into the first equation in Eq.(5.19), the equations of motion can be converted into a set of ordinary differential equations in the second order form:

$$\hat{\boldsymbol{M}}\ddot{\boldsymbol{z}} + \hat{\boldsymbol{F}} + \hat{\boldsymbol{B}}\boldsymbol{u} = \boldsymbol{O} \tag{5.27}$$

where $\boldsymbol{z}$ is defined in Eq.(5.14) and

$$\hat{\boldsymbol{M}} = \boldsymbol{T}_z^T \boldsymbol{M}(\boldsymbol{x}) \boldsymbol{T}_z$$
$$\hat{\boldsymbol{F}} = \boldsymbol{T}_z^T \left(\boldsymbol{F}(\boldsymbol{x}, \dot{\boldsymbol{x}}) + \boldsymbol{M}(\boldsymbol{x}) \boldsymbol{G} \right) \tag{5.28}$$
$$\hat{\boldsymbol{B}} = \boldsymbol{T}_z^T \boldsymbol{B}(\boldsymbol{x})$$

5.4. Conclusions

In this chapter, a control-oriented model is developed for tensegrity-membrane systems. The bars are treated as rigid bodies. Linear elastic laws and infinitesimal strain assumptions are applied to the membrane. Also, the dynamics of tendons is ignored. Equations of motion are derived based on Lagrange's method. Since holonomic constraints and Lagrange's multipliers are employed to carry out the model development, the resulting equations of motion are a set of DAEs. Then, a coordinate partitioning and coordinate mapping technique is used to convert the DAEs into ODEs.

Since the bars are modeled as rigid bodies and modal coordinates are used to describe the membrane relative deflections, the number of generalized coordinates needed for this control-oriented model is much less than the number of coordinates required for the two nonlinear finite element models discussed in previous chapters. Moreover, thanks to the coordinate partitioning and coordinate mapping technique, the resulting equations of motion can be expressed as a set of ODEs. Therefore, compared to the nonlinear finite element models, this control-oriented model is very suitable for control design. It should be noted that the accuracy and reliability of this control-oriented model still need careful examination, since several modeling assumptions are introduced to simplify the modeling problem. More details of the comparison between the nonlinear finite element models and the control-oriented model can be found in the next chapter.

Chapter 6: Numerical Analysis of Tensegrity-Membrane Systems

6.1. Introduction

This chapter addresses the numerical analysis of system statics, natural frequencies, and mode shapes of tensegrity-membrane systems. The shell-beam-cable model, the membrane-truss-cable model, and the control-oriented model are used to carry out the analysis. Two representative tensegrity-membrane systems are studied: a 1-4 symmetric system and a 2-3 symmetric system.

To examine the equilibrium finding method proposed in Chapter 3, static analysis is first performed using the shell-beam-cable model. The loads exerted on system components are also examined to see whether the designed prestressing condition is reasonable. Since the density of meshes used in finite element analysis can affect the accuracy of analysis results, mesh convergence analysis is conducted using the shell-beam-cable model. Based on the results of the static analysis and the mesh convergence analysis, the three mathematical models are used to study the natural frequencies and mode shapes of the 1-4 symmetric system and the 2-3 symmetric system. Free vibration responses given by the three models are also studied and compared in order to investigate the accuracy and reliability of the membrane-truss-cable model and the control-oriented model.

For the two tensegrity-membrane systems studied in this chapter, the material and geometrical parameters used are shown in Table 6.1.

Table 6.1. Material and geometrical parameters of tensegrity-membrane systems

Components	Parameters	
Membrane	Young's Modulus (E)	165 MPa
	Density (ρ)	1400 kg/m^3
	Thickness (h)	51 μm
	Poisson's ratio (μ)	0.34
Bar	Density	7800 kg/m^3
	Diameter	30 mm
Tendon	Young's Modulus	2 GPa
	Diameter	0.6 mm

6.2. Static Analysis

Static analysis is conducted to check whether the equilibrium finding method and the system statics equations discussed in Chapter 3 are correct. The shell-beam-cable model, which is the model of great generality for tensegrity-membrane systems, is used to perform the analysis for a 1-4 symmetric system and a 2-3 symmetric system. Yield analysis and buckling analysis are also conducted to examine whether the loads exerted on system components cause mechanical failures.

6.2.1. 1-4 Symmetric System

For the 1-4 symmetric system, the square membrane is divided into 4 quadrilaterals, and a 10×10 mesh is used for each quadrilateral. Each bar is modeled by one beam element and each tendon is modeled by three truss elements.

According to the proposed equilibrium finding method in Chapter 3, the equilibrium parameters are listed in Table 6.2.

Table 6.2. Equilibrium parameters for the 1-4 symmetric system

System parameter	Designed value
θ_1	60º
ψ_1	10º
l_1	2.015 m
r_1	0.4286 m
r_1^S	1.529 m
r_{mb}	1.4142 m

The iteration history of the upper end of bar b_{14} is shown in Figure 6.1. It can be seen that the system converges to the designed equilibrium. Thus, for this 1-4 system, the equilibrium finding method proposed in Chapter 3 gives correct equilibrium parameters.

The static configuration of the 1-4 symmetric system is shown in Figure 6.2. The thick black lines are the bars and the thin blue lines indicate the tendons. It should be noted that, since the membrane corner forces are designed to be small, the edge curvature is not significant and cannot be clearly seen in the figure.

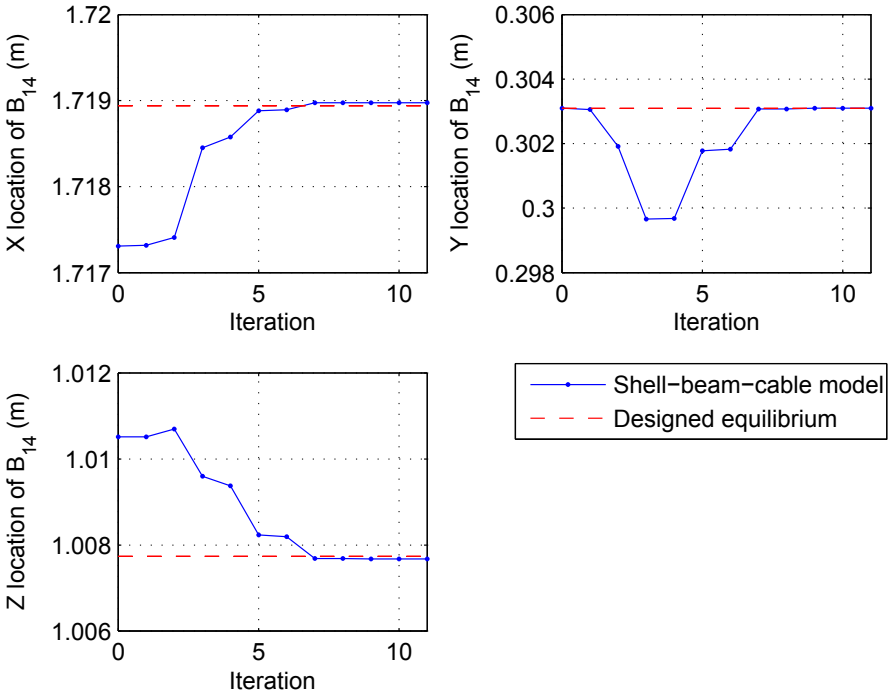

Figure 6.1. Iteration history of the location of B_{14}

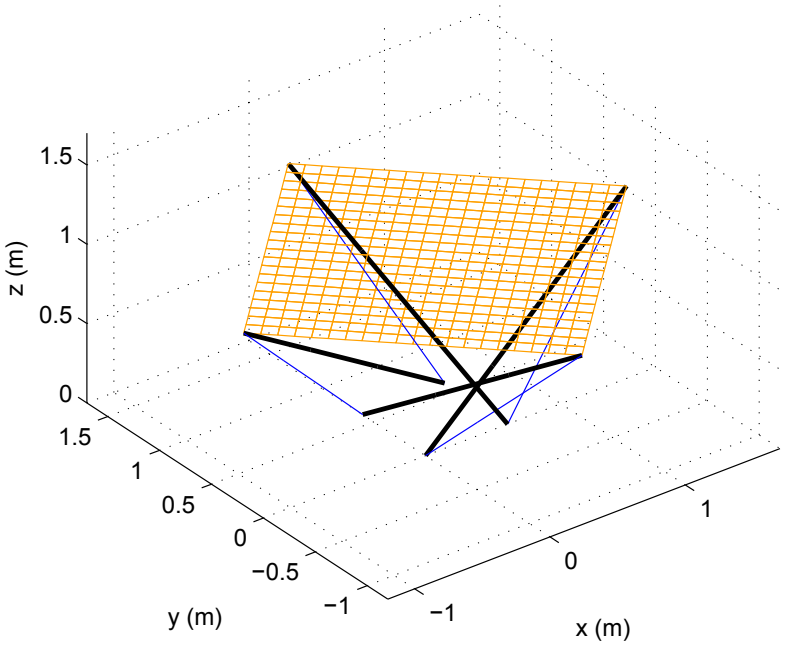

Figure 6.2. Static configuration of the 1-4 symmetric system

Yield and buckling analysis results of bars, tendons, and the membrane are shown in Table 6.3. For the membrane, the maximum principal stress criterion and the von Mises criterion are used to check whether the membrane yields under prestressing. The principal stresses are σ_{P1}, σ_{P2}, and σ_{P3} $(\sigma_{P1} \geq \sigma_{P2} \geq \sigma_{P3})$. The membrane yield stress, i.e. the yield stress at 3% of Kapton, is 61MPa [74].

The maximum principal stress criterion can be expressed as:

$$\sigma_{P1} \leq \sigma_Y \tag{5.29}$$

where σ_Y is the yield stress.

The von Mises criterion can be expressed as:

$$\sigma_v = \sqrt{\frac{(\sigma_{P1} - \sigma_{P2})^2 + (\sigma_{P2} - \sigma_{P3})^2 + (\sigma_{P3} - \sigma_{P1})^2}{2}} \leq \sigma_Y \tag{5.30}$$

The stress distribution of the membrane in the floating reference frame O_f-$x_f y_f z_f$ is shown in Figure 6.3. The principal stresses and the von Mises stress of the membrane in the frame O_f-$x_f y_f z_f$ are plotted in Figure 6.4.

The critical load of bars is determined by Euler's column formula, which can be written as:

$$F_{crit} = \frac{\pi^2 EI}{Kl^2} \tag{5.31}$$

where E is Young's Modulus, I is the area moment of inertia of bars, l is the length of columns, and K = 1.0 for hinged columns.

For tendons, the tendon stress is compared with the yield stress of Nylon, which is 94.8 MPa [75], in order to check whether the tendons are in the linear elastic regime.

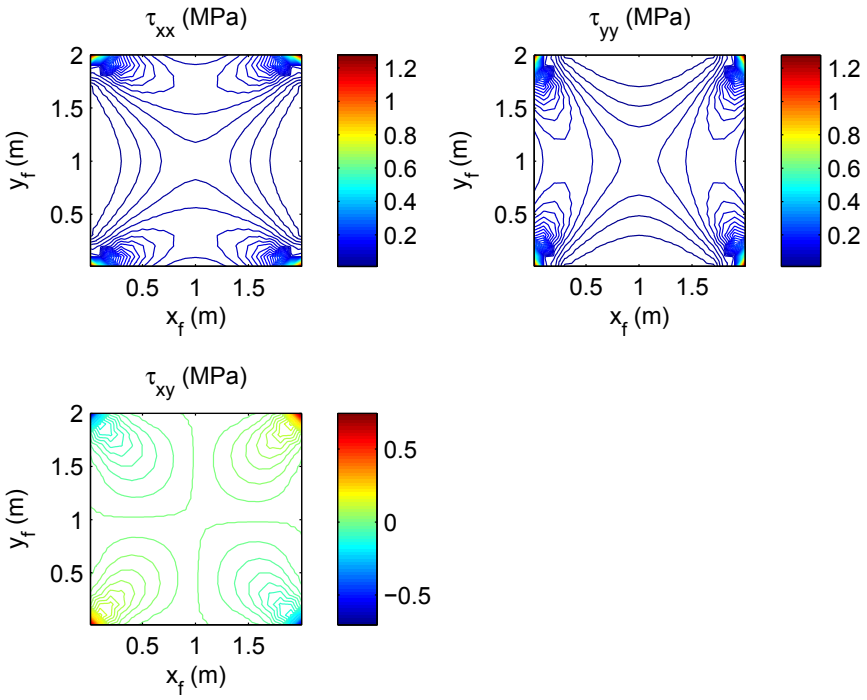

Figure 6.3. Stress distribution of the membrane

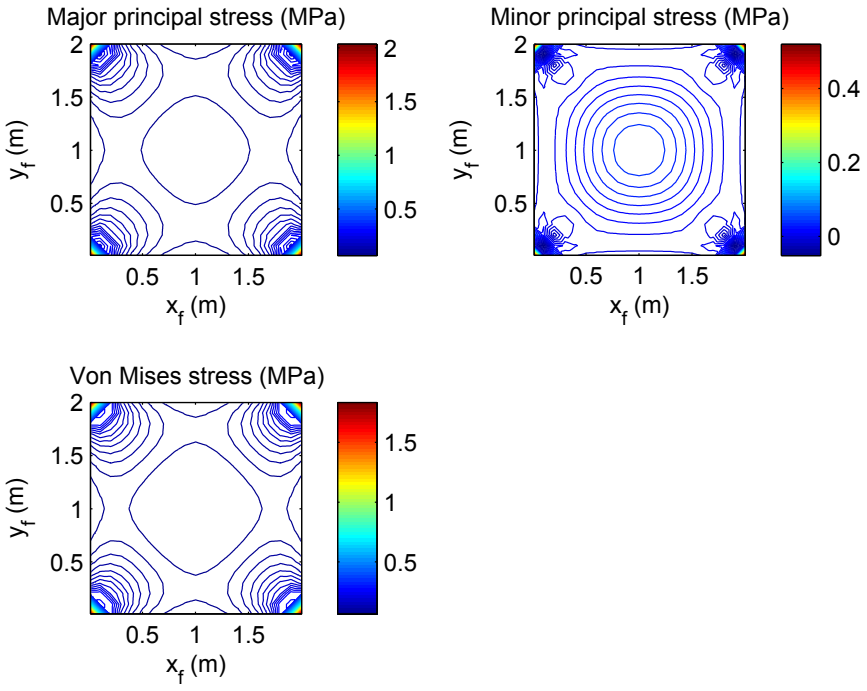

Figure 6.4. Principal stresses and the von Mises stress of the membrane

Table 6.3. Yield and bucking analysis results for the 1-4 symmetric system

Components	Stress/Load	
Membrane	Maximum value of σ_{P1}	2.12 MPa
	Maximum value of σ_v	1.91 MPa
	Yield stress at 3%	61 MPa
Bars	Applied load	14.53 N
	Critical load	19153 N
Tendons	Maximum value of tendon stress	37.98 MPa
	Yield stress	94.8 MPa

It can be seen that, for each yield criterion, stresses σ_{P1} and σ_v are smaller than the yield stress of the membrane. Tendon stress is smaller than the yield stress as well. The applied load on bars is smaller than the critical load predicted by Euler's column formula. Therefore, we can conclude that the designed equilibrium is feasible and the prestressing doesn't cause mechanical failures.

6.2.2. 2-3 Symmetric System

For the 2-3 symmetric system, the triangular membrane is divided into 3 quadrilaterals, and a 10×10 mesh is used for each quadrilateral. Each bar is modeled by one beam element and each tendon is modeled by three truss elements.

According to the proposed equilibrium finding method, the equilibrium parameters are listed in Table 6.4.

Table 6.4. Equilibrium parameters for the 2-3 symmetric system

System parameter	Designed value
θ_1	63º
ψ_1	20º
θ_2	63º
ψ_2	-46.45º
l_1	2.5 m
l_2	2.5 m
r_1	0.7 m
r_2	0.503 m
r_{mb}	1.87 m
σ_2	-66.45º
z_2	0.794 m
r_1^S	1.9425 m
r_2^V	1.9953 m
r_2^D	2.1424 m
r_2^C	0.8204 m
r_2^R	0.8042 m
r_2^P	2.0176 m
r_2^S	2.0939 m

The locations of B_{11}, A_{21}, and B_{21}, i.e. the ends of bar b_{14} and bar b_{21}, are monitored. The iteration history is shown in Figure 6.5 - Figure 6.7. It can be seen that the whole system converges to the designed equilibrium. Thus, for this 2-3 system, it can be concluded that the equilibrium conditions given by the equilibrium finding method presented in Chapter 3 are correct.

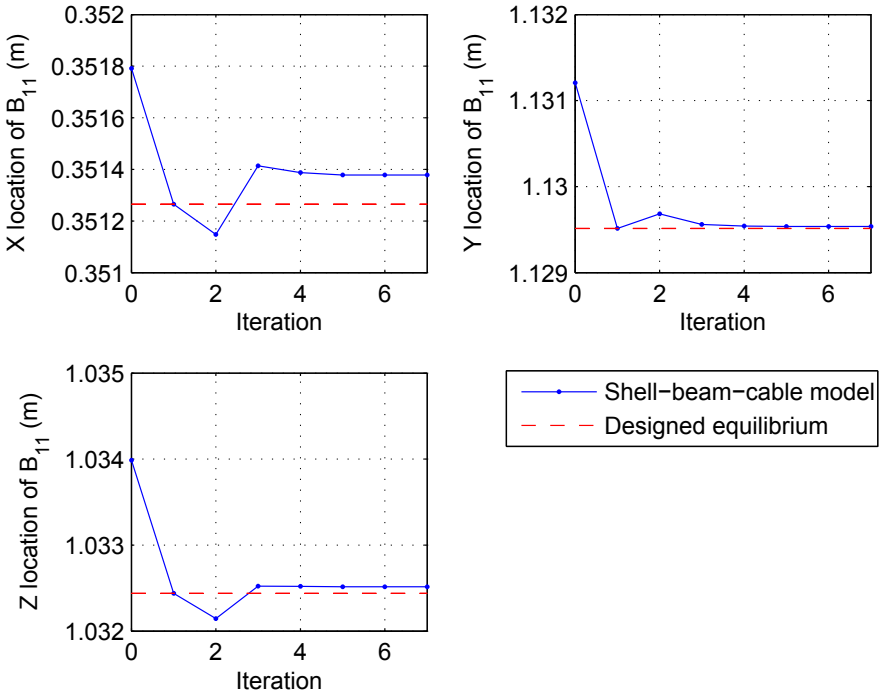

Figure 6.5. Iteration history of the location of B_{11}

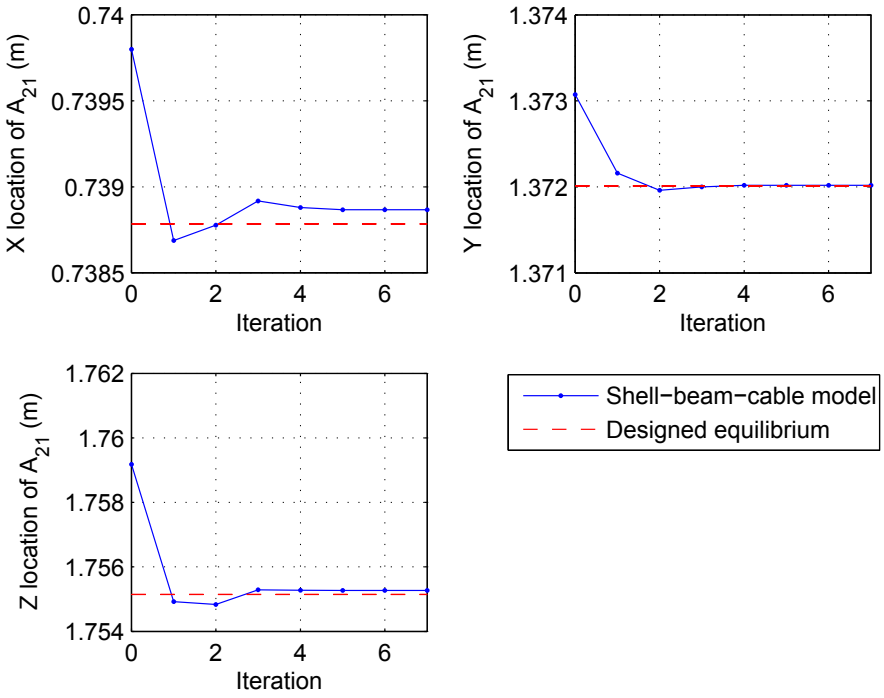

Figure 6.6. Iteration history of the location of A_{21}

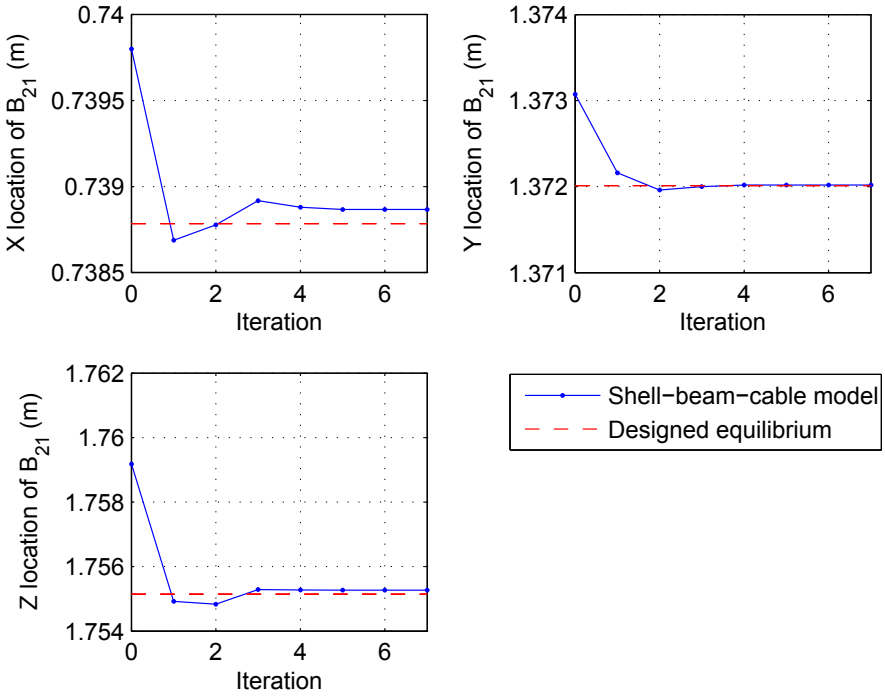

Figure 6.7. Iteration history of the location of B_{21}

The static configuration of the 2-3 system is shown in Figure 6.8. The thick black lines are the bars and the thin blue lines indicate the tendons. Since the forces on the membrane corners are small, the edge curvature is not significant and cannot be clearly seen in the figure.

The stress distribution of the membrane in the floating reference frame O_f-$x_fy_fz_f$ is shown in Figure 6.9. The principal stresses and the von Mises stress of the membrane in the floating reference frame O_f-$x_fy_fz_f$ are plotted in Figure 6.10.

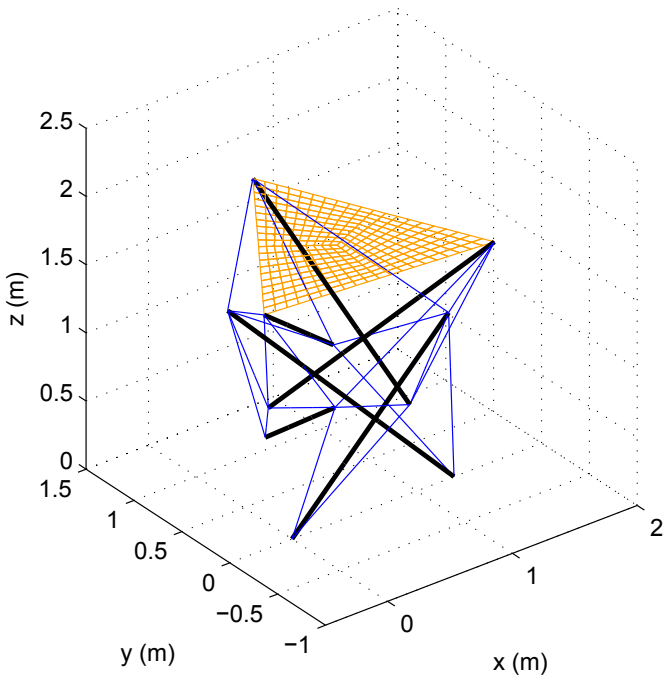

Figure 6.8. Static configuration of the 2-3 symmetric system

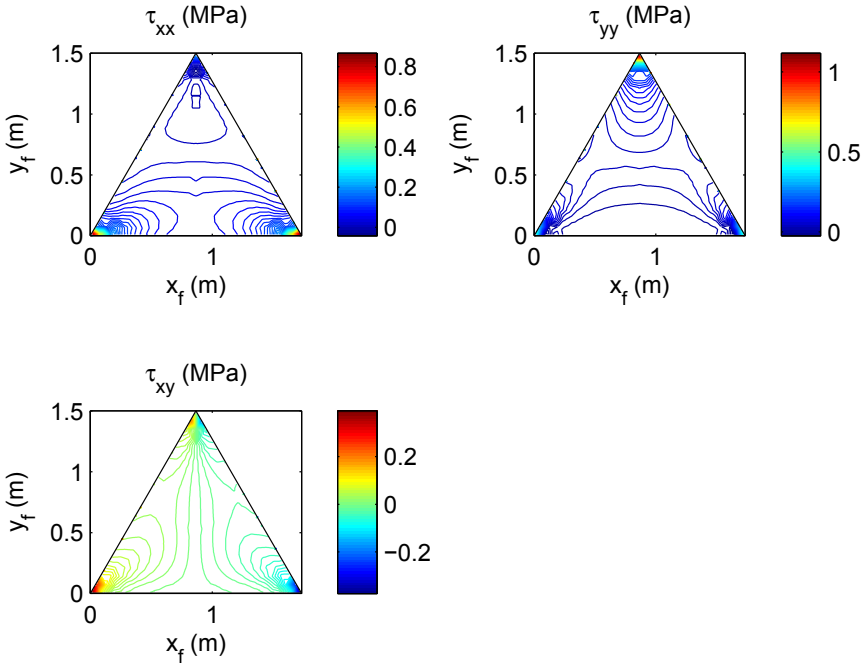

Figure 6.9. Stress distribution of the membrane

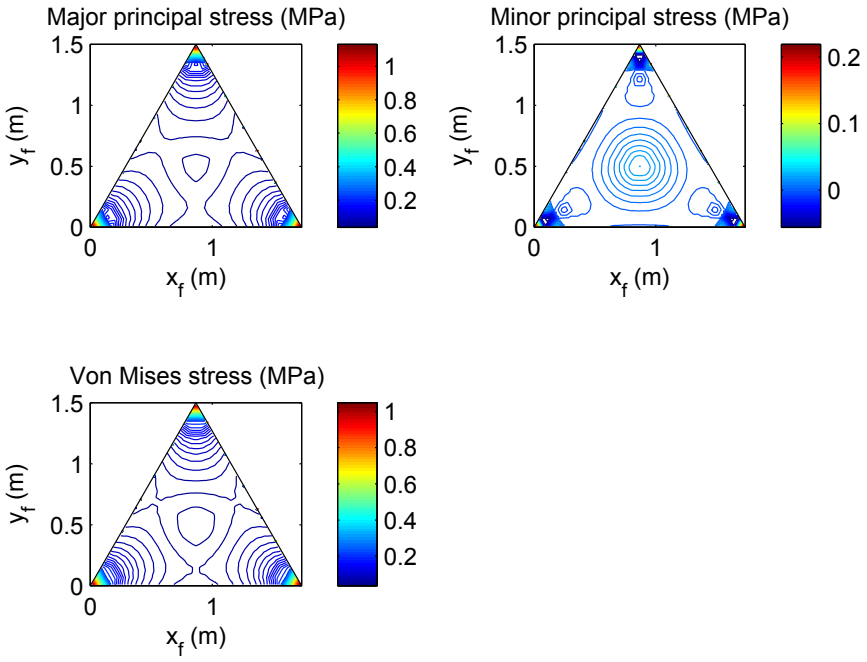

Figure 6.10. Principal stresses and the von Mises stress of the membrane

Yield and buckling analysis results of bars, tendons, and the membrane are shown in Table 6.5. The criteria used for the 2-3 symmetric system are the same as those used for the 1-4 symmetric system in the previous section.

It can be seen that, for each yield theory, the reference stress is smaller than the yield stress of the membrane. Tendon stress is smaller than the yield stress as well. The applied load on bars is smaller than the critical load predicted by Euler's column formula. Therefore, we can conclude that the designed equilibrium is feasible and the prestressing doesn't cause mechanical failures.

Table 6.5. Yield and bucking analysis results for the 2-3 symmetric system

Components	Stress/Load	
Membrane	Maximum value of σ_{P1}	1.25 MPa
	Maximum value of σ_v	1.15 MPa
	Yield stress at 3%	61 MPa
Bars	Applied load on b_{1j}	14.48 N
	Applied load on b_{2j}	5.02 N
	Critical load	19153 N
Tendons	Maximum value of tendon stress	33.58 MPa
	Yield stress	94.8 MPa

6.3. Mesh Convergence Analysis

This section addresses the mesh convergence analysis for the 1-4 system and the 2-3 system. To examine the impact of mesh density on the analysis results of the whole system, the convergence of system natural frequencies is investigated and compared using the shell-beam-cable model.

The tangent stiffness matrix at the designed equilibrium is used to find system natural frequencies. According to Eq. (4.6), the tangent stiffness matrix $\boldsymbol{K_T}$ can be expressed as: $\boldsymbol{K_T} = {}_0^t\boldsymbol{K_L} + {}_0^t\boldsymbol{K_{NL}}$. Thus, solving the following equation yields the model analysis results of tensegrity-membrane systems:

$$\left(\boldsymbol{M}\omega^2 - \boldsymbol{K_T}\right)\boldsymbol{\phi} = \boldsymbol{O} \tag{5.32}$$

where $\boldsymbol{M}$ is the mass matrix expressed in Eq. (4.6). The symbol ω represents the natural frequency of the system and $\boldsymbol{\phi}$ is the eigenvector containing the information of the corresponding mode shape.

Mesh convergence analysis is conducted for the membrane and tendons, while it is not performed for bars. There are two reasons for this decision: 1) deformations of the membrane and tendons are more significant, requiring appropriate meshes to capture the dynamics of the membrane and tendons. For the bars, as discussed previously, their rigid body motions, which are not sensitive to mesh density, are more likely to occur; 2) it has been shown that the four-node beam element used in this work is of high performance and a single four-node beam element can give good results for many beam deformation problems [48].

6.3.1. 1-4 Symmetric System

For the mesh convergence study of the membrane, each bar is modeled by one four-node beam element, and each tendon is modeled using one two-node truss element. The natural frequencies of the first 12 modes are shown in Figure 6.11. It can be seen that, when the element number of the membrane is greater than 400, the natural frequencies of the first 12 modes start to converge. The improvement in the values of natural frequencies is not significant as the element number further increases. Therefore, modeling the membrane using 400 elements is a reasonable choice.

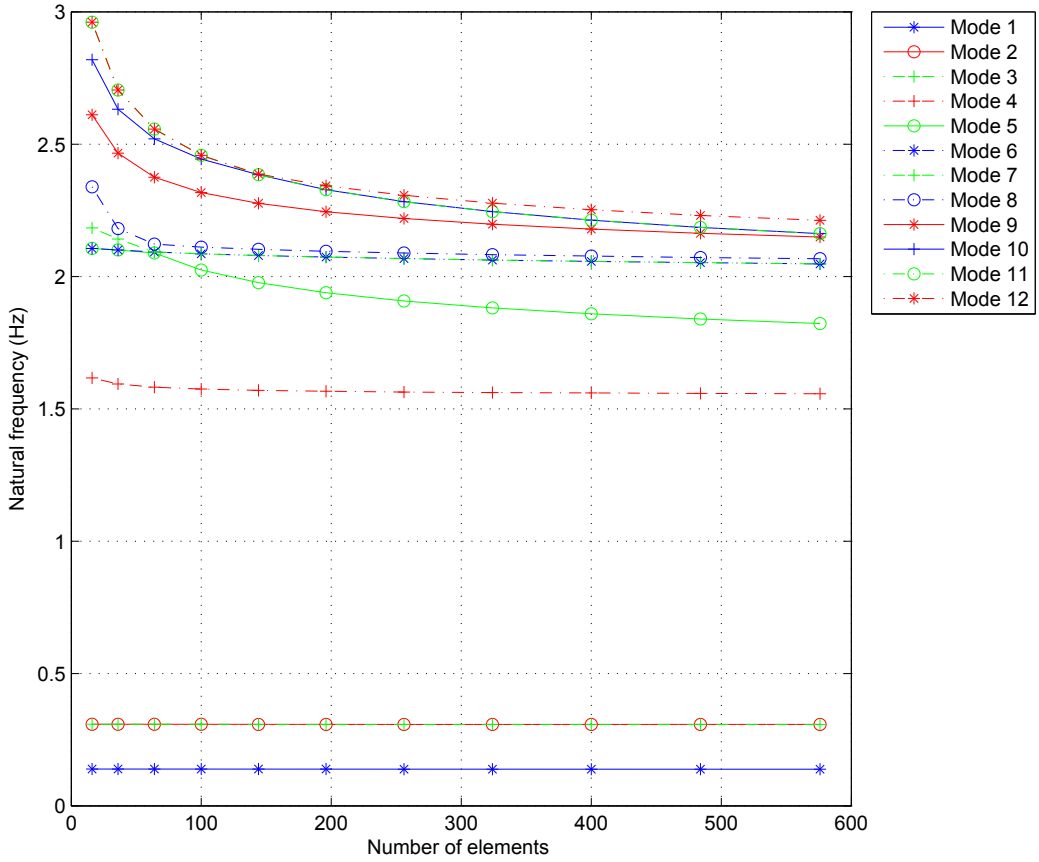

Figure 6.11. Mesh convergence for the membrane of the 1-4 system

The mesh convergence results for tendons are shown in Figure 6.12. The membrane is modeled using 400 elements and each bar is modeled using one beam element. The number of elements for tendons is changed to examine the influence of tendon mesh density on the whole system. It can be seen that the natural frequencies of the first 12 modes are identical as the element number of each tendon increases. This observation indicates that the dynamics of the whole system is not sensitive to the mesh density of tendons.

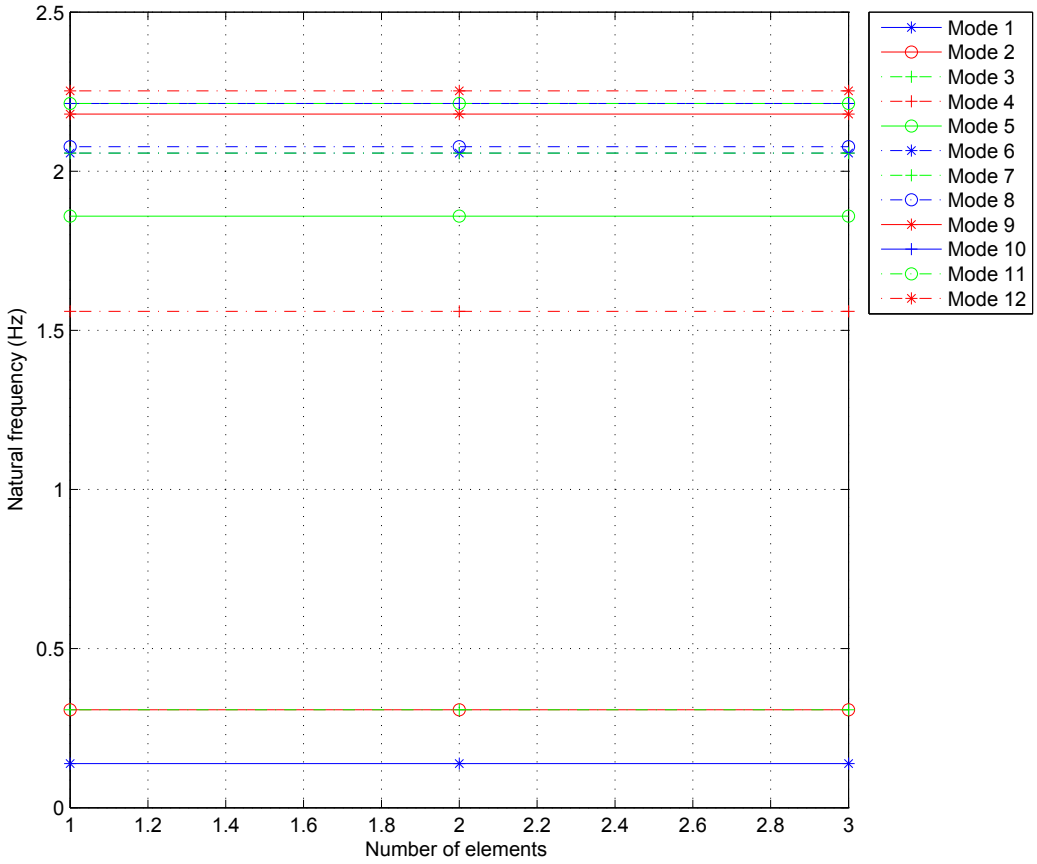

Figure 6.12. Mesh convergence for the tendons of the 1-4 system

6.3.2. 2-3 Symmetric System

To conduct the mesh convergence analysis for the membrane, each bar is modeled by one four-node beam element, and each tendon is modeled using one two-node truss element. The mesh convergence results for the membrane are shown in Figure 6.13, where the frequencies of the first 12 modes are presented. It can be seen that, when the number of elements is greater than 300, the natural frequencies of most modes converge. The frequencies of Mode 11 and Mode 12 are still trying to converge when the number of

elements is greater than 300, while the improvement in natural frequency values is not significant. Thus, it is reasonable to model the membrane with 300 elements.

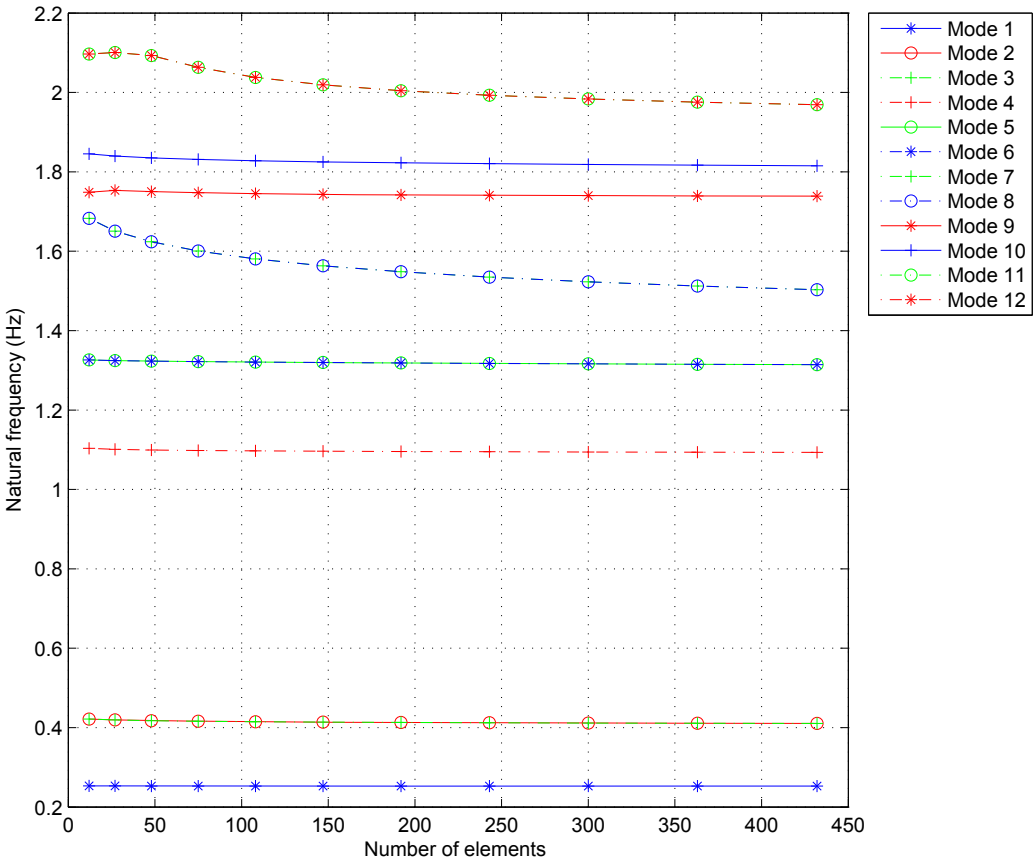

Figure 6.13. Mesh convergence for the membrane of the 2-3 system

The mesh convergence results for tendons are shown in Figure 6.14. The membrane is modeled using 300 elements and one beam element is used for each bar. Similar to the 1-4 system, the natural frequencies of the first 12 modes are identical as the element number of each tendon increases. Thus, we can conclude that the mesh density of tendons has little effect on the dynamics of the whole system.

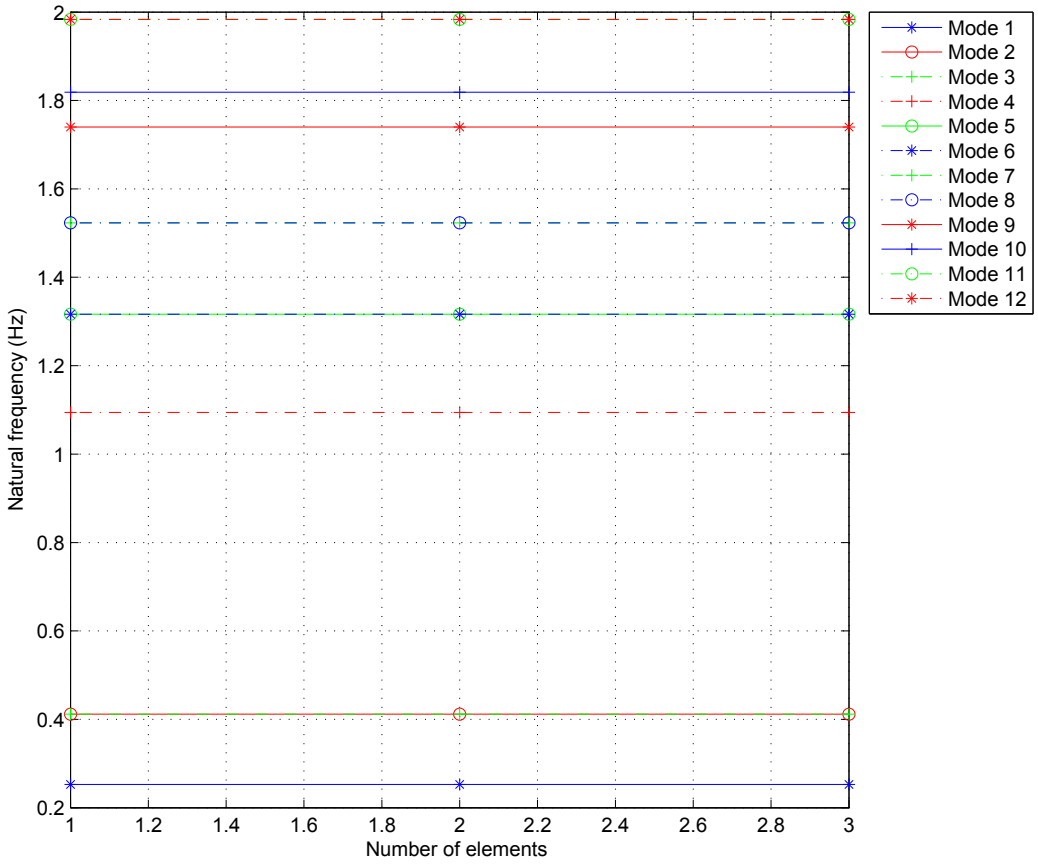

Figure 6.14. Mesh convergence for the tendons of the 2-3 system

6.4. Modal Analysis

In this section, modal analysis for the 1-4 system and the 2-3 system is performed using the three mathematical models developed in this work. To examine the accuracy and reliability of the two simplified models, i.e. the membrane-truss-cable model and the control-oriented model, the natural frequencies given by these two models are compared with the frequencies given by the shell-beam-cable model.

For the nonlinear finite element models, the modal analysis is conducted using Eq. (5.32). For the control-oriented model, the nonlinear equations of motion in Eq. (5.27) are

linearized at the designed equilibrium. The linearized equations can be expressed in the first-order form as:

$$\dot{\boldsymbol{x}}_z = \boldsymbol{A}\boldsymbol{x}_z \tag{5.33}$$

where $\boldsymbol{x}_z$ is the state vector: $\boldsymbol{x}_z = \begin{bmatrix} \boldsymbol{z}^T & \dot{\boldsymbol{z}}^T \end{bmatrix}^T$. Note that the state variables in Eq. (5.33) represent small perturbations and should not be confused with the variables with the same symbols in the nonlinear equations of motion in Eq. (5.27). The eigenvalues of matrix $\boldsymbol{A}$ correspond to the natural frequencies of tensegrity-membrane systems.

6.4.1. 1-4 Symmetric System

Based on the mesh convergence analysis in the previous section, a 20×20 mesh is used for the membrane. In other words, the membrane is discretized into 400 elements. For the two nonlinear finite element models, each bar is modeled by one four-node beam element and three truss elements are used for each tendon. For the control-oriented model, the first five modes are used to model the membrane vibrations.

The natural frequencies are shown in Table 6.6. It can be seen that the results given by the three models are close to each other. The relative errors with respect to the results given by the shell-beam-cable model are less than 3%. Note that the membrane transverse bending stiffness and transverse shear stiffness are ignored in the membrane-truss-cable model and the control-oriented model. The tendon dynamics and the geometric nonlinearity of the membrane are also neglected in the control-oriented model. Based on this observation, we can conclude that, for this 1-4 system, these modeling assumptions for the membrane-truss-cable model and the control-oriented model do not introduce significant modeling errors.

Table 6.6. Natural frequencies of the 1-4 system

	Shell-beam-cable model	Membrane-truss-cable model	Control-oriented model
Mode 1	0.1386 Hz	0.1386 Hz	0.1367 Hz
Mode 2	0.3076 Hz	0.3076 Hz	0.2997 Hz
Mode 3	0.3076 Hz	0.3076 Hz	0.2997 Hz
Mode 4	1.5598 Hz	1.5599 Hz	1.5401 Hz
Mode 5	1.8590 Hz	1.8679 Hz	1.8552 Hz
Mode 6	2.0571 Hz	2.0569 Hz	2.0288 Hz
Mode 7	2.0571 Hz	2.0569 Hz	2.0289 Hz
Mode 8	2.0770 Hz	2.0763 Hz	2.0471 Hz
Mode 9	2.1793 Hz	2.1803 Hz	2.1507 Hz
Mode 10	2.2130 Hz	2.2277 Hz	2.2062 Hz
Mode 11	2.2130 Hz	2.2277 Hz	2.2119 Hz
Mode 12	2.2523 Hz	2.2653 Hz	2.2479 Hz

Mode shapes of the 1-4 system given by the shell-beam-cable model are shown in Figure 6.15 – Figure 6.17. In Figure 6.15, the mode shapes of Mode 1 – Mode 3 show significant coupling between the rigid body motion of the bars and the membrane. The corresponding mode shapes of the membrane in the O_f-$x_f y_f z_f$ frame are depicted in Figure 6.16. It can be seen that, in Mode 1 – Mode 3, the modes of membrane transverse vibrations are also excited. The coupling between membrane deformations and the rigid body motion of bars can be also seen in Mode 5. These observations clearly indicate that the system components of this 1-4 system are highly coupled.

It should be noted that the tendon dynamics is included in the shell-beam-cable model, but tendon deformations do not appear in the first 12 mode shapes of the 1-4 system. This result is expected, since tendons are generally much lighter than bars and membranes,

while they are usually heavily tensioned. As a result, tendon vibrations are of much smaller amplitudes and less likely to be excited compared with vibrations of bars and membranes.

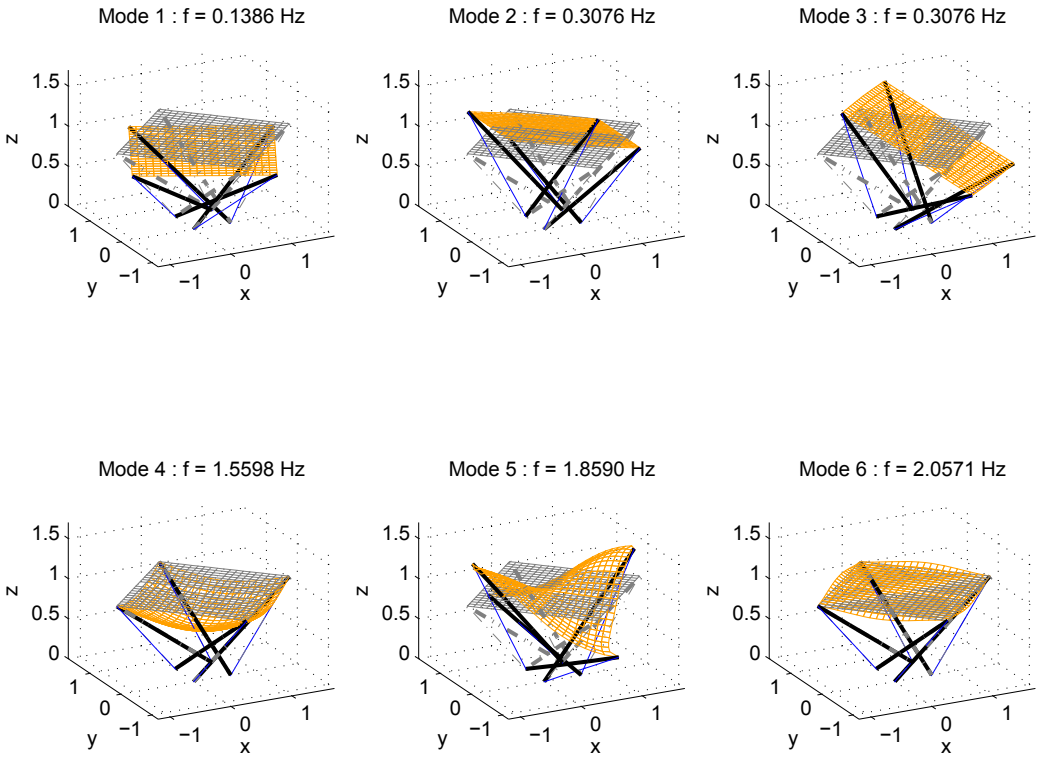

Figure 6.15. Mode shapes of the 1-4 system (Mode 1 – Mode 6)

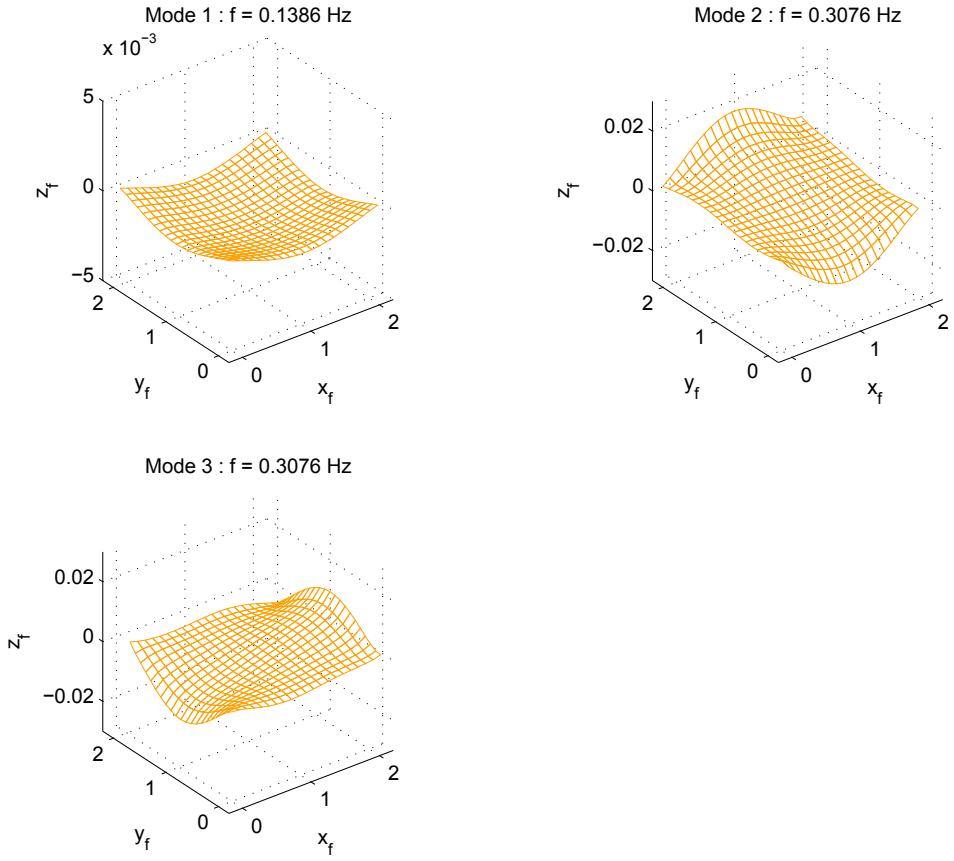

Figure 6.16. Mode shapes of the membrane in the O_f-$x_f y_f z_f$ frame (Mode 1 – Mode 3)

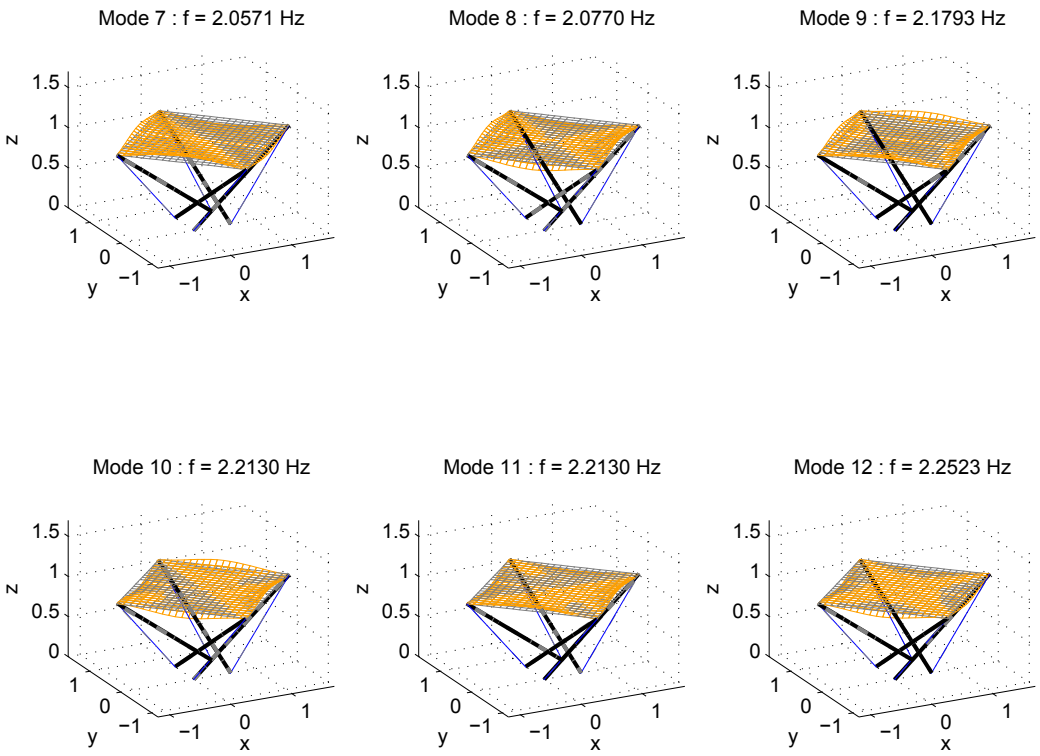

Figure 6.17. Mode shapes of the 1-4 system (Mode 7 – Mode 12)

6.4.2. 2-3 Symmetric System

For the 2-3 system, the triangular membrane is divided into 3 quadrilaterals and a 10×10 mesh is used for each quadrilateral. In other words, 300 elements are used for the membrane. For the two nonlinear finite element models, each bar is modeled by one beam element and three truss elements are used for each tendon. For the control-oriented model, the first four modes are used to model the membrane vibrations.

Natural frequencies of the 2-3 system given by the three models are shown in Table 6.7. Good agreement of the natural frequencies can be observed. The relative errors are less than 1%. Thus, similar to the 1-4 system, we can conclude that the modeling

assumptions for the membrane-truss-cable model and the control-oriented model do not introduce significant modeling errors for this 2-3 system.

Table 6.7. Natural frequencies of the 2-3 system

	Shell-beam-cable model	Membrane-truss-cable model	Control-oriented model
Mode 1	0.2527 Hz	0.2527 Hz	0.2503 Hz
Mode 2	0.4116 Hz	0.4116 Hz	0.4076 Hz
Mode 3	0.4116 Hz	0.4116 Hz	0.4076 Hz
Mode 4	1.0942 Hz	1.0953 Hz	1.0843 Hz
Mode 5	1.3164 Hz	1.3174 Hz	1.3020 Hz
Mode 6	1.3164 Hz	1.3174 Hz	1.3020 Hz
Mode 7	1.5230 Hz	1.5264 Hz	1.5110 Hz
Mode 8	1.5230 Hz	1.5264 Hz	1.5121 Hz
Mode 9	1.7399 Hz	1.7404 Hz	1.7258 Hz
Mode 10	1.8186 Hz	1.8224 Hz	1.8053 Hz
Mode 11	1.9834 Hz	1.9876 Hz	1.9712 Hz
Mode 12	1.9834 Hz	1.9876 Hz	1.9720 Hz

Mode shapes of the 2-3 system given by the shell-beam-cable model are depicted in Figure 6.18 – Figure 6.20. Results in Figure 6.18 and Figure 6.19 show that the membrane rigid body motions, the membrane deformations, and the bar rigid body motions are highly coupled in the first six modes of this 2-3 system. The coupling between system components of this 2-3 system is more significant than that of the 1-4 system, which is expected due to the increased complexity of this 2-3 system. Clearly, for this 2-3 system, it is not reasonable to design or analyze system components separately.

Similar to the 1-4 system, the modes of tendon deformations do not show in the first 12 mode shapes of the 2-3 system. This observation indicates that the dynamics of bars and membranes is dominant for this 2-3 tensegrity-membrane system, and tendon dynamics can be ignored without introducing significant modeling errors.

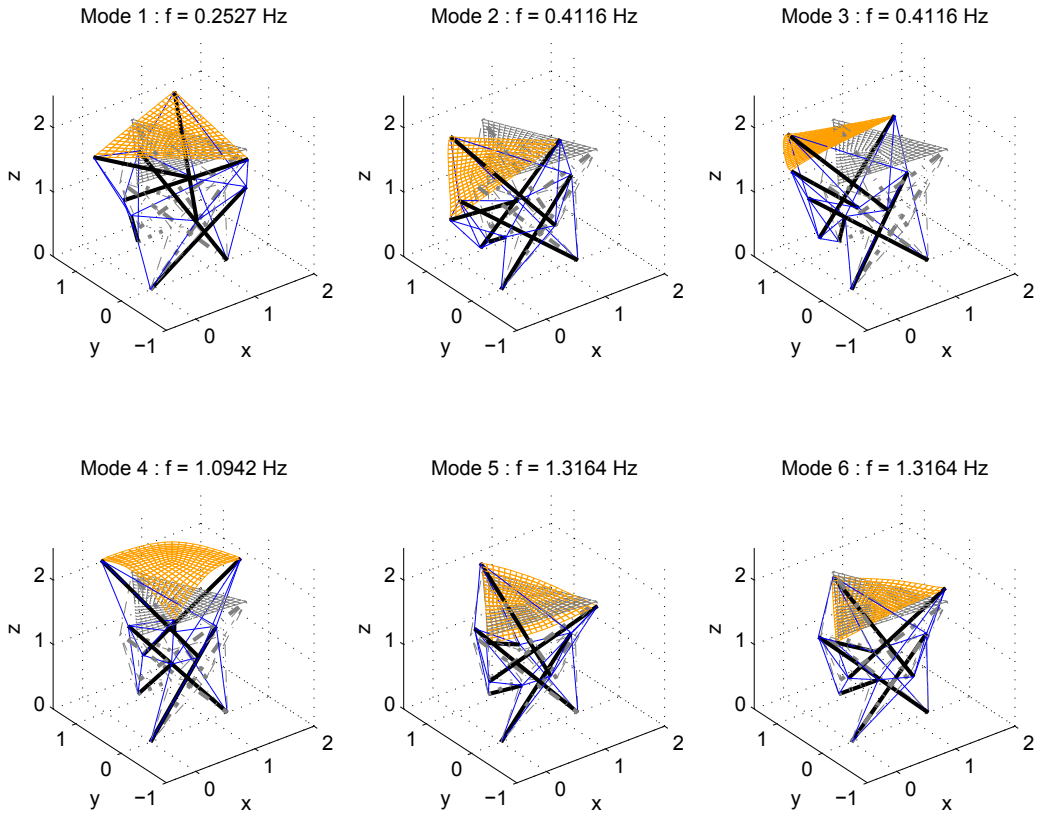

Figure 6.18. Mode shapes of the 2-3 system (Mode 1 – Mode 6)

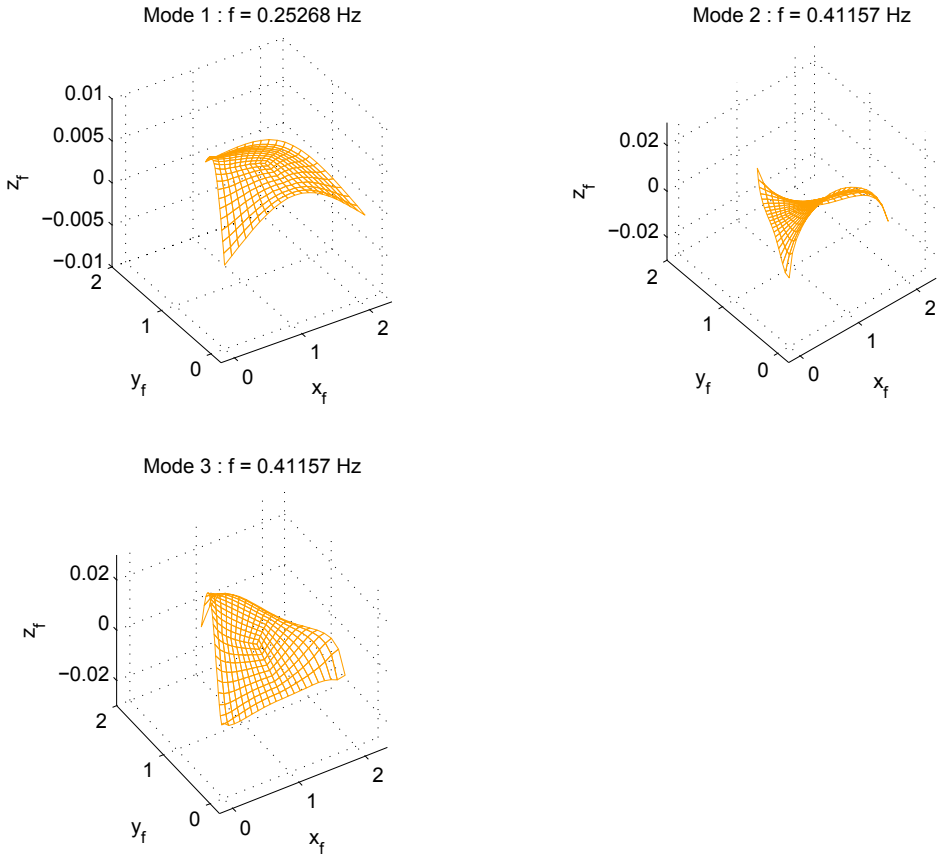

Figure 6.19. Mode shapes of the membrane in the O_f-$x_f y_f z_f$ frame (Mode 1 – Mode 3)

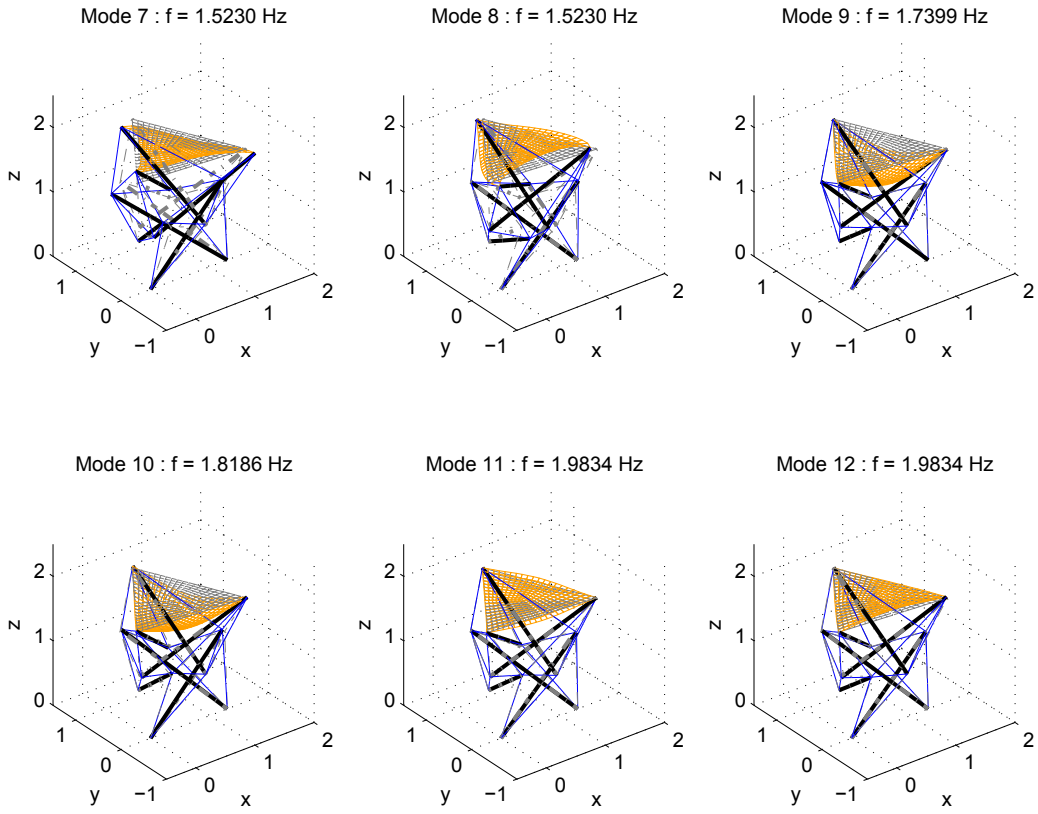

Figure 6.20. Mode shapes of the 2-3 system (Mode 7 – Mode 12)

6.5. Free Vibration Analysis

In this section, free vibration analysis is carried out to study the responses of tensegrity-membrane systems in the time domain. We can also compare the free vibration results given by the shell-beam-cable model with the results given by the membrane-truss-cable model and the control-oriented model to examine the accuracy and reliability of the two simplified models. For the three models, Park's method [59] is used to solve the nonlinear equations of motions of the three models. If $\boldsymbol{x}$ is the generalized coordinate vector, the velocity and acceleration terms can be expressed as:

$$\ddot{\boldsymbol{x}}_{t+\Delta t} = \frac{1}{6\Delta t}\left(10\dot{\boldsymbol{x}}_{t+\Delta t} - 15\dot{\boldsymbol{x}}_t + 6\dot{\boldsymbol{x}}_{t-\Delta t} - \dot{\boldsymbol{x}}_{t-2\Delta t}\right)$$
$$\dot{\boldsymbol{x}}_{t+\Delta t} = \frac{1}{6\Delta t}\left(10\boldsymbol{x}_{t+\Delta t} - 15\boldsymbol{x}_t + 6\boldsymbol{x}_{t-\Delta t} - \boldsymbol{x}_{t-2\Delta t}\right) \tag{5.34}$$

Since Park's method is a 3-step method, initialization is required. The trapezoidal rule is used for the initialization process:

$$\boldsymbol{x}_{t+\Delta t} = \boldsymbol{x}_t + \frac{\Delta t}{2}\left(\dot{\boldsymbol{x}}_t + \dot{\boldsymbol{x}}_{t+\Delta t}\right); \quad \dot{\boldsymbol{x}}_{t+\Delta t} = \dot{\boldsymbol{x}}_t + \frac{\Delta t}{2}\left(\ddot{\boldsymbol{x}}_t + \ddot{\boldsymbol{x}}_{t+\Delta t}\right) \tag{5.35}$$

6.5.1. 1-4 Symmetric System

For the 1-4 symmetric system, a 20×20 mesh is used for the square membrane. Each bar is modeled by one beam element and three truss elements are used for each tendon. The time step is chosen as Δt = 0.01s and the initial perturbation is chosen as $\Delta\dot{\theta}_{12}(t) = 0.01$ rad/s. This time step is chosen according to Shannon's sampling theorem [72] and the highest natural frequency given by the control-oriented model, which is 2.4322 Hz. The sampling frequency is selected to be approximately 40 times higher than 2.4322 Hz, which gives the corresponding time step Δt = 0.01s. In order to perform fair comparison, the same time step is used to solve the three models.

Membrane vibrations are studied by monitoring the transverse deflections of three points on the membrane, which are labeled w_1, w_2, and w_3. These transverse deflections are measured in the O_f-$x_f y_f z_f$ frame and are characterized as:

$$\begin{aligned} w_1 &= w\left(x_f, y_f\right)\Big|_{x_f=0.6(\mathrm{m}),\ y_f=1.6(\mathrm{m})} \\ w_2 &= w\left(x_f, y_f\right)\Big|_{x_f=0.5(\mathrm{m}),\ y_f=0.4(\mathrm{m})} \\ w_3 &= w\left(x_f, y_f\right)\Big|_{x_f=1.5(\mathrm{m}),\ y_f=0.3(\mathrm{m})} \end{aligned} \tag{5.36}$$

Simulation results given by the three models are plotted in Figure 6.21 - Figure 6.23. The responses of the bars given by the three models are in good agreement. Note that the dynamics of tendons and the deformations of bars are ignored in the control-oriented model. Thus, this observation indicates that ignoring the flexibility of bars and tendon dynamics does not cause modeling errors. It can be also observed that the responses of membrane transverse deflections given by the control-oriented model are close to the responses given by the two nonlinear finite element models. Clearly, the geometric nonlinearity of the membrane, which is ignored in the control-oriented model, is not significant when this 1-4 system experiences the given small perturbation.

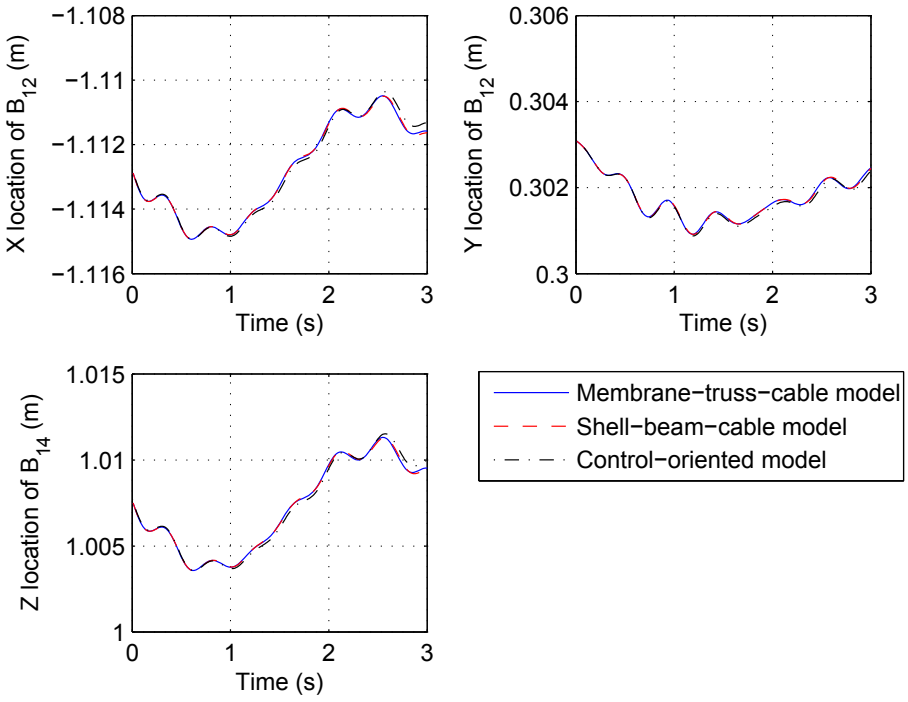

Figure 6.21. Comparison results of the locations of B_{12}

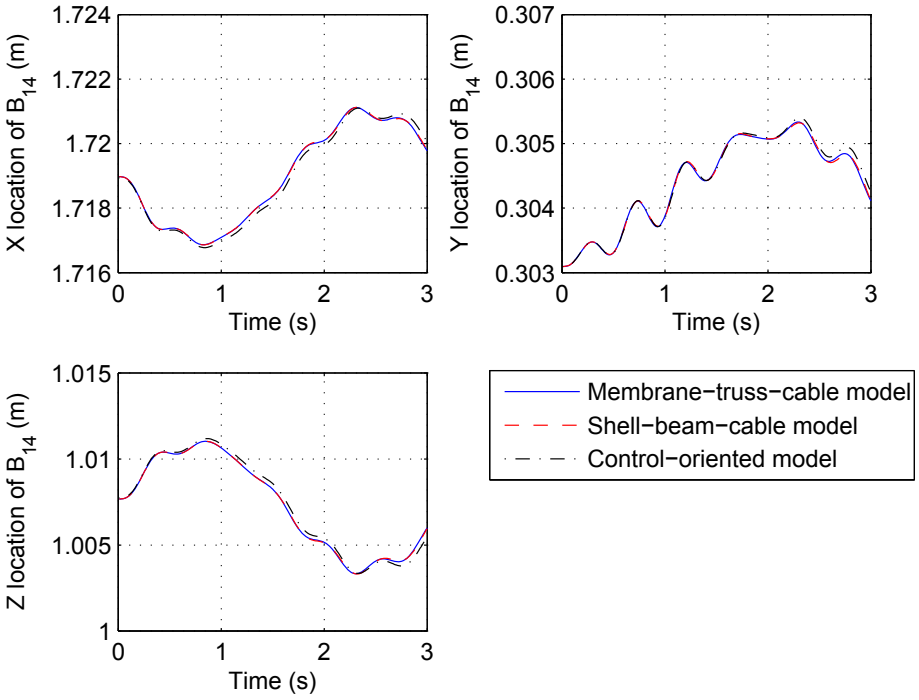

Figure 6.22. Comparison results of the locations of B_{14}

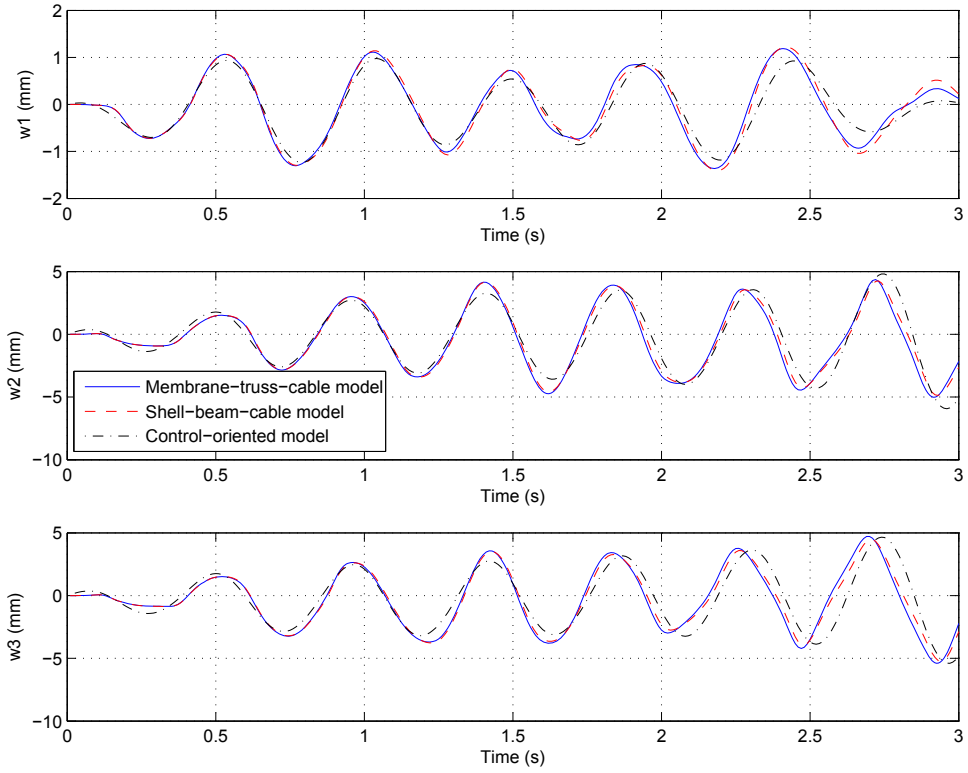

Figure 6.23. Comparison results of w_1, w_2, and w_3 of the 2-3 system

To examine the transverse vibrations of tendons, we first introduce a local orthogonal coordinate system with basis vectors $\vec{e}_{t1}$, $\vec{e}_{t2}$, and $\vec{e}_{t3}$ for each tendon. The vector $\vec{e}_{t1}$ is defined to be the unit vector pointing from one tendon end to another. Then, $\vec{e}_{t2}$ and $\vec{e}_{t3}$, which define the two transverse directions of a tendon, can be expressed as:

$$\vec{e}_{t2} = \frac{\vec{e}_{t1} \times \vec{e}_z}{\left\| \vec{e}_{t1} \times \vec{e}_z \right\|}; \quad \vec{e}_{t3} = \vec{e}_{t1} \times \vec{e}_{t2} \tag{5.37}$$

The tendon transverse deflections of the maximum amplitude are shown in Figure 6.24. It can be seen that the results given by the two nonlinear finite element models are very close. Note that the vibration amplitude is less than 5×10^{-4} mm, which is much smaller than the vibration amplitude of the attached membrane and the bars. This

observation coincides with the modal analysis result that modes of tendon vibrations are not excited in the first 12 modes of the 1-4 tensegrity-membrane system. Therefore, it is reasonable to conclude that for this 1-4 system the tendon dynamics does not affect the dynamics of the whole system.

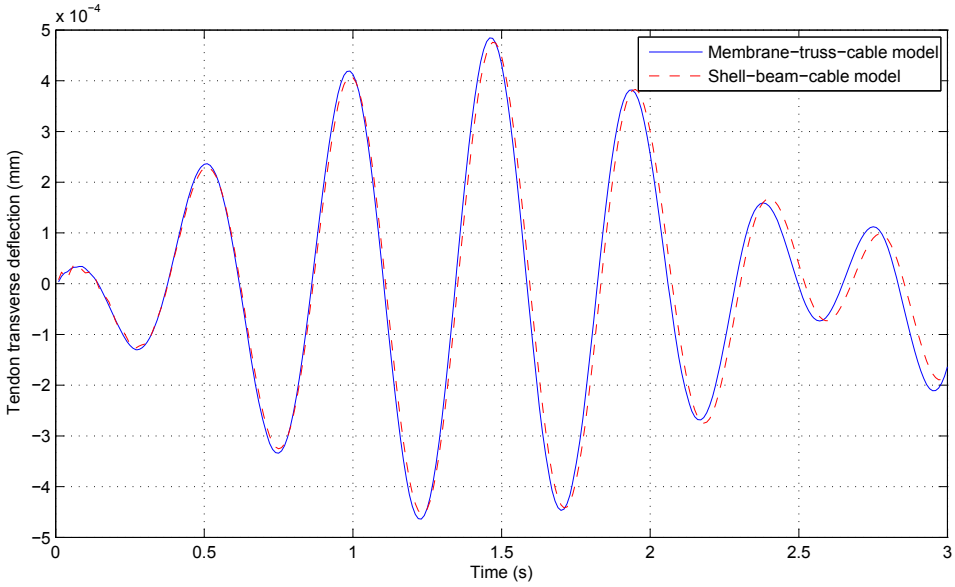

Figure 6.24. Representative tendon transverse deflections of the 1-4 system

6.5.2. 2-3 Symmetric System

For the 2-3 system, the triangular membrane is divided into 3 quadrilaterals and a 10×10 mesh is used for each quadrilateral. Each bar is modeled by one beam element and three truss elements are used for each tendon. The time step is chosen as Δt = 0.01s and the initial disturbance $\Delta\dot{\theta}_{11}(t) = 0.01$ rad/s is applied. This time step is chosen to make the sampling frequency approximately 10 times higher than the highest natural frequency given by the control-oriented model, which is 4.4607 Hz. The same time step is used to solve the three mathematical models in order to conduct fair comparison.

To study the membrane vibrations of this 2-3 system, the transverse deflections of 3 points on the membrane, w_1, w_2, and w_3, are monitored. These transverse deflections are characterized as:

$$\begin{aligned} w_1 &= w\left(x_f, y_f\right)\Big|_{x_f=0.86(\mathrm{m}),\ \ y_f=0.50(\mathrm{m})} \\ w_2 &= w\left(x_f, y_f\right)\Big|_{x_f=0.86(\mathrm{m}),\ \ y_f=0.98(\mathrm{m})} \\ w_3 &= w\left(x_f, y_f\right)\Big|_{x_f=0.45(\mathrm{m}),\ \ y_f=0.26(\mathrm{m})} \end{aligned} \tag{5.38}$$

Simulation results given by the three models are presented in Figure 6.25 - Figure 6.28. Similar to the observations for the 1-4 system, it can be seen that the responses of bars given by the three models are close to each other. Therefore, for this 2-3 system, it is reasonable to treat bars as rigid bodies when the system is under the given small perturbation. Moreover, membrane transverse deflections given by the three models are in good agreement, indicating that ignoring the geometric nonlinearities of the membrane does not cause major errors.

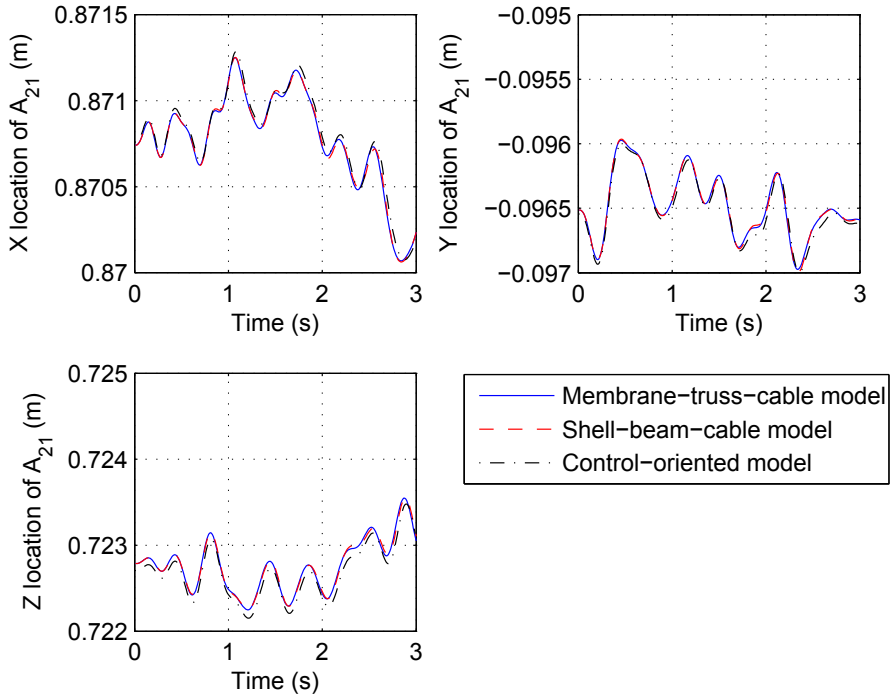

Figure 6.25. Comparison results of the locations of A_{21}

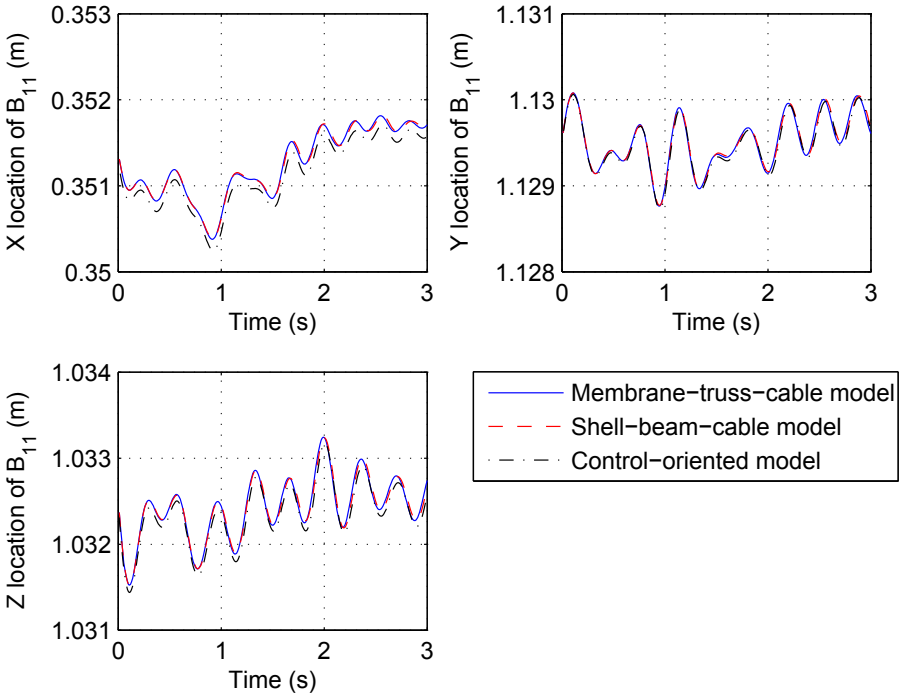

Figure 6.26. Comparison results of the locations of B_{11}

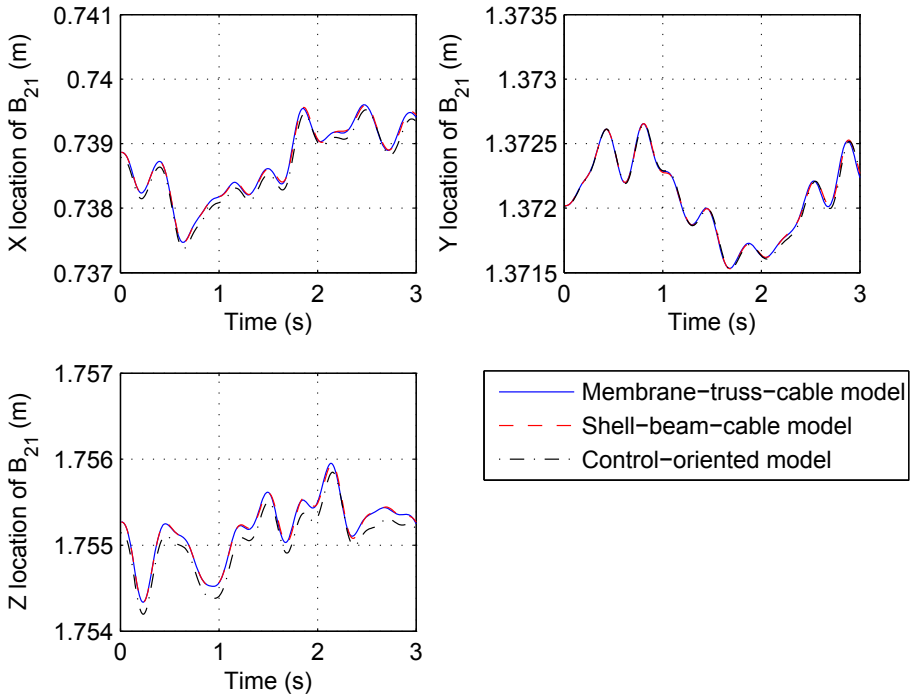

Figure 6.27. Comparison results of the locations of B_{21}

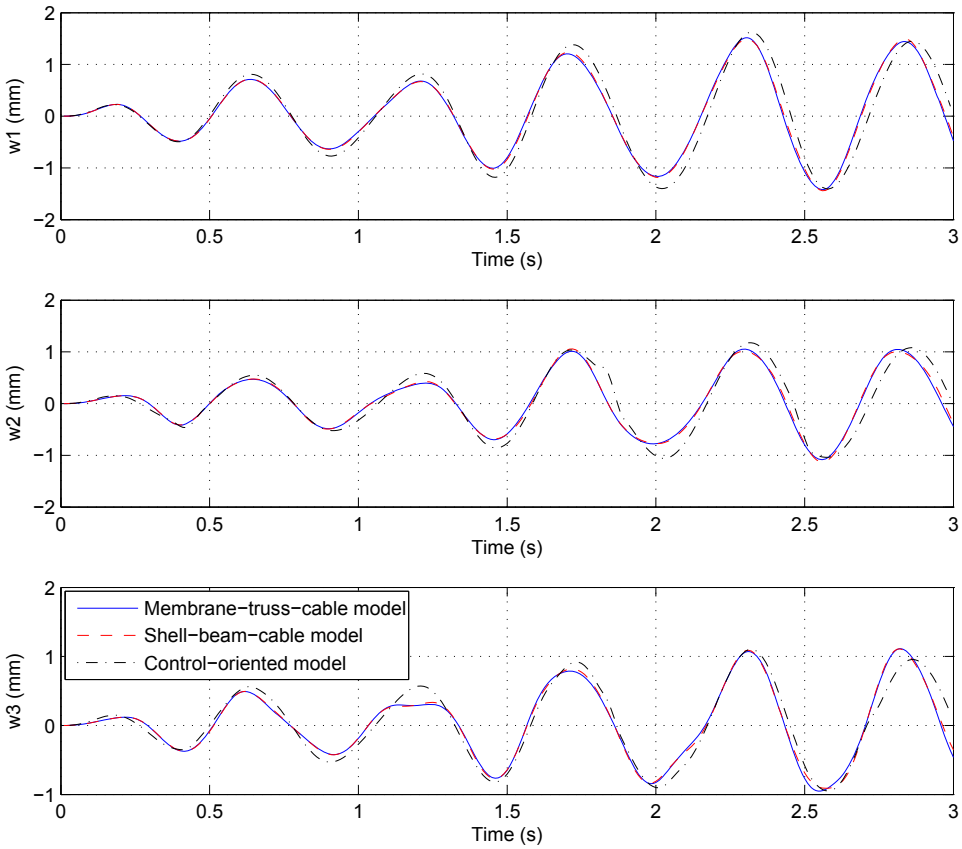

Figure 6.28. Comparison results of w_1, w_2, and w_3 of the 2-3 system

The tendon transverse responses of the maximum amplitude given by the shell-beam-cable model and the membrane-truss-cable model are shown in Figure 6.29. Clearly, the results given by the two nonlinear finite element models are close to each other. The vibration amplitude is less than 1.5×10^{-3} mm, which is much smaller than the vibration amplitude of the attached membrane and the bars. Thus, we can conclude that it is reasonable to ignore the tendon dynamics for this 2-3 system.

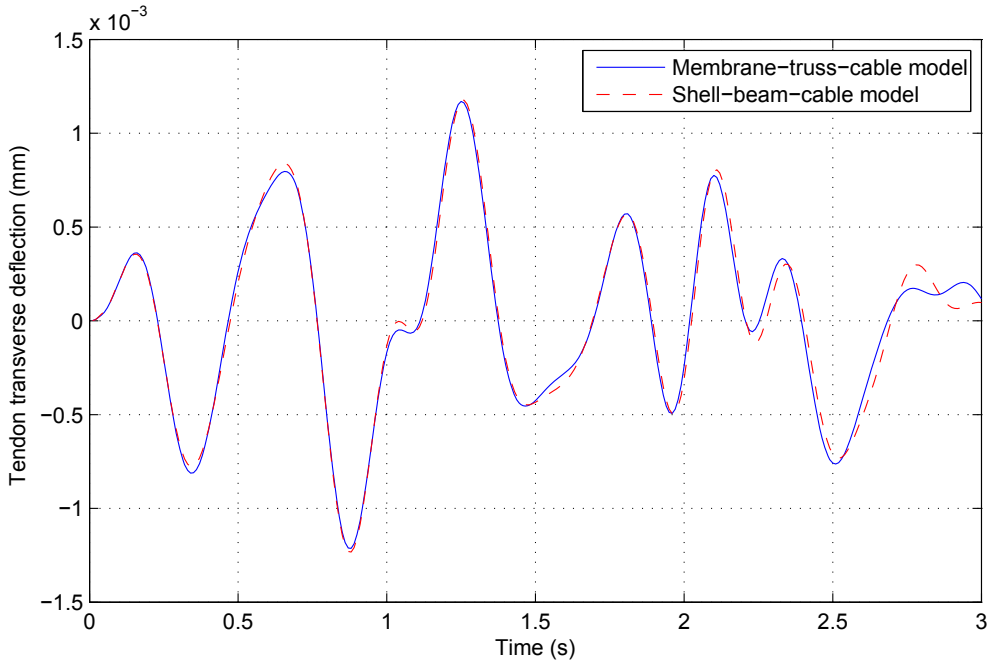

Figure 6.29. Representative tendon transverse deflections of the 2-3 system

6.6. Conclusions

In this chapter, static analysis for a 1-4 symmetric system and a 2-3 symmetric system is first performed using the shell-beam-cable model. Simulation results show that the two tensegrity-membrane systems converge to the designed equilibrium configurations, indicating that the equilibrium finding method introduced in Chapter 3 is correct.

Yield and buckling analysis is conducted for the membranes, tendons, and bars at the designed equilibriums. For the membranes, the maximum principal stress criterion and the von Mises criterion are used. The buckling analysis for bars is based on Euler's column formula. Tendon stresses are compared with the yield stress of the corresponding material. Analysis results show that the designed equilibrium conditions are feasible and no mechanical failure occurs due to prestressing.

According to the modal analysis results, the natural frequencies given by the three models are very close. Mode shapes of the two tensegrity-membrane systems indicate that there is strong coupling between the membrane rigid body motions, the membrane deformations, and the rigid body motions of bars. Thus, we can conclude that a tensegrity-membrane system should be designed and studied as a whole system and it is not reasonable to design or analyze each component separately.

Moreover, the modal analysis results show that the modes of tendon transverse vibrations are not excited in the first 12 modes of the 1-4 system and the 2-3 system. In the free vibration analysis, the tendon transverse deflection of the maximum amplitude is much smaller than the vibration amplitudes of membranes and bars. These two observations are expected, since tendons are generally much lighter compared with bars and membranes. Therefore, it is reasonable to ignore the dynamics of tendons in the study of system dynamics, which is a commonly used modeling assumption in the modeling and analysis of tensegrity systems.

The free vibration results given by the three models are compared with each other. It can be observed that the free vibration responses given by the three models are close to each other. It indicates that the control-oriented model can capture the system dynamics accurately when the system experiences small perturbations. Good agreement of the responses of bars indicates that modeling the bars as rigid bodies does not introduce significant modeling errors. This conclusion corresponds to another commonly used modeling assumption in tensegrity system analysis that bars can be treated as rigid bodies.

Chapter 7: Nonlinear Control Design for System Deployment

7.1. Introduction

System deployment is to change the shape of a system from one configuration to another configuration. Desired deployment trajectories of a tensegrity-membrane system usually cover a large region within the system operational envelope. Therefore, a single linear controller may not be able to complete this control task and nonlinear controllers should be considered.

From the point of view of control design, tensegrity-membrane systems should be classified as nonlinear underactuated systems, since these is no actuator directly regulating the behavior of membranes. Nonlinear control design for underactuated systems is challenging because there are fewer control inputs compared to the number of degrees of freedom of the system. One of the successful nonlinear control methods for underactuated systems is the partial feedback linearization (PFL) technique [60]. This method has been implemented to control an acrobot [61] and a three-link pendulum [62]. De Luca et al. [63] developed a stabilizing controller based on the PFL technique and the nilpotent approximation for an underactuated planar 2R manipulator. Tuan et al. [64] presented and tested a control algorithm, developed by combining the PFL technique with the sliding mode control, for a 3D overhead crane. It should be noted that controllers based on the PFL technique is not robust due to the inherent nonrobustness of feedback linearization and the underactuated dynamics cannot be directly regulated by PFL controllers.

In this chapter, a nonlinear control strategy is design to deploy tensegrity-membrane systems. A nonlinear adaptive controller based on the collocated PFL technique is used to drive tensegrity-membrane systems from initial packaged configurations to final deployed configurations. Around the final deployed configurations, an H_∞ controller is employed for system stabilization. This control strategy is used to control and deploy three tensegrity-membrane systems, i.e. a 1-4(D) system, a 1-6(D) system, and a 2-3 system. Simulation results are presented and discussed at the end of this chapter.

7.2. Nonlinear Adaptive Controller for System Deployment

After expressing the equations of motion in Eq. (5.27) in block matrix form, we have

$$\begin{bmatrix} \hat{\boldsymbol{M}}_{11} & \hat{\boldsymbol{M}}_{12} \\ \hat{\boldsymbol{M}}_{12}{}^{T} & \hat{\boldsymbol{M}}_{22} \end{bmatrix} \begin{bmatrix} \ddot{\boldsymbol{q}} \\ \ddot{\boldsymbol{\eta}} \end{bmatrix} + \begin{bmatrix} \hat{\boldsymbol{F}}_1 \\ \hat{\boldsymbol{F}}_2 \end{bmatrix} + \begin{bmatrix} \hat{\boldsymbol{B}}_1 \\ \boldsymbol{O} \end{bmatrix} \boldsymbol{u} = \boldsymbol{O} \tag{5.39}$$

Based on the collocated partial feedback linearization technique, Eq. (5.39) can be simplified as:

$$\begin{aligned} &\ddot{\boldsymbol{q}} + \boldsymbol{F}_q^{\,*} + \boldsymbol{B}_q^{\,*} \boldsymbol{u} = \boldsymbol{O} \\ &\hat{\boldsymbol{M}}_{22} \ddot{\boldsymbol{\eta}} + \hat{\boldsymbol{F}}_2 + \hat{\boldsymbol{M}}_{12}{}^{T} \ddot{\boldsymbol{q}} = \boldsymbol{O} \end{aligned} \tag{5.40}$$

where

$$\begin{aligned} \boldsymbol{F}_q^{\,*} &= \hat{\boldsymbol{M}}_q{}^{-1} \left(\hat{\boldsymbol{F}}_1 - \hat{\boldsymbol{M}}_{12} \hat{\boldsymbol{M}}_{22}{}^{-1} \hat{\boldsymbol{F}}_2 \right) \\ \boldsymbol{B}_q^{\,*} &= \hat{\boldsymbol{M}}_q{}^{-1} \hat{\boldsymbol{B}}_1 \\ \hat{\boldsymbol{M}}_q &= \hat{\boldsymbol{M}}_{11} - \hat{\boldsymbol{M}}_{12} \hat{\boldsymbol{M}}_{22}{}^{-1} \hat{\boldsymbol{M}}_{12}{}^{T} \end{aligned} \tag{5.41}$$

Here the superscript * indicates the exact value of a variable, i.e. symbol v* represents the exact value of v.

Compared to the elastic characteristics of the membrane, the mass properties of the bars and the membrane can be measured accurately. Moreover, the elastic behavior of

modern elastomers is linear even for large strains, so their stiffness properties can be measured accurately compared to the membrane elastic characteristics. Therefore, it is reasonable to assume that $\boldsymbol{B}_q^*$ is exactly known, while $\boldsymbol{F}_q^*$ contains modeling errors and parameter uncertainties, i.e.

$$\boldsymbol{F}_q^* = \boldsymbol{F}_q + \Delta\boldsymbol{F}_q; \quad \boldsymbol{B}_q^* = \boldsymbol{B}_q \tag{5.42}$$

where $\boldsymbol{F}_q$ and $\boldsymbol{B}_q$ are the nominal models of $\boldsymbol{F}_q^*$ and $\boldsymbol{B}_q^*$, respectively.

The uncertainty $\Delta\boldsymbol{F}_q$ can be approximated by a set of radial basis functions. Then, Eq. (5.40) can be written as:

$$\begin{aligned} &\ddot{\boldsymbol{q}} + \left(\boldsymbol{F}_q + \boldsymbol{W}_F^{*T}\boldsymbol{\Phi}_F + \boldsymbol{\varepsilon}\right) + \boldsymbol{B}_q\boldsymbol{u} = \boldsymbol{O} \\ &\hat{\boldsymbol{M}}_{22}\ddot{\boldsymbol{\eta}} + \hat{\boldsymbol{F}}_2 + \hat{\boldsymbol{M}}_{12}{}^T\ddot{\boldsymbol{q}} = \boldsymbol{O} \end{aligned} \tag{5.43}$$

where $\boldsymbol{W}_F$ is the matrix of unknown constants, $\boldsymbol{\Phi}_F$ is the vector of radial basis functions, and $\boldsymbol{\varepsilon}$ is the approximation error. Here, the Gaussian function is used:

$$\Phi_F{}^i = \exp\left(-\left\|\boldsymbol{v}_q - \boldsymbol{v}_c\right\|_2^2 \Big/ 2\sigma_q{}^2\right); \quad \boldsymbol{v}_q = \begin{bmatrix}\boldsymbol{q}^T & \dot{\boldsymbol{q}}^T\end{bmatrix}^T \tag{5.44}$$

where $\boldsymbol{v}_c$ denotes the vector of centers and σ_q denotes the width of the Gaussian function. Barron [65] has proven that, for a scalar function, when m Gaussian functions are used, the approximation error ε satisfies the following equation:

$$\left|\varepsilon\right| < \varepsilon^*; \quad \varepsilon^* \simeq O(1/\sqrt{m}) \tag{5.45}$$

Based on the collocated PFL technique, the control input is chosen as:

$$\boldsymbol{u} = \boldsymbol{B}_q{}^{-1}\left(-\boldsymbol{F}_q - \boldsymbol{W}_F{}^T\boldsymbol{\Phi}_F - \ddot{\boldsymbol{q}}_d + \boldsymbol{D}_q\left(\dot{\boldsymbol{q}} - \dot{\boldsymbol{q}}_d\right) + \boldsymbol{K}_q\left(\boldsymbol{q} - \boldsymbol{q}_d\right)\right) \tag{5.46}$$

where $\boldsymbol{D}_q$ and $\boldsymbol{K}_q$ are chosen as:

$$\begin{aligned} &\boldsymbol{D}_q = d_q(t)\boldsymbol{I}; \quad \boldsymbol{K}_q = k_q(t)\boldsymbol{I} \\ &\left(0 < \underline{d} \le d_q(t) \le \overline{d}; \quad 0 < \underline{k} \le k_q(t) \le \overline{k}\right) \end{aligned} \tag{5.47}$$

Note that here $\boldsymbol{D_q}$ and $\boldsymbol{K_q}$ are time-varying. In Eq. (5.46), $\boldsymbol{q_d}$ is the desired trajectory to be tracked by the closed-loop system, which is a user-defined bounded signal. In this work, $\boldsymbol{q_d}$ is a time-varying function, but its argument, which is time t, is not explicitly written in equations for simplicity.

After inserting Eq. (5.46) into Eq. (5.43), the closed-loop system is:

$$\begin{aligned} &\ddot{\boldsymbol{e}} + \boldsymbol{D_q}\dot{\boldsymbol{e}} + \boldsymbol{K_q}\boldsymbol{e} + \Delta\boldsymbol{W_F}^T\boldsymbol{\Phi_F} + \boldsymbol{\varepsilon} = \boldsymbol{O} \\ &\hat{\boldsymbol{M}}_{22}\ddot{\boldsymbol{\eta}} + \hat{\boldsymbol{F}}_2 + \hat{\boldsymbol{M}}_{12}{}^T\ddot{\boldsymbol{q}} = \boldsymbol{O} \end{aligned} \tag{5.48}$$

where $\boldsymbol{e} = \boldsymbol{q} - \boldsymbol{q_d}$ and $\Delta\boldsymbol{W_F} = \boldsymbol{W_F^*} - \boldsymbol{W_F}$.

Let the candidate Lyapunov function be:

$$\begin{aligned} &V\left(t, \hat{\boldsymbol{x}}\right) = \boldsymbol{e}^T\boldsymbol{P}_1\left(t\right)\boldsymbol{e} + 2\boldsymbol{e}^T\boldsymbol{P}_2\dot{\boldsymbol{e}} + \dot{\boldsymbol{e}}^T\boldsymbol{P}_3\dot{\boldsymbol{e}} + Tr\left(\Gamma^{-1}\Delta\boldsymbol{W_F}^T\Delta\boldsymbol{W_F}\right) \\ &\left(\hat{\boldsymbol{x}} = \left[\boldsymbol{e}^T \quad \dot{\boldsymbol{e}}^T \quad vec\left(\Delta\boldsymbol{W_F}\right)^T\right]^T; \quad \underline{\Gamma} \prec \Gamma^{-1} \prec \overline{\Gamma}\right) \end{aligned} \tag{5.49}$$

where $vec(\boldsymbol{V})$ is the vectorization of matrix $\boldsymbol{V}$. In other words, if matrix $\boldsymbol{V}$ is expressed as $\boldsymbol{V} = \left[\boldsymbol{v_1} \quad ... \quad \boldsymbol{v_n}\right]$, then $vec(\boldsymbol{V})$ can be written as $vec\left(\boldsymbol{V}\right) = \left[\boldsymbol{v_1}^T \quad ... \quad \boldsymbol{v_n}^T\right]^T$. In Eq. (5.49), $\boldsymbol{P}_1(t)$, $\boldsymbol{P}_2$, and $\boldsymbol{P}_3$ are chosen as:

$$\begin{aligned} &\boldsymbol{P}_1\left(t\right) = \alpha\boldsymbol{D_q} + \beta\boldsymbol{K_q} = \left(\alpha d_q\left(t\right) + \beta k_q\left(t\right)\right)\boldsymbol{I} \\ &\boldsymbol{P}_2 = \alpha\boldsymbol{I}; \quad \boldsymbol{P}_3 = \beta\boldsymbol{I}; \quad \left(\alpha > 0; \quad \beta > 0\right) \end{aligned} \tag{5.50}$$

The dynamics of $\boldsymbol{W_F}$ is chosen as:

$$\dot{\boldsymbol{W}}_{\boldsymbol{F}} = \mathbf{Proj}\left(\boldsymbol{W_F}, \boldsymbol{Y}\right); \quad \boldsymbol{Y} = -\Gamma\boldsymbol{\Phi_F}\left(\boldsymbol{e}^T\boldsymbol{P}_2 + \dot{\boldsymbol{e}}^T\boldsymbol{P}_3\right) \tag{5.51}$$

where $\mathbf{Proj}(\cdot,\cdot)$ is the projection operator to prevent parameter drift [66]. The projection operator guarantees that $\boldsymbol{W_F}$ is bounded, i.e. $Tr\left(\Delta\boldsymbol{W_F}^T\left(\boldsymbol{Y} - \mathbf{Proj}\left(\boldsymbol{W_F}, \boldsymbol{Y}\right)\right)\right) \le 0$ and $\left\|\boldsymbol{W_F}\right\| \le \overline{W}_F$. Note that the generalized projection operator for matrices is used in Eq.

(5.51). In other words, for matrices $\boldsymbol{V} = \begin{bmatrix} \boldsymbol{v}_1 & \dots & \boldsymbol{v}_n \end{bmatrix}$ and $\boldsymbol{F} = \begin{bmatrix} \boldsymbol{f}_1 & \dots & \boldsymbol{f}_n \end{bmatrix}$, **Proj**($\boldsymbol{V}$, $\boldsymbol{F}$) can be expressed as:

$$\mathbf{Proj}(\boldsymbol{V}, \boldsymbol{F}) = \begin{bmatrix} \mathbf{Proj}(\boldsymbol{v}_1, \boldsymbol{f}_1) & \dots & \mathbf{Proj}(\boldsymbol{v}_n, \boldsymbol{f}_n) \end{bmatrix} \tag{5.52}$$

where $\mathbf{Proj}(\boldsymbol{v}_i, \boldsymbol{f}_i)$ is the projection operator for vectors.

After taking the time derivative of Eq. (5.49) and inserting Eq. (5.51), we get:

$$\begin{aligned} \dot{V} &\le -2\dot{\boldsymbol{e}}^T \left(\boldsymbol{P}_3 \boldsymbol{D}_q - \boldsymbol{P}_2 \right) \dot{\boldsymbol{e}} - \boldsymbol{e}^T \left(2\boldsymbol{P}_2 \boldsymbol{K}_q - \dot{\boldsymbol{P}}_1 \right) \boldsymbol{e} - 2\left(\boldsymbol{e}^T \boldsymbol{P}_2 + \dot{\boldsymbol{e}}^T \boldsymbol{P}_3 \right) \boldsymbol{\varepsilon} \\ &\le -\boldsymbol{x}_e{}^T \boldsymbol{Q} \boldsymbol{x}_e - \boldsymbol{x}_e{}^T \boldsymbol{H} \boldsymbol{\varepsilon} \end{aligned} \tag{5.53}$$

where

$$\boldsymbol{x}_e = \begin{bmatrix} \boldsymbol{e}^T & \dot{\boldsymbol{e}}^T \end{bmatrix}^T ; \ \boldsymbol{Q} = \begin{bmatrix} \left(\alpha(2k_q - \dot{d}_q) - \beta \dot{k}_q \right) \boldsymbol{I} & \boldsymbol{O} \\ \boldsymbol{O} & 2\left(\beta d_q - \alpha \right) \boldsymbol{I} \end{bmatrix}$$
$$\boldsymbol{H} = 2\begin{bmatrix} \alpha \boldsymbol{I} & \beta \boldsymbol{I} \end{bmatrix}^T \tag{5.54}$$

By choosing α, β, d_q, and k_q appropriately, we can make $2(\beta d_q - \alpha)$ and $2\alpha(k_q - \dot{d}_q) - \beta \dot{k}_q$ positive. Also, we can get the following inequality:

$$\boldsymbol{x}_e{}^T \boldsymbol{Q} \boldsymbol{x}_e \ge \lambda_{\min} \left\| \boldsymbol{x}_e \right\|^2 > 0 \tag{5.55}$$

where $\lambda_{\min}$ is a positive constant selected such that

$$\lambda_{\min} = \min_{t>0} \left\{ \alpha(2k_q - \dot{d}_q) - \beta \dot{k}_q, \quad 2\left(\beta d_q - \alpha \right) \right\} \tag{5.56}$$

According to Eq. (5.45), we have $\left\| \boldsymbol{\varepsilon} \right\| < \varepsilon^* \sqrt{n_\varepsilon}$, if $\boldsymbol{\varepsilon}$ is a $n_\varepsilon \times 1$ vector. Then, Eq. (5.53) can be expressed as:

$$\begin{aligned} \dot{V} &= -\boldsymbol{x}_e{}^T \boldsymbol{Q} \boldsymbol{x}_e + \boldsymbol{x}_e{}^T \boldsymbol{H} \left(-\boldsymbol{\varepsilon} \right) \\ &\le -\lambda_{\min} \left\| \boldsymbol{x}_e \right\|^2 + \left\| \boldsymbol{x}_e \right\| \left\| \boldsymbol{H} \right\| n_\varepsilon \varepsilon^* \\ &\le -\left\| \boldsymbol{x}_e \right\| \left(\lambda_{\min} \left\| \boldsymbol{x}_e \right\| - \left\| \boldsymbol{H} \right\| n_\varepsilon \varepsilon^* \right) \end{aligned} \tag{5.57}$$

After combining Eq. (5.46) and Eq. (5.51), the nonlinear adaptive control law is:

$$\begin{aligned} \boldsymbol{u} &= \boldsymbol{B}_q^{-1}\left(-\boldsymbol{F}_q - \boldsymbol{W}_F^{\,T}\boldsymbol{\Phi}_F - \ddot{\boldsymbol{q}}_d + \boldsymbol{D}_q\left(\dot{\boldsymbol{q}} - \dot{\boldsymbol{q}}_d\right) + \boldsymbol{K}_q\left(\boldsymbol{q} - \boldsymbol{q}_d\right)\right) \\ \dot{\boldsymbol{W}}_F &= \mathbf{Proj}\left(\boldsymbol{W}_F, -\Gamma\boldsymbol{\Phi}_F\left(\boldsymbol{e}^T\boldsymbol{P}_2 + \dot{\boldsymbol{e}}^T\boldsymbol{P}_3\right)\right) \end{aligned} \tag{5.58}$$

This Lyapunov stability analysis leads to the following lemma.

Lemma 7.1. Given the open-loop plant in Eq. (5.40), after applying the control law in Eq. (5.58) to the plant, the tracking error of the closed-loop system in Eq. (5.48), i.e. the dynamics of $\boldsymbol{x}_e$, is ultimately bounded.

Proof: According to Eqs. (5.47), (5.49), and (5.50), we get:

$$\lambda_{\min}\left(\boldsymbol{V}_1\right)\left\|\hat{\boldsymbol{x}}\right\|^2 \le V\left(t,\hat{\boldsymbol{x}}\right) \le \lambda_{\max}\left(\boldsymbol{V}_2\right)\left\|\hat{\boldsymbol{x}}\right\|^2 \tag{5.59}$$

where

$$\boldsymbol{V}_1 = \begin{bmatrix} \left(\alpha\underline{d} + \beta\underline{k}\right)\boldsymbol{I} & \alpha\boldsymbol{I} & \boldsymbol{O} \\ \alpha\boldsymbol{I} & \beta\boldsymbol{I} & \boldsymbol{O} \\ \boldsymbol{O} & \boldsymbol{O} & \underline{\Gamma}\boldsymbol{I} \end{bmatrix};\quad \boldsymbol{V}_2 = \begin{bmatrix} \left(\alpha\overline{d} + \beta\overline{k}\right)\boldsymbol{I} & \alpha\boldsymbol{I} & \boldsymbol{O} \\ \alpha\boldsymbol{I} & \beta\boldsymbol{I} & \boldsymbol{O} \\ \boldsymbol{O} & \boldsymbol{O} & \overline{\Gamma}\boldsymbol{I} \end{bmatrix} \tag{5.60}$$

Considering the bounds ensured by the projection operator, it can be found in Eq. (5.57) that:

$$\dot{V} \le -\hat{\mu}\left\|\boldsymbol{x}_e\right\|^2;\quad \left(0 < \hat{\mu} < \lambda_{\min}\right) \tag{5.61}$$

for any $\boldsymbol{x}_e$ such that $\left\|\boldsymbol{x}_e\right\| \ge \left\|\boldsymbol{H}\right\| n_\varepsilon \varepsilon^* / \left(\lambda_{\min} - \hat{\mu}\right) > 0$. Then, according to Theorem 4.18 in [67], the dynamics of $\boldsymbol{x}_e$ is ultimately bounded.

□

The zero dynamics of the closed-loop system in Eq. (5.48), i.e. the dynamics of $\boldsymbol{\eta}$, can be shown to be stable. The stability analysis is shown in Appendix.

7.3. Linear H_∞ Control for System Stabilization

The nonlinear adaptive controller designed in the previous section can drive the actuated independent coordinate $\boldsymbol{q}$ to track the desired trajectory, but it cannot directly regulate the dynamics of the underactuated coordinate $\boldsymbol{\eta}$. When the system is in the vicinity of the deployed configuration, a controller is needed to stabilize $\boldsymbol{q}$ and $\boldsymbol{\eta}$ at the equilibrium.

Since the modal coordinates cannot be measured, the generalized coordinates in Eq. (5.18) are used. In other words, the relative deflections of K points on the membrane are used as generalized coordinates for membrane relative vibrations instead of membrane modal coordinates.

The linear system derived by linearizing the nonlinear system in Eq. (5.27) around the deployed configuration, $\boldsymbol{z}_e = [\boldsymbol{q}_e^T \quad \boldsymbol{O}]^T$, can be generally expressed as:

$$\begin{aligned} \dot{\boldsymbol{x}}_z &= \boldsymbol{A}\boldsymbol{x}_z + \boldsymbol{B}_1\boldsymbol{w} + \boldsymbol{B}_2\boldsymbol{u} \\ \boldsymbol{p} &= \boldsymbol{C}_1\boldsymbol{x}_z + \boldsymbol{D}_{11}\boldsymbol{w} + \boldsymbol{D}_{12}\boldsymbol{u} \\ \boldsymbol{y} &= \boldsymbol{C}_2\boldsymbol{x}_z + \boldsymbol{D}_{21}\boldsymbol{w} + \boldsymbol{D}_{22}\boldsymbol{u} \end{aligned} \tag{5.62}$$

where $\boldsymbol{w}$ is the vector of exogenous inputs, including plant disturbances, noise, etc., $\boldsymbol{p}$ is the vector of the regulated output, and $\boldsymbol{y}$ is the vector of the measured outputs. The state variable $\boldsymbol{x}_z$ can be expressed as: $\boldsymbol{x}_z = [\tilde{\boldsymbol{z}}^T \quad \dot{\tilde{\boldsymbol{z}}}^T]^T$. Note that the variables in Eq. (5.62) represent small perturbations and should not be confused with the variables with the same symbols in the nonlinear model in previous sections. Without loss of generality, it is assumed that $\boldsymbol{D}_{22} = \boldsymbol{O}$.

According to the system interconnection shown in Figure 7.1, the exogenous input vector $\boldsymbol{w}$ can be written as: $\boldsymbol{w} = [\boldsymbol{q}_d^T \quad \boldsymbol{v}_d^T \quad \boldsymbol{n}_q^T \quad \boldsymbol{n}_v^T \quad \boldsymbol{n}_{\dot{q}}^T \quad \boldsymbol{n}_{\dot{v}}^T]^T$, where $\boldsymbol{q}_d$ and $\boldsymbol{v}_d$ are

the reference signals for $\boldsymbol{q}$ and $\boldsymbol{v}$, respectively. Here $\boldsymbol{n}_q$, $\boldsymbol{n}_v$, $\boldsymbol{n}_{\dot{q}}$, and $\boldsymbol{n}_{\dot{v}}$ represent the measurement noise and disturbances. The regulated output vector $\boldsymbol{p}$ can be expressed as: $\boldsymbol{p} = [\boldsymbol{e}_d{}^T \quad \boldsymbol{e}_u{}^T]^T$.

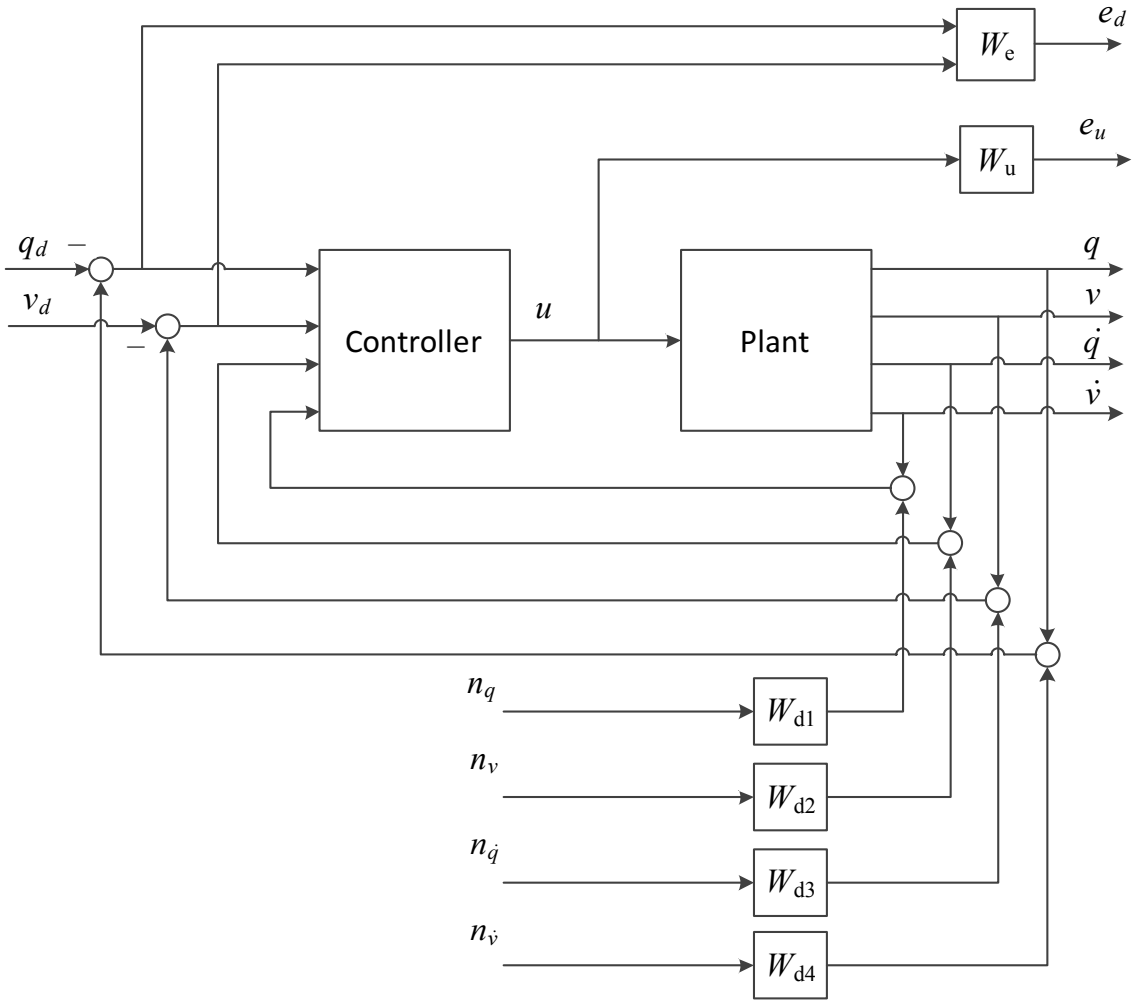

Figure 7.1. System interconnection

To minimize the effect of $\boldsymbol{w}$ on $\boldsymbol{p}$, the H_∞ norm of the transfer matrix $\boldsymbol{G}_{\boldsymbol{pw}}(s)$ from $\boldsymbol{w}$ on $\boldsymbol{p}$ should be smaller than a certain constant γ. This condition can be written as:

$$\left\| \boldsymbol{G}_{\boldsymbol{pw}} \right\|_\infty = \sup_{\|\boldsymbol{w}\|_2 \neq 0,\ \boldsymbol{w} \in L_2} \frac{\|\boldsymbol{p}\|_2}{\|\boldsymbol{w}\|_2} < \gamma \tag{5.63}$$

where $\|\boldsymbol{G}_{pw}\|_\infty$ is the H_∞ norm of $\boldsymbol{G}_{pw}$ and $\|\boldsymbol{p}\|_2$ represents the L_2 norm of $\boldsymbol{p}$. If the open-loop system in Eq. (5.62) is controllable and observable, to make the corresponding closed-loop system satisfy Eq. (5.63) is equivalent to the condition that there exists a symmetric positive definite solution $\boldsymbol{X}$ to the LMI [68, 69]:

$$\begin{bmatrix} \boldsymbol{A}_{cl}{}^T\boldsymbol{X} + \boldsymbol{X}\boldsymbol{A}_{cl} & \boldsymbol{B}_{cl} & \boldsymbol{X}\boldsymbol{C}_{cl}{}^T \\ \boldsymbol{B}_{cl}{}^T & -\gamma\boldsymbol{I} & \boldsymbol{D}_{cl}{}^T \\ \boldsymbol{C}_{cl}\boldsymbol{X} & \boldsymbol{D}_{cl} & -\gamma\boldsymbol{I} \end{bmatrix} \prec \boldsymbol{O} \tag{5.64}$$

where subscript *cl* indicates the terms of the closed-loop system. This condition is known as the Bounded Real Lemma.

In this work, the closed-loop system is desired to be α-stable, i.e. the real part of each closed-loop pole is desired to be less than $-\alpha_1$. A controller $\boldsymbol{K}(s) = \boldsymbol{D}_k + \boldsymbol{C}_k(s\boldsymbol{I} - \boldsymbol{A}_k)^{-1}\boldsymbol{B}_k$ that makes the closed-loop system satisfy Eq. (5.63) and the α-stability requirement can be determined by solving the following convex optimization problem [70]:

$$\begin{aligned} &\text{find} && \boldsymbol{R}, \boldsymbol{S}, \bar{\boldsymbol{A}}_k, \bar{\boldsymbol{B}}_k, \bar{\boldsymbol{C}}_k, \text{ and } \boldsymbol{D}_k \\ &\text{subject to} && \begin{bmatrix} \boldsymbol{R} & \boldsymbol{I} \\ \boldsymbol{I} & \boldsymbol{S} \end{bmatrix} \succ \boldsymbol{O} \\ & && \boldsymbol{\Psi}_{\mathbf{A}} + \boldsymbol{\Psi}_{\mathbf{A}}{}^T + 2\alpha_1 \begin{bmatrix} \boldsymbol{R} & \boldsymbol{I} \\ \boldsymbol{I} & \boldsymbol{S} \end{bmatrix} \prec \boldsymbol{O} \\ & && \begin{bmatrix} \boldsymbol{\Psi}_{\mathbf{A}} + \boldsymbol{\Psi}_{\mathbf{A}}{}^T & \boldsymbol{\Psi}_{\mathbf{B}} & \boldsymbol{\Psi}_{\mathbf{C}}{}^T \\ \boldsymbol{\Psi}_{\mathbf{B}}{}^T & -\gamma\boldsymbol{I} & \boldsymbol{\Psi}_{\mathbf{D}}{}^T \\ \boldsymbol{\Psi}_{\mathbf{C}} & \boldsymbol{\Psi}_{\mathbf{D}} & -\gamma\boldsymbol{I} \end{bmatrix} \prec \boldsymbol{O} \end{aligned} \tag{5.65}$$

where $\boldsymbol{R}$ and $\boldsymbol{S}$ are positive-definite symmetric matrices. Matrices $\boldsymbol{\Psi}_{\mathbf{A}}$, $\boldsymbol{\Psi}_{\mathbf{B}}$, $\boldsymbol{\Psi}_{\mathbf{C}}$, and $\boldsymbol{\Psi}_{\mathbf{D}}$ are:

$$\begin{aligned} \boldsymbol{\Psi}_{\mathbf{A}} &= \begin{bmatrix} \boldsymbol{A}\boldsymbol{R} + \boldsymbol{B}_2\bar{\boldsymbol{C}}_k & \boldsymbol{A} + \boldsymbol{B}_2\boldsymbol{D}_k\boldsymbol{C}_2 \\ \bar{\boldsymbol{A}}_k & \boldsymbol{S}\boldsymbol{A} + \bar{\boldsymbol{B}}_k\boldsymbol{C}_2 \end{bmatrix}; \qquad \boldsymbol{\Psi}_{\mathbf{B}} = \begin{bmatrix} \boldsymbol{B}_1 + \boldsymbol{B}_2\boldsymbol{D}_k\boldsymbol{D}_{21} \\ \boldsymbol{S}\boldsymbol{B}_1 + \bar{\boldsymbol{B}}_k\boldsymbol{D}_{21} \end{bmatrix} \\ \boldsymbol{\Psi}_{\mathbf{C}} &= \begin{bmatrix} \boldsymbol{C}_1\boldsymbol{R} + \boldsymbol{D}_{12}\bar{\boldsymbol{C}}_k & \boldsymbol{C}_1 + \boldsymbol{D}_{12}\boldsymbol{D}_k\boldsymbol{C}_2 \end{bmatrix}; \quad \boldsymbol{\Psi}_{\mathbf{D}} = \boldsymbol{D}_{11} + \boldsymbol{D}_{12}\boldsymbol{D}_k\boldsymbol{D}_{21} \end{aligned} \tag{5.66}$$

The controller $\boldsymbol{K}(s)$ can be found using the following equations:

$$\begin{aligned}
&\boldsymbol{M}\boldsymbol{N}^T = \boldsymbol{I} - \boldsymbol{R}\boldsymbol{S} \\
&\bar{\boldsymbol{B}}_k = \boldsymbol{N}\boldsymbol{B}_k + \boldsymbol{S}\boldsymbol{B}_2\boldsymbol{D}_k \\
&\bar{\boldsymbol{C}}_k = \boldsymbol{C}_k\boldsymbol{M}^T + \boldsymbol{D}_k\boldsymbol{C}_2\boldsymbol{R} \\
&\bar{\boldsymbol{A}}_k = \boldsymbol{N}\boldsymbol{A}_k\boldsymbol{M}^T + \boldsymbol{N}\boldsymbol{B}_k\boldsymbol{C}_2\boldsymbol{R} + \boldsymbol{S}\boldsymbol{B}_2\boldsymbol{C}_k\boldsymbol{M}^T + \boldsymbol{S}\left(\boldsymbol{A} + \boldsymbol{B}_2\boldsymbol{D}_k\boldsymbol{C}_2\right)\boldsymbol{R}
\end{aligned} \tag{5.67}$$

The LMIs in Eq. (5.65) can be solved by using existing numerical solvers (e.g. CVX). More details about the numerical results of the controller parameters are given in the next section.

7.4. Simulation Results

In this section, simulation results of the deployment of three tensegrity-membrane systems, i.e. a 1-4(D) symmetric system, a 1-6(D) symmetric system, and a 2-3 symmetric system, are presented

For each system, the desired trajectory $\boldsymbol{q_d}$ is chosen to belong to the set of symmetric equilibriums. According to the static analysis in Chapter 3, $\boldsymbol{q_d}$ can be specified by the reference declination angle, θ_r, and the reference azimuth angle, ψ_r. Here, the value of θ_r is generated by a second order system:

$$\begin{aligned}
&\ddot{\theta}_r(t) + 2\xi_r\omega_r\dot{\theta}_r(t) + \omega_r{}^2\theta_r(t) = \omega_r{}^2\theta_e \\
&\theta_r(0) = \theta_0; \quad \dot{\theta}_r(0) = 0
\end{aligned} \tag{5.68}$$

where subscripts 0 and e indicate the value of initial and final configurations, respectively. For the 1-4(D) system, ξ_r and ω_r are chosen as: ξ_r = 1, ω_r = 0.7. For the 1-6(D) system, ξ_r = 1, ω_r = 0.35. For the 2-3 system, ξ_r = 1, ω_r = 0.5. Clearly, for each system, the desired trajectory is generated by a critically damped second-order system. The settling time of θ_r is 6.79 seconds, 13.57 seconds, and 9.5 seconds for the 1-4(D)

system, the 1-6(D) system, and the 2-3 system, respectively [71]. It is known that the responses of critically damped second-order systems are free from overshoot compared to the responses of underdamped systems and have the shortest settling time compared to the responses of overdamped systems.

For the 1-4(D) system and the 1-6(D) system, the corresponding values of ψ_r can be determined based on the equilibrium conditions in Eq. (3.41). For the 2-3 system, the deployment trajectory is selected to be one desired trajectory in the region of system equilibriums. Such a region of system equilibriums can be calculated numerically based on the equilibrium finding method discussed in Chapter 3.

Since tendons can only carry tensile loads, tendon lengths are treated as control limits and tendon rest-lengths should not exceed the corresponding tendon lengths. Note that the control limits are variable during system deployment but fixed at the final deployed configuration.

Based on the Lyapunov stability analysis for the nonlinear adaptive controller shown in Section 7.3, controller parameters $d_q(t)$ and $k_q(t)$ with large values can minimize the tracking error. On the other hand, large $d_q(t)$ and $k_q(t)$ will introduce large transient control signals, which may exceed the control limits. To balance these two performance criteria, the following controller parameters are used:

$$\begin{aligned} &\omega(t) = \omega_0 + \omega_e\left(1-\exp\left(-t/\tau\right)\right) \\ &d_q(t) = 2d_c\omega(t); \quad k_q(t) = \omega(t)^2 \end{aligned} \tag{5.69}$$

The nonlinear adaptive controller is implemented first to deploy the system from the initial configuration to the final configuration. The initial value of $\boldsymbol{W_F}$ is set to be zero and Γ is chosen as $\Gamma = 0.01$. Parameters α and β in Eq. (5.50) are chosen as $\alpha = \beta = 1$.

The H_∞ controller becomes active in order to stabilize the system at the final configuration when the following control switching condition is satisfied:

$$\left\| \frac{\boldsymbol{q} - \boldsymbol{q}_d}{\boldsymbol{q}_d} \right\|_2 \leq R_c \tag{5.70}$$

For the three systems, R_c is chosen as R_c = 0.01. Parameters of nonlinear adaptive controllers are listed in Table 7.1.

Table 7.1. Parameters of nonlinear adaptive controllers

	ω_0	ω_e	τ	d_c
1-4(D) system	15	150	20	1.5
1-6(D) system	4	10	20	0.7
2-3 system	1	24	5	0.9

For the H_∞ control design, the weighting functions used in this work are:

1. For the three systems, $\boldsymbol{W}_\mathbf{e}$ is defined as: $\boldsymbol{W}_\mathbf{e} = 0.5\boldsymbol{I}$.
2. The weighting functions corresponding to the measurement noise are chosen as: $\boldsymbol{W}_\mathbf{d1} = \boldsymbol{W}_\mathbf{d2} = \boldsymbol{W}_\mathbf{d3} = \boldsymbol{W}_\mathbf{d4} = 0.001\boldsymbol{I}$ for the three systems.
3. The weighting function $\boldsymbol{W}_\mathbf{u}$ is defined as: $\boldsymbol{W}_\mathbf{u} = 1/u_m\boldsymbol{I}$, which indicates that the variations of the control inputs, i.e. variations of the tendon rest-lengths, are desired to be smaller than u_m meters. For the 1-4(D) system and the 2-3 system, u_m = 0.01. For the 1-6(D) system, u_m = 0.02.
4. For the 1-4(D) system, the parameter for the α-stability requirement, i.e. α_1, is chosen as: α_1 = 0.5. For the 1-6(D) system and the 2-3 system, α_1 = 0.4.

Simulation programs are coded in Mathematica 8. The nonlinear system is solved based on Park's method, which is designed for stiff systems. Time steps for the numerical solver are determined based on the Shannon sampling theorem [72], which indicates that the sampling frequency should be at least two times higher than the highest natural frequency of the system. This theorem is widely used in the field of digital signal processing and provides a sufficient condition for a sample rate that permits a discrete sequence of samples to capture all the information from a continuous-time signal of finite bandwidth. More details of time step selection are presented in the following sections.

7.4.1. 1-4(D) System

For this 1-4(D) system, a 20×20 mesh is used for the square membrane. The materials for the membrane, bars, and tendons are chosen as Kapton, wood, and Nylon, respectively. The material and geometrical parameters of bars and tendons are listed in Table 7.2. The first three modes are used to describe the vibration of the membrane. Based on the modal analysis results, the first three modes are all transverse vibration modes.

In this work, the Popov-Belevitch-Hautus (PBH) eigenvector test [73] is used to check the controllability and observability of the linearized system at the deployed configuration. Consider the following linear time-invariant (LTI) system:

$$\begin{aligned} \dot{\boldsymbol{x}} &= \boldsymbol{A}\boldsymbol{x} + \boldsymbol{B}\boldsymbol{u}; \quad \boldsymbol{x}\left(t_0\right) = \boldsymbol{x}_0 \\ \boldsymbol{y} &= \boldsymbol{C}\boldsymbol{x} + \boldsymbol{D}\boldsymbol{u} \end{aligned} \tag{5.71}$$

The PBH controllability criterion is: the LTI system in Eq. (5.71) is uncontrollable if and only if there exists a left eigenvector $\tilde{\boldsymbol{v}}$ of $\boldsymbol{A}$ such that $\tilde{\boldsymbol{v}}^T\boldsymbol{B} = \boldsymbol{O}$. The PBH observability criterion is: the LTI system in Eq. (5.71) is unobservable if and only if there exists a right

eigenvector $\hat{\boldsymbol{v}}$ of $\boldsymbol{A}$ such that $\boldsymbol{C}\hat{\boldsymbol{v}} = \boldsymbol{O}$. After applying the PBH test, the linearized model of this 1-4(D) system is found to be controllable and observable.

Table 7.2. Material and geometrical parameters of the 1-4(D) system

	Membrane	Bar	Tendon SL_i	Tendon SU_i
Young's modulus	165 MPa	11 GPa	2 GPa	2 GPa
Density	1400 kg/m^3	800 kg/m^3	N/A	N/A
Poisson's ratio	0.34	N/A	N/A	N/A
Thickness	51 μm	N/A	N/A	N/A
Cross section diameter	N/A	0.03 mm	0.8 mm	0.4 mm

The highest natural frequency of the open-loop linear system is f_{max} = 7.32 Hz. In order to capture the complete system dynamics, the sampling frequency is chosen to be approximately 10 times higher than f_{max}, which gives the corresponding time step Δt = 0.01s.

Equilibrium parameters are shown in Table 7.3. The initial configuration and the final configuration are determined based on the equilibrium finding method presented in Chapter 3. The radius of the membrane's circumscribed circle is r_{mb} = 1.414 m. The length of each bar is chosen as l_{1j} = 2.2 m. The circumscribed circle radius of the system base is r_1 = 0.79 m.

Table 7.3. Equilibrium parameters of the 1-4(D) system

	Initial configuration	Final configuration
Declination angle (θ)	87.6º	75º
Azimuth angle (ψ)	38.4º	30º
Rest-length of tendon SL_i	0.7502 m	0.6726 m
Rest-length of tendon SU_i	1.4785 m	1.7720 m

The uncertainty in Eq. (5.42) is modeled as:

$$\Delta \boldsymbol{F}_{\boldsymbol{q}} = \boldsymbol{F}_{\boldsymbol{q}}^{*} - \left(\boldsymbol{F}_{\boldsymbol{q}}^{*}\Big|_{(\theta_0,\, \psi_0)} \right) \tag{5.72}$$

In other words, it is assumed that we only know the information of $\boldsymbol{F}_{\boldsymbol{q}}^{*}$ at the system's initial configuration, which is used to represent the nominal model $\boldsymbol{F}_{\boldsymbol{q}}$.

The deflections of 3 points on the membrane, w_1, w_2, and w_3, are monitored. The locations of the 3 points are characterized by:

$$\begin{aligned} w_1 &= w^r\left(x_f, y_f\right)\Big|_{x_f = 1\ (\mathrm{m});\ \ y_f = 1\ (\mathrm{m})} \\ w_2 &= w^r\left(x_f, y_f\right)\Big|_{x_f = 2\ (\mathrm{m});\ \ y_f = 1\ (\mathrm{m})} \\ w_3 &= w^r\left(x_f, y_f\right)\Big|_{x_f = 1\ (\mathrm{m});\ \ y_f = 2\ (\mathrm{m})} \end{aligned} \tag{5.73}$$

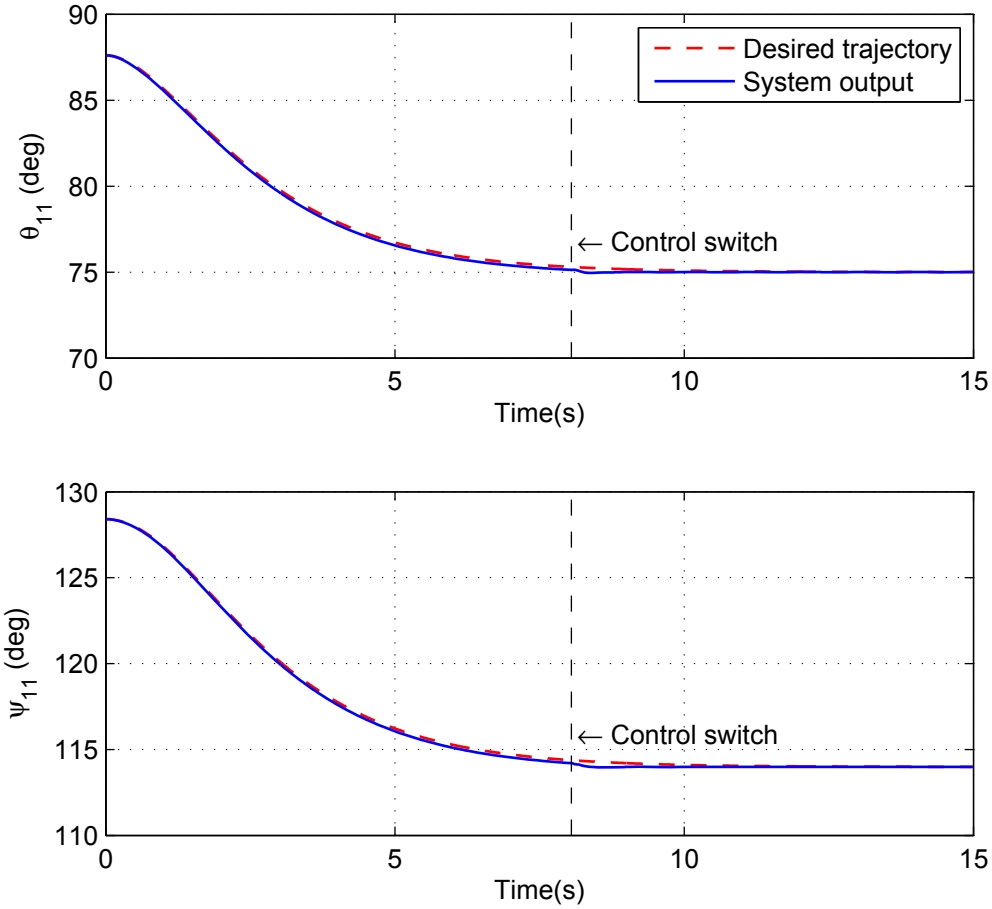

Figure 7.2. Representative responses of bar attitudes of the 1-4(D) system

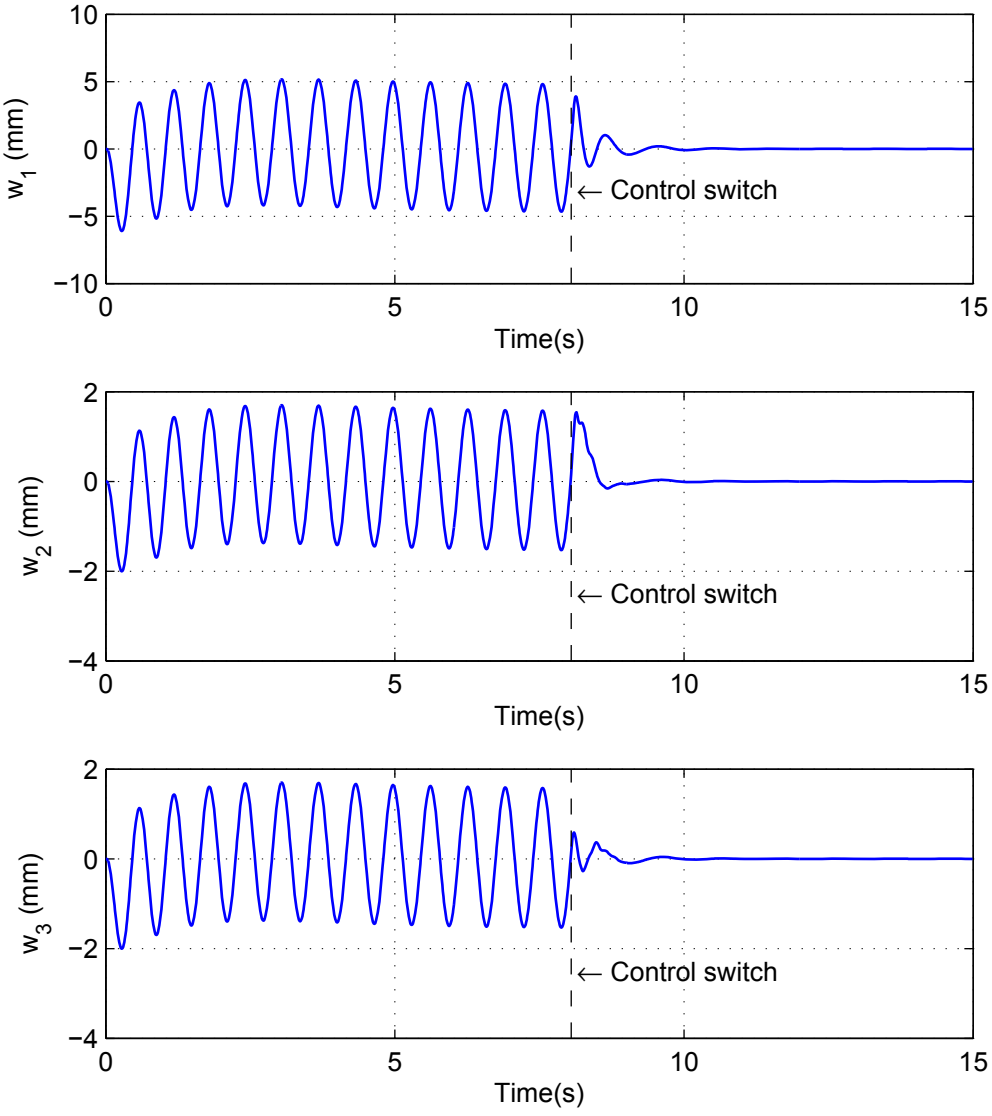

Figure 7.3. Responses of w_1, w_2, and w_3 of the 1-4(D) system

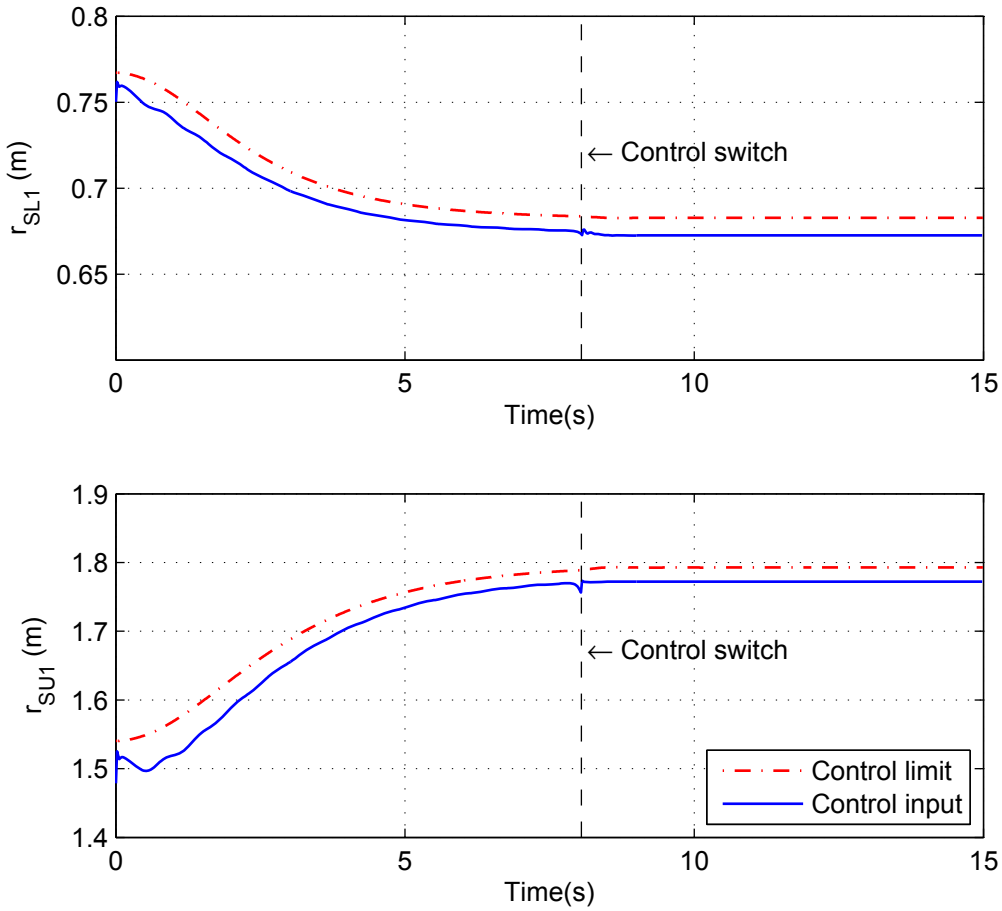

Figure 7.4. Representative tendon rest-length variations of the 1-4(D) system

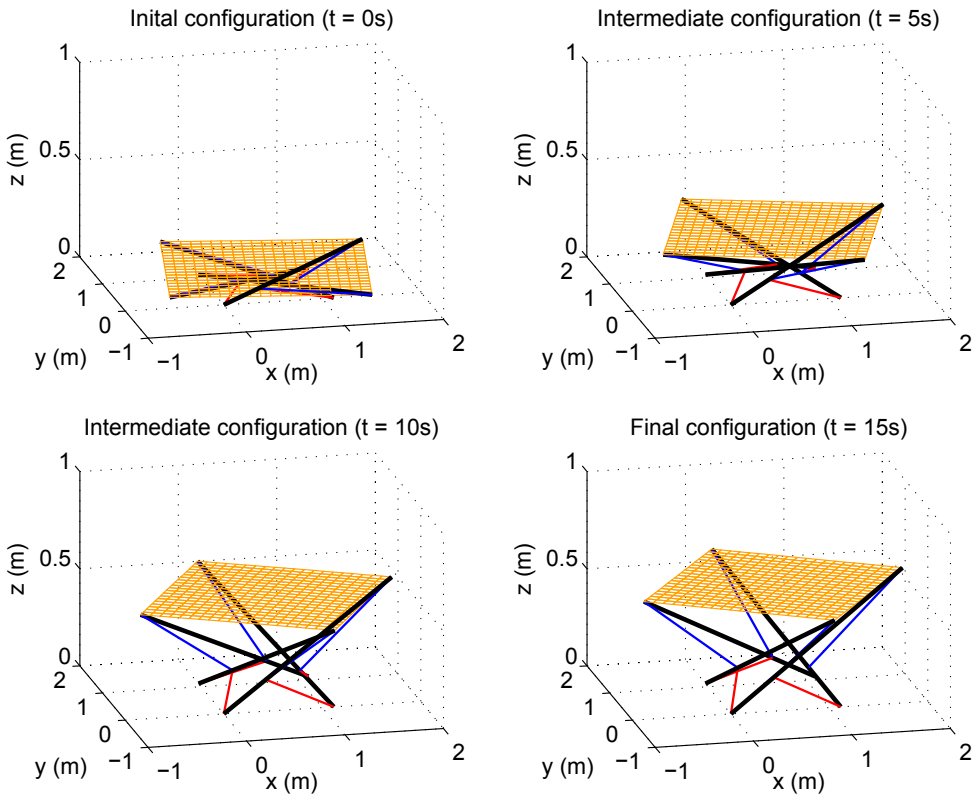

Figure 7.5. Deployment sequence of the 1-4(D) system

In Figure 7.2, it can be observed that the nonlinear adaptive controller can drive the 1-4(D) system from the initial configuration to the final configuration and make the actuated coordinates, i.e. the attitudes of bars, track the desired trajectory.

Figure 7.5 shows snapshots of the deployment process of the 1-4(D) system. We can observe that the 1-4(D) system experiences significant shape changes during deployment, while the membrane transverse deflections cannot be clearly seen. This coincides with the results shown in Figure 7.3, where the magnitude of the membrane relative transverse deflections is less than 7 mm. This observation indicates that the control strategy does not introduce significant undesired membrane vibrations during deployment. Control switch occurs at t = 8.05s. In Figure 7.2 and Figure 7.3, it can be also seen that, after the control

switch, the entire 1-4(D) system is rapidly stabilized by the H_∞ controller at the final deployed configuration. There is no significant variation of control inputs after the control switch.

During system deployment, the peak compressive load on bars during deployment is 3.68N. The critical load of bars determined by Euler's column buckling formula is 891.9N. Clearly, the peak compressive load is less than the critical load. Therefore, we can conclude that the bars do not buckle during deployment. The yield analysis for the membrane is conducted based on the von Mises criterion. The maximum von Mises stress in the membrane is 2.9MPa during deployment. It is less than the yield stress at 3% for Kapton which is 61MPa [74]. Thus, the membrane does not yield and remains linearly elastic during system deployment. The maximum stress in tendons during deployment is 83MPa. It is less than the yield stress of Nylon which is 94.8MPa [75]. Clearly, the tendons do not yield during system deployment.

7.4.2. 1-6(D) System

The hexagonal membrane is divided into 6 quadrilaterals, and a 10×10 mesh is used for each quadrilateral. The materials for the membrane, bars, and tendons are chosen as Kapton, wood, and Nylon, respectively. For the 1-6(D) system, the parameters of bars and the membrane are the same as those listed in Table 7.2. The parameters of tendons are listed in Table 7.4.

The first five modes are used to describe the vibration of the membrane. These five modes are all transverse vibration modes. The PBH test result indicates that the linearized model of this system is controllable and observable.

Table 7.4. Tendon parameters of the 1-6(D) system

	Young's modulus	Cross section diameter
Tendon SL_i	2 GPa	0.8 mm
Tendon SU_i	2 GPa	0.4 mm

The highest natural frequency of the open-loop linear system is f_{max} = 8.59 Hz. In order to capture the complete system dynamics, the sampling frequency is chosen to be approximately 10 times higher than f_{max}, which gives the corresponding time step Δt = 0.01s.

Table 7.5. Equilibrium parameters of the 1-6(D) system

	Initial configuration	Final configuration
Declination angle (θ)	88.6º	72º
Azimuth angle (ψ)	33.2º	24.5º
Rest-length of tendon SL_i	0.6909 m	0.6566 m
Rest-length of tendon SU_i	2.5350 m	2.7457 m

The equilibrium parameters are shown in Table 7.5. The initial configuration and the final configuration are determined based on the equilibrium finding method presented in Chapter 3. The radius of the membrane's circumscribed circle is r_{mb} = 2 m. The length of each bar is chosen as l_{1j} = 3 m. The circumscribed circle radius of the system base is r_1 = 1.2 m.

The uncertainty in Eq. (5.42) is modeled by ignoring the term $\boldsymbol{M}(\boldsymbol{x})\boldsymbol{G}$ in Eq. (5.28). The deflections of 3 points on the membrane, w_1, w_2, and w_3, are monitored:

$$\begin{aligned} w_1 &= w^r\left(x_f, y_f\right)\Big|_{x_f = 1\ (\mathrm{m});\ \ y_f = 1.732\ (\mathrm{m})} \\ w_2 &= w^r\left(x_f, y_f\right)\Big|_{x_f = 2.5\ (\mathrm{m});\ \ y_f = 0.866\ (\mathrm{m})} \\ w_3 &= w^r\left(x_f, y_f\right)\Big|_{x_f = 2.5\ (\mathrm{m});\ \ y_f = 2.598\ (\mathrm{m})} \end{aligned} \tag{5.74}$$

In Figure 7.6, the simulation results indicate that the nonlinear adaptive controller can drive the 1-6(D) system from the initial configuration to the final deployed configuration. The actuated coordinates, i.e. the attitudes of bars, can track the desired trajectory accurately. Simulation results of membrane transverse deflections are shown in Figure 7.7. The amplitude of the membrane relative transverse vibrations is less than 6 mm.

Snapshots of the system deployment process are shown in Figure 7.9. It can be seen that the 1-6(D) system experiences significant shape changes during deployment, while the membrane transverse deflections cannot be clearly seen. This observation coincides with the results shown in Figure 7.7 that membrane transverse deflections are small. This observation also indicates that the control strategy does not introduce significant undesired membrane vibrations during deployment. Control switch occurs at t = 18.44s. In Figure 7.6 and Figure 7.7, it can be seen that, after the control switch, the entire 1-6(D) system is rapidly stabilized by the H_∞ controller at the final deployed configuration. It can be observed that there is no significant variation after control switch.

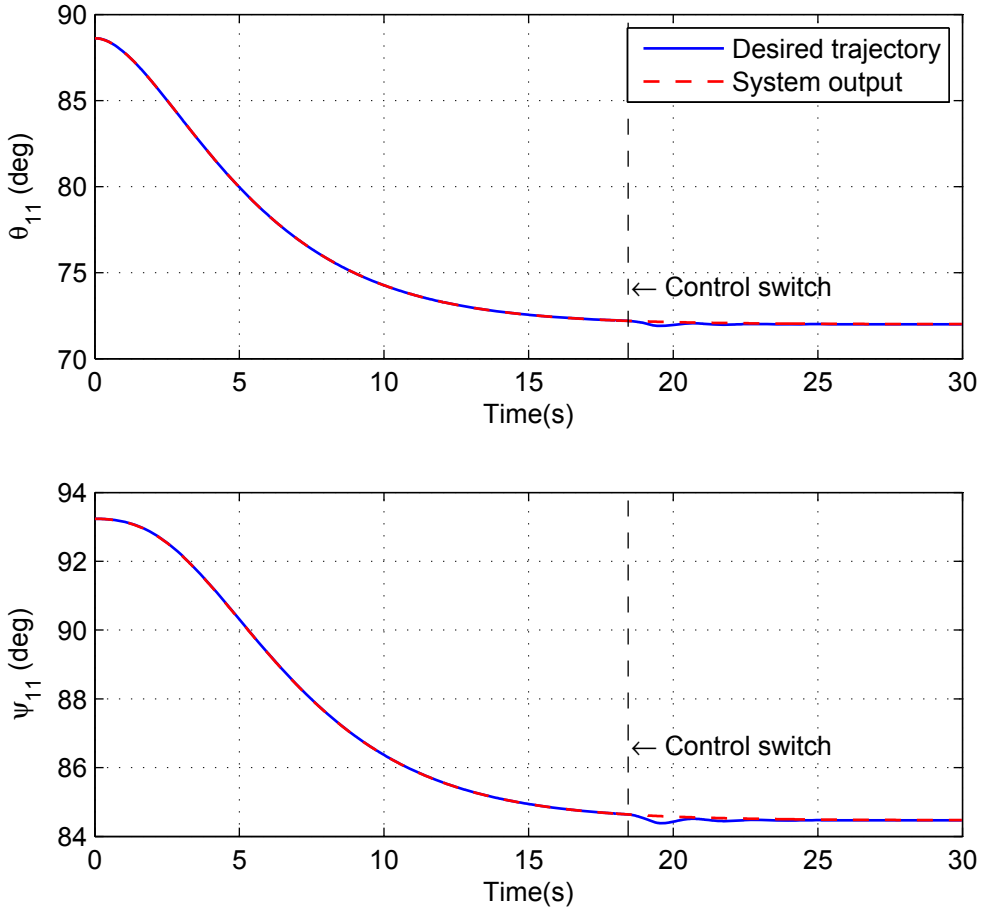

Figure 7.6. Representative responses of bar attitude of the 1-6(D) system

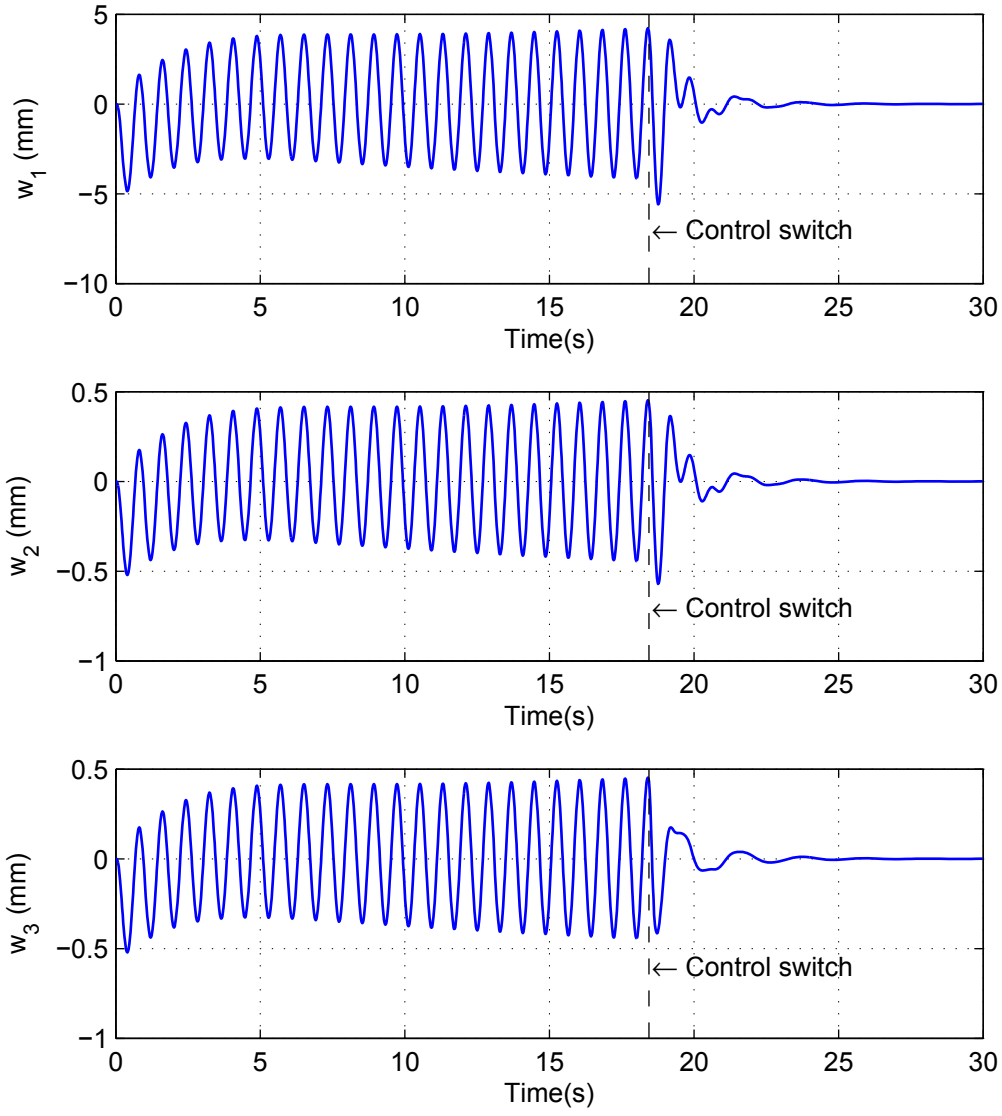

Figure 7.7. Responses of w_1, w_2, and w_3 of the 1-6(D) system

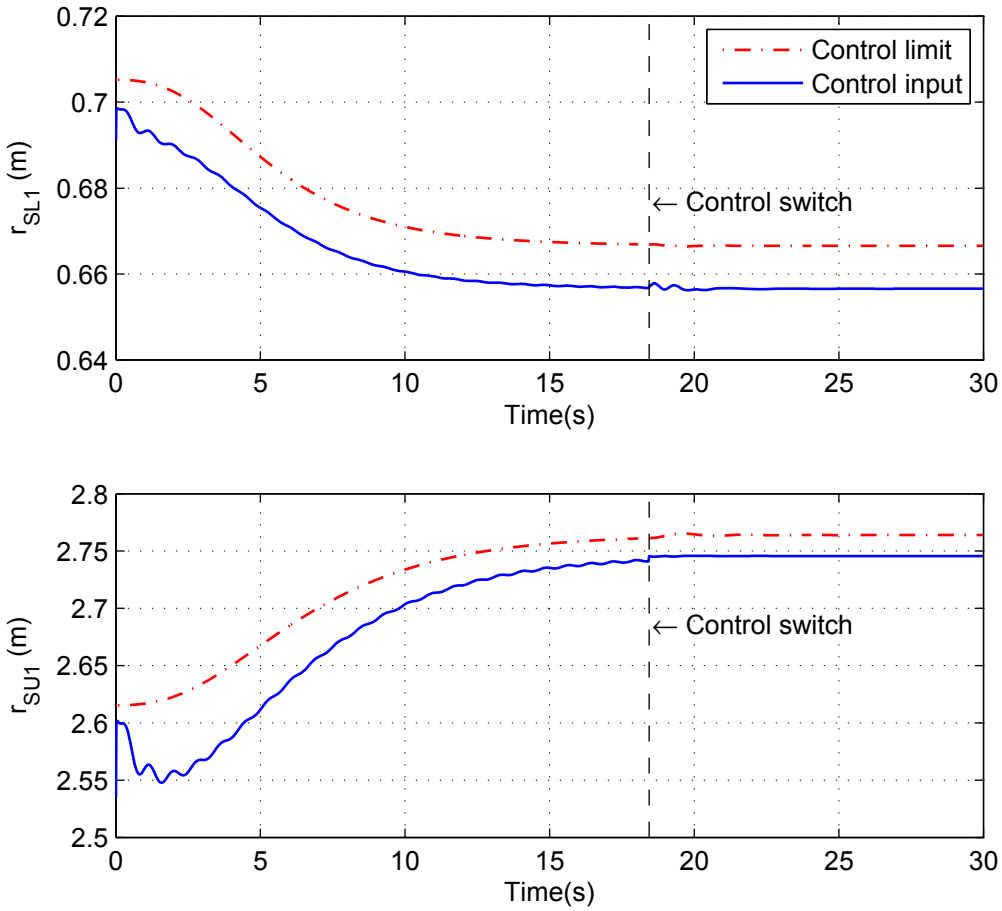

Figure 7.8. Representative tendon rest-length variations of the 1-6(D) system

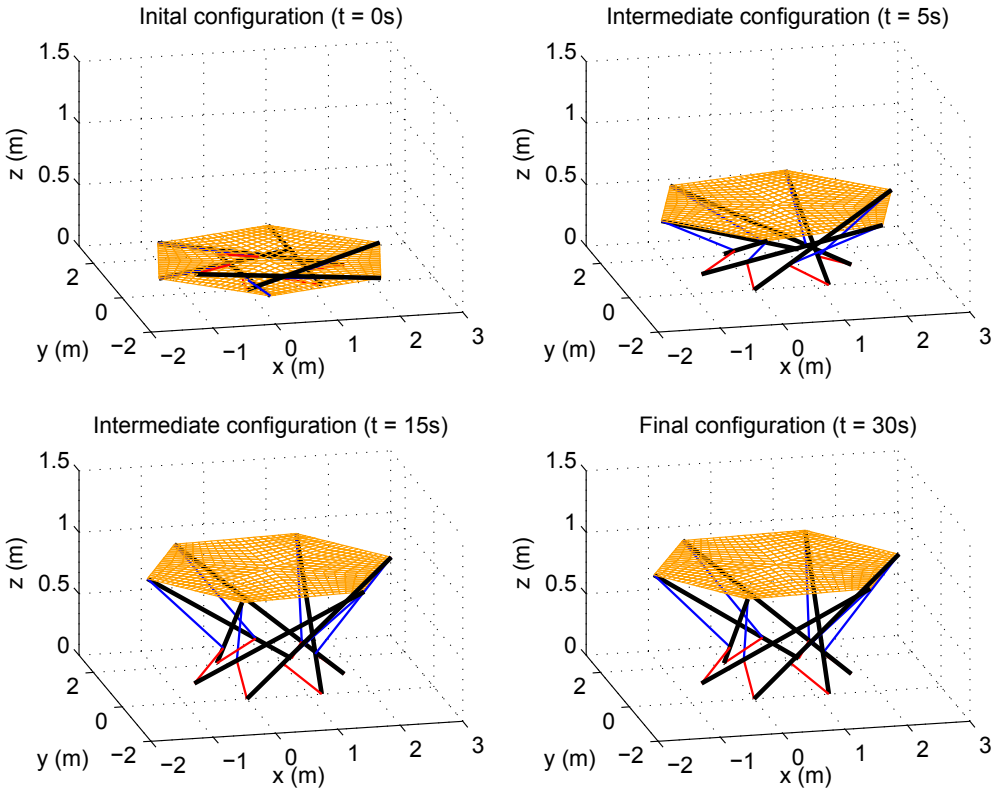

Figure 7.9. Deployment sequence of the 1-6(D) system

During system deployment, the peak compressive load on bars is 1.06N. The critical load of bars is 479.6N. Clearly, the bars do not buckle during deployment and can be treated as rigid bodies. The maximum von Mises stress in the membrane is 3.53MPa, which is less than the yield stress at 3% for Kapton. The maximum stress in tendons is 63.3MPa, which is less than the yield stress of Nylon. Therefore, the membrane and tendons do not yield during system deployment.

7.4.3. 2-3 System

For this system, the triangular membrane is divided into 3 quadrilaterals, and a 10×10 mesh is used for each quadrilateral. The materials for the membrane, bars, and tendons

are chosen as Kapton, wood, and Nylon, respectively. The material and geometrical parameters of bars and the membrane are the same as those listed in Table 7.2. The parameters of tendons for the 2-3 system are listed in Table 7.6.

Table 7.6. Tendon parameters of the 2-3 system

	Young's modulus	Cross section diameter
Tendon S_{1j}	2 GPa	0.254 mm
Tendon S_{2j}	2 GPa	0.254 mm
Tendon V_{2j}	2 GPa	0.254 mm
Tendon R_{2j}	2 GPa	0.254 mm
Tendon P_{2j}	2 GPa	0.254 mm
Tendon C_{2j}	2 GPa	0.4 mm
Tendon D_{2j}	2 GPa	0.4 mm

The first four modes are used to describe the membrane vibrations. These four modes are all transverse vibration modes according to the numerical results. The PBH test result indicates that the linearized model of this system is controllable and observable.

The highest natural frequency of the open-loop linear system is f_{max} = 9.83 Hz. In order to capture the complete system dynamics, the sampling frequency is chosen to be approximately 10 times higher than f_{max}, which gives the corresponding time step Δt = 0.01s.

The equilibrium parameters of the system are listed in Table 7.7. The initial configuration and the final configuration are determined based on the equilibrium finding

method presented in Chapter 3. The radius of the membrane's circumscribed circle is r_{mb} = 1 m. The length of bars is chosen as $l_1 j = l_2 j$ = 1.8 m. The circumscribed circle radius of the system base is r_1 = 0.75 m.

Table 7.7. Equilibrium parameters of the 2-3 system

	Initial configuration	Final configuration
Declination angle (θ_{1j} / θ_{2j})	79.63º/79.63º	55º/55º
Azimuth angle (ψ_{1j} / ψ_{2j})	10º/−24.86 º	10º/−24.86 º
Rest-length of tendon S_{1j}	0.6159 m	1.0286 m
Rest-length of tendon V_{2j}	0.9624 m	0.7736 m
Rest-length of tendon D_{2j}	1.0075 m	0.7199 m
Rest-length of tendon C_{2j}	1.1153 m	1.1094 m
Rest-length of tendon R_{2j}	1.3658 m	1.4835 m
Rest-length of tendon P_{2j}	0.7302 m	0.8459 m
Rest-length of tendon S_{2j}	0.5070 m	1.1831 m

The deflections of 3 points on the membrane, w_1, w_2, and w_3, are monitored:

$$\begin{aligned} w_1 &= w^r\left(x_f, y_f\right)\Big|_{x_f=0.866\ (\mathrm{m});\ \ y_f=0.5\ (\mathrm{m})} \\ w_2 &= w^r\left(x_f, y_f\right)\Big|_{x_f=1.30\ (\mathrm{m});\ \ y_f=0.75\ (\mathrm{m})} \\ w_3 &= w^r\left(x_f, y_f\right)\Big|_{x_f=0.433\ (\mathrm{m});\ \ y_f=0.75\ (\mathrm{m})} \end{aligned} \tag{5.75}$$

For this 2-3 system, the uncertainty in Eq. (5.42) is modeled by ignoring the term $\boldsymbol{M}(\boldsymbol{x})\boldsymbol{G}$ in Eq. (5.28).

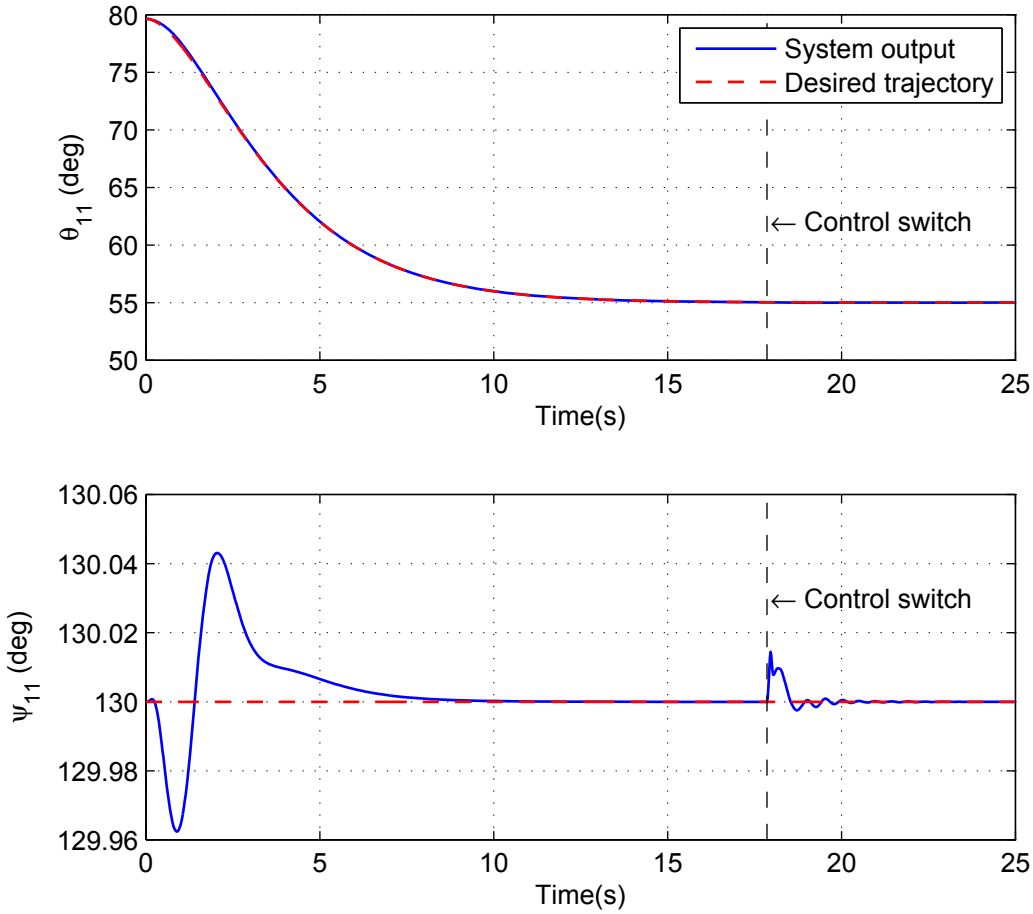

Figure 7.10. Responses of attitudes of bar b_{11} of the 2-3 system

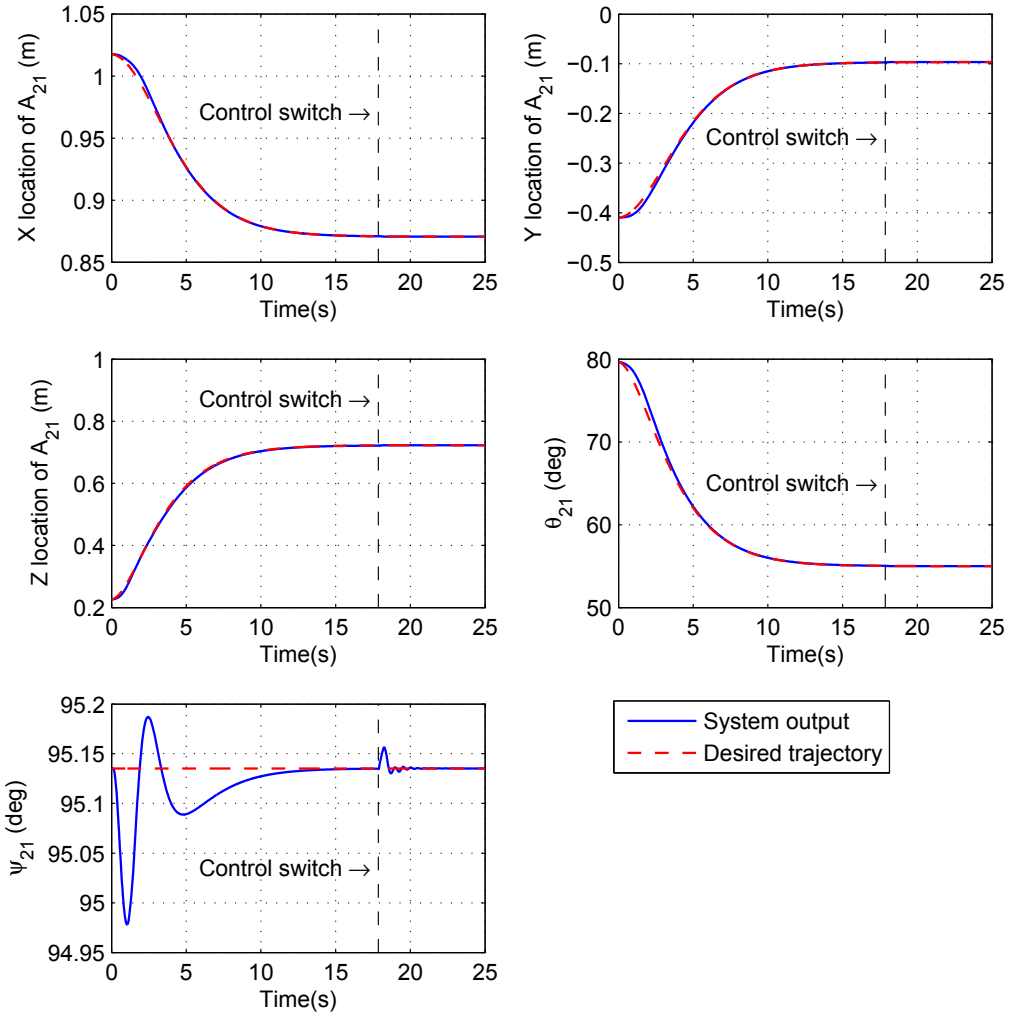

Figure 7.11. Responses of locations and attitudes of bar b_{21} of the 2-3 system

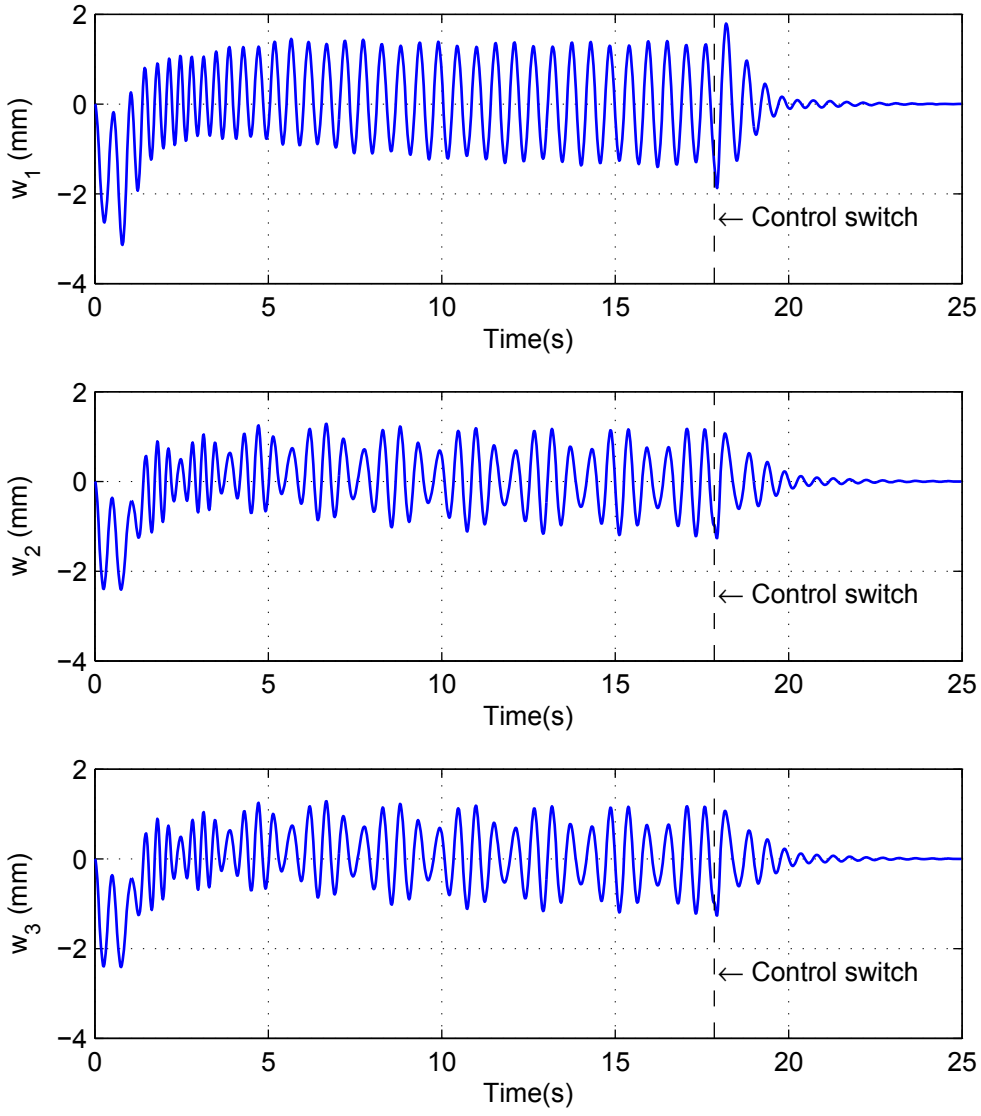

Figure 7.12. Responses of w_1, w_2, and w_3 of the 2-3 system

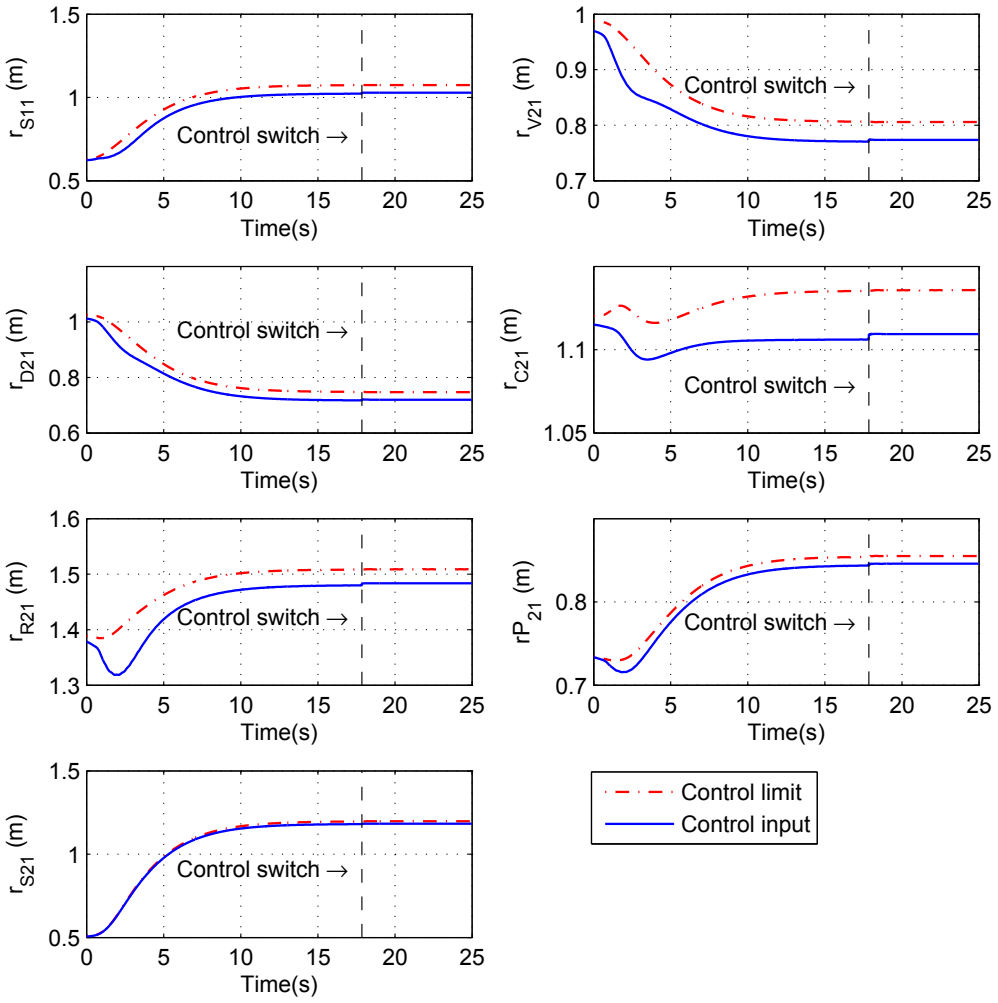

Figure 7.13. Representative tendon rest-length variations of the 2-3 system

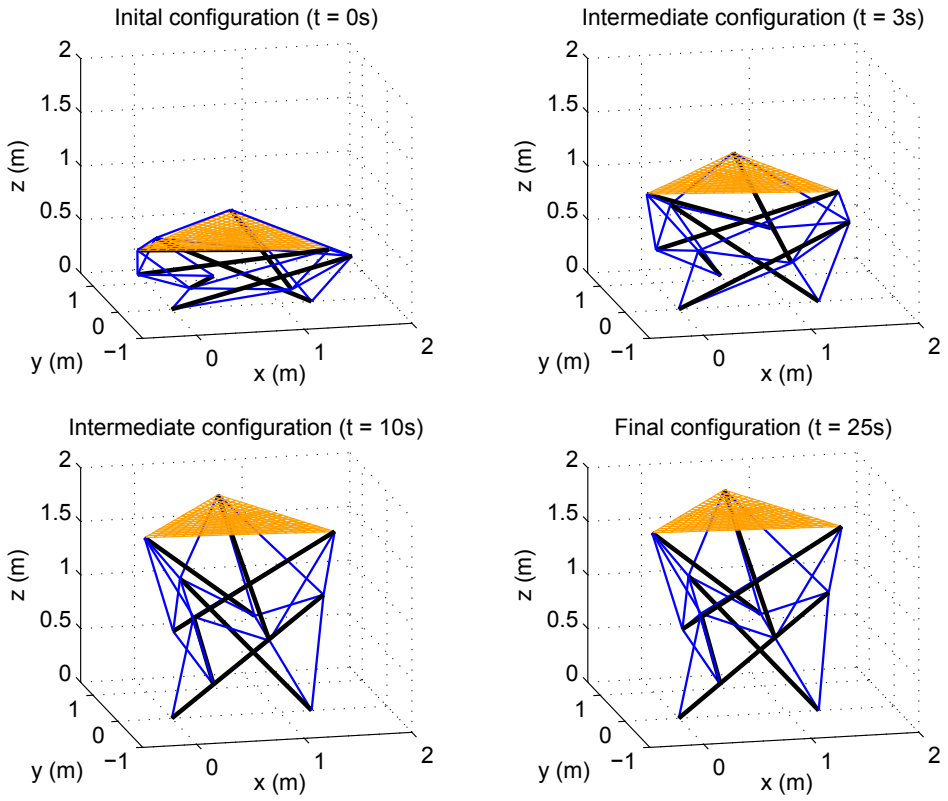

Figure 7.14. Deployment sequence of the 2-3 system

The simulation results in Figure 7.10 and Figure 7.11 indicate that the nonlinear adaptive controller can make the actuated coordinates, i.e. the locations and attitudes of bars, track the desired trajectory. Snapshots of the system deployment process of the 2-3 system are shown in Figure 7.14. The 2-3 system experiences significant shape changes during deployment, while the membrane transverse deflections cannot be clearly seen. This coincides with the results shown in Figure 7.12, where the magnitude of the membrane relative transverse deflections is less than 5 mm. This observation indicates that this control strategy does not introduce significant undesired membrane vibrations during system deployment.

Control switch occurs at t = 17.86s. In Figure 7.10 - Figure 7.12, it can be seen that, after the control switch, the entire 2-3 system is rapidly stabilized by the H_∞ controller at the final deployed configuration. Simulation results show that there is no significant variation after control switch.

During system deployment, the peak compressive load on bars during deployment is 7.17N. The critical load of bars is 1332.3N. Clearly, the bars do not buckle during deployment and can be treated as rigid bodies. The maximum von Mises stress in the membrane is 3.53MPa, which is less than the yield stress at 3% for Kapton. The maximum stress in tendons is 63.3MPa, which is less than the yield stress of Nylon. Therefore, the membrane and tendons do not yield during system deployment.

7.5. Conclusions

In this chapter, a nonlinear control strategy of deploying tensegrity-membrane systems is studied. A nonlinear adaptive controller is designed to deploy the system from the initial configuration to the final configuration, and an H_∞ controller is implemented to stabilize the system at the deployed configuration.

Nonlinear simulations are conducted to deploy a 1-4(D) system, a 1-6(D) system, and a 2-3 system. According to the simulation results, in each case, the nonlinear adaptive controller can drive the attitudes of bars to follow the desired trajectory accurately. The membrane vibration, which is the zero dynamics of the system, is stable. During system deployment, the amplitude of the membrane vibration is small.

After control switch, the H_∞ controller stabilizes all the state variables of the system, and drives them to the equilibrium quickly. The required control inputs are small according to the simulation results.

The major limitation of the control strategy used here is that the nonlinear adaptive controller cannot directly regulate the membrane vibration during deployment, which means that this nonlinear controller cannot be used in the scenario where the membrane is required to be free from vibration during the entire deployment process. However, the membrane vibration, which is the zero dynamics of the system, is proven to be stable.

7.6. Appendix: Stability Analysis of Zero Dynamics

In Eq. (5.40), the equation of motion of $\boldsymbol{\eta}$ before the coordinate mapping is:

$$\boldsymbol{M}_{22}\ddot{\boldsymbol{\eta}} + \boldsymbol{F}_2 + \boldsymbol{M}_{12}{}^T\ddot{\boldsymbol{q}} + \boldsymbol{M}_{23}\ddot{\boldsymbol{\zeta}} = \boldsymbol{O} \tag{5.76}$$

After simplification, Eq. (5.76) can be written as:

$$\boldsymbol{M}_{\eta}\ddot{\boldsymbol{\eta}} + \left(\boldsymbol{C}_{\eta} + \boldsymbol{C}_S\left(\boldsymbol{\zeta}\right)\right)\dot{\boldsymbol{\eta}} + \left(\boldsymbol{K}_{\eta}\boldsymbol{\eta} + \boldsymbol{K}_{S1}\left(\boldsymbol{\zeta}\right) + \boldsymbol{K}_{S2}\left(\boldsymbol{\zeta}\right)\right)\boldsymbol{\eta} + \boldsymbol{b}\left(\boldsymbol{q},\boldsymbol{\zeta}\right) = \boldsymbol{O} \tag{5.77}$$

where $\boldsymbol{K}_{\eta}$ is the stiffness matrix of modal coordinates, which can be determined using Eq. (5.6). Matrices $\boldsymbol{M}_{\eta}$ and $\boldsymbol{C}_{\eta}$ can be written as:

$$\boldsymbol{M}_{\eta} = \rho\iiint_V\left(\boldsymbol{\Psi}^T\boldsymbol{\Psi}\right)dv; \quad \boldsymbol{C}_{\eta} = c\boldsymbol{M}_{\eta}; \quad \left(\boldsymbol{\Psi} = \left[\boldsymbol{\phi}_1 \quad \cdots \quad \boldsymbol{\phi}_K\right]\right) \tag{5.78}$$

Due to the orthogonality of mode shapes, i.e.

$$\iiint_V\left(\boldsymbol{\phi}_i{}^T\boldsymbol{\phi}_j\right)dv = \begin{cases} 0, & i \neq j \\ 1, & i = j \end{cases} \tag{5.79}$$

the mass matrix $\boldsymbol{M}_{\eta}$ is a diagonal matrix after integration, and all the diagonal elements are positive. Therefore, $\boldsymbol{M}_{\eta}$ is positive definite. The damping matrix $\boldsymbol{C}_{\eta}$ is introduced by the Rayleigh dissipation function expressed in Eq. (5.13), and it is positive definite. Based on numerical results, $\boldsymbol{K}_{\eta}$ is positive definite.

The matrices $\boldsymbol{C}_s$, $\boldsymbol{K}_{s1}$ and $\boldsymbol{K}_{s2}$ in Eq. (5.77) can be expressed as:

$$\begin{aligned}\boldsymbol{C}_S(\boldsymbol{\zeta}) &= 2\rho\iiint_V \left(\boldsymbol{\phi}^T \boldsymbol{S}\boldsymbol{\phi}\right) dv \\ \boldsymbol{K}_{S1}(\boldsymbol{\zeta}) &= \rho\iiint_V \left(\boldsymbol{\phi}^T \dot{\boldsymbol{S}}\boldsymbol{\phi}\right) dv \\ \boldsymbol{K}_{S2}(\boldsymbol{\zeta}) &= -\rho\iiint_V \left(\boldsymbol{\phi}^T \boldsymbol{S}^T \boldsymbol{S}\boldsymbol{\phi}\right) dv\end{aligned} \tag{5.80}$$

where $\boldsymbol{S}$ is given by:

$$\boldsymbol{S} = \begin{bmatrix} 0 & -\omega_z & \omega_y \\ \omega_z & 0 & -\omega_x \\ -\omega_y & \omega_x & 0 \end{bmatrix}; \quad \boldsymbol{\omega} = \begin{bmatrix} \omega_x & \omega_y & \omega_z \end{bmatrix}^T \tag{5.81}$$

Note that $\dot{\boldsymbol{R}}_{fe} = \boldsymbol{R}_{fe}\boldsymbol{S}$. The matrices $\boldsymbol{S}$ and $\dot{\boldsymbol{S}}$ are positive semi-definite. Therefore, $\boldsymbol{C}_S$ and $\boldsymbol{K}_{S1}$ are positive semi-definite, and $\boldsymbol{K}_{S2}$ is negative semi-definite.

The vector $\boldsymbol{b}$ in Eq. (5.77) is:

$$\boldsymbol{b}(\boldsymbol{q},\boldsymbol{\zeta}) = \iiint_V \rho\left(\boldsymbol{\phi}^T \ddot{\boldsymbol{X}}_s + 2\boldsymbol{\phi}^T \boldsymbol{S}\dot{\boldsymbol{X}}_s + \boldsymbol{\phi}^T \left(\dot{\boldsymbol{S}} - \boldsymbol{S}^T \boldsymbol{S}\right)\boldsymbol{X}_s + \boldsymbol{\phi}^T \boldsymbol{R}_{fe}{}^T \ddot{\boldsymbol{r}}_0\right) dv \tag{5.82}$$

where

$$\boldsymbol{X}_s = \begin{bmatrix} x_f + u^s & y_f + v^s & w^s \end{bmatrix}^T; \quad \boldsymbol{r}_0 = \boldsymbol{OO}_f \tag{5.83}$$

Note that $\boldsymbol{C}_s$, $\boldsymbol{K}_{s1}$, $\boldsymbol{K}_{s2}$ and $\boldsymbol{b}$ are functions of $\boldsymbol{\zeta}$ and $\boldsymbol{q}$. The coordinate mapping in Eq. (5.25) will replace the terms of $\boldsymbol{\zeta}$ by the corresponding terms of $\boldsymbol{q}$, while the structure of Eq. (5.77) and the definiteness of $\boldsymbol{C}_s$, $\boldsymbol{K}_{s1}$ and $\boldsymbol{K}_{s2}$ do not change. Therefore, after the coordinate mapping, Eq. (5.77) can be written as:

$$\boldsymbol{M}_\eta \ddot{\boldsymbol{\eta}} + \boldsymbol{C}_\eta \dot{\boldsymbol{\eta}} + \boldsymbol{K}_\eta \boldsymbol{\eta} + \boldsymbol{C}_S(\boldsymbol{q})\dot{\boldsymbol{\eta}} + \left(\boldsymbol{K}_{S1}(\boldsymbol{q}) + \boldsymbol{K}_{S2}(\boldsymbol{q})\right)\boldsymbol{\eta} + \boldsymbol{b}(\boldsymbol{q}) = \boldsymbol{O} \tag{5.84}$$

which is the equation of motion of $\boldsymbol{\eta}$ in Eq. (5.39). After evaluating Eq. (5.84) along the trajectory of $\boldsymbol{q}$, we have the zero dynamics of the system in Eq. (5.48).

After rearranging Eq. (5.84), we can express the equation of motion for $\boldsymbol{\eta}$ in the first order form:

$$\dot{\boldsymbol{x}}_{\eta} = f\left(\boldsymbol{x}_{\eta}, \boldsymbol{\delta}\right) = \left(\boldsymbol{A}_{\eta} + \tilde{\boldsymbol{A}}_{\eta}\left(t\right)\right)\boldsymbol{x}_{\eta} + \boldsymbol{\delta}\left(\boldsymbol{q}\right) \tag{5.85}$$

where

$$\begin{aligned}
\boldsymbol{x}_{\eta} &= \begin{bmatrix} \boldsymbol{\eta} \\ \dot{\boldsymbol{\eta}} \end{bmatrix}; \quad \boldsymbol{\delta}\left(\boldsymbol{q}\right) = \begin{bmatrix} \boldsymbol{O} \\ -\boldsymbol{M}_{\eta}^{-1}\boldsymbol{b}\left(\boldsymbol{q}\right) \end{bmatrix} \\
\boldsymbol{A}_{\eta} &= \begin{bmatrix} \boldsymbol{O} & \boldsymbol{I} \\ -\boldsymbol{M}_{\eta}^{-1}\boldsymbol{K}_{\eta} & -\boldsymbol{M}_{\eta}^{-1}\boldsymbol{C}_{\eta} \end{bmatrix} \\
\tilde{\boldsymbol{A}}_{\eta}\left(t\right) &= \begin{bmatrix} \boldsymbol{O} & \boldsymbol{O} \\ -\boldsymbol{M}_{\eta}^{-1}\left(\boldsymbol{K}_{S1}\left(\boldsymbol{q}\right) + \boldsymbol{K}_{S2}\left(\boldsymbol{q}\right)\right) & -\boldsymbol{M}_{\eta}^{-1}\boldsymbol{C}_{S}\left(\boldsymbol{q}\right) \end{bmatrix}
\end{aligned} \tag{5.86}$$

It is obvious that $\boldsymbol{A}_{\eta}$ is Hurwitz since $\boldsymbol{M}_{\eta}$, $\boldsymbol{C}_{\eta}$, and $\boldsymbol{K}_{\eta}$ are all positive definite, indicating that there exists a symmetric positive definite matrix $\boldsymbol{P}_{\eta}$ such that $\boldsymbol{A}_{\eta}^{T}\boldsymbol{P}_{\eta} + \boldsymbol{P}_{\eta}\boldsymbol{A}_{\eta} = -\boldsymbol{I}$ [73]. Then, for the unforced system, we can find that:

$$\begin{aligned}
&\left(\boldsymbol{A}_{\eta} + \tilde{\boldsymbol{A}}_{\eta}\left(t\right)\right)^{T}\boldsymbol{P}_{\eta} + \boldsymbol{P}_{\eta}\left(\boldsymbol{A}_{\eta} + \tilde{\boldsymbol{A}}_{\eta}\left(t\right)\right) \\
&= -\boldsymbol{I} + \tilde{\boldsymbol{A}}_{\eta}\left(t\right)^{T}\boldsymbol{P}_{\eta} + \boldsymbol{P}_{\eta}\tilde{\boldsymbol{A}}_{\eta}\left(t\right) \\
&\le \left(-1 + 2\left\|\tilde{\boldsymbol{A}}_{\eta}\left(t\right)\right\|\left\|\boldsymbol{P}_{\eta}\right\|\right)\boldsymbol{I}
\end{aligned} \tag{5.87}$$

Our numerical tests indicate that $\left\|\tilde{\boldsymbol{A}}_{\eta}\left(t\right)\right\|$ is bounded and satisfies the following condition:

$$\left\|\tilde{\boldsymbol{A}}_{\eta}\left(t\right)\right\| \le \tilde{\rho}\frac{1}{2\left\|\boldsymbol{P}_{\eta}\right\|}; \quad \left(0 < \tilde{\rho} << 1\right) \tag{5.88}$$

After inserting Eq. (5.88) into Eq. (5.87), we can get:

$$\left(\boldsymbol{A}_{\eta} + \tilde{\boldsymbol{A}}_{\eta}\left(t\right)\right)^{T}\boldsymbol{P}_{\eta} + \boldsymbol{P}_{\eta}\left(\boldsymbol{A}_{\eta} + \tilde{\boldsymbol{A}}_{\eta}\left(t\right)\right) \le -\left(1 - \tilde{\rho}\right)\boldsymbol{I} \tag{5.89}$$

Thus, according to Theorem 7.4 in [73], the unforced system is globally exponentially stable. Obviously, $f(\boldsymbol{x}_{\eta}, \boldsymbol{\delta})$ is continuously differentiable and globally Lipschitz in $(\boldsymbol{x}_{\eta}, \boldsymbol{\delta})$. Due to the uncertainty of $\boldsymbol{F}_{\boldsymbol{q}}^{*}$, Lemma 7.1 shows that $\boldsymbol{q}$ is bounded. Our numerical tests

indicate that $\boldsymbol{\delta}$ is bounded. Thus, according to Lemma 4.6 in [67], the system in Eq. (5.85) is input-to-state stable.

Chapter 8: LPV Control Design for System Deployment

8.1. Introduction

Most controllers implemented in practice are designed at a set of system operational points using the linearized model of system dynamics and are scheduled as functions of system parameters. This gain-scheduling control technique provides a cheap and simple way of carrying out nonlinear system control. Also, in the previous chapter, it is shown that, for a tensegrity-membrane system, the dynamics of bars and the attached membrane can be regulated by a linear H_∞ controller simultaneously. Therefore, a gain-scheduling controller is suitable for the control task that the bars and the attached membrane of a tensegrity-membrane system are required to be well regulated during the entire deployment process.

However, engineering insight and ad hoc rules are required for controller scheduling. Moreover, since the gain-scheduling technique relies on discretized system operational regions, the resulting controllers do not guarantee the performance and stability of the closed-loop systems at the operational points other than the design points. These issues are the major motivation of the development of linear parameter varying (LPV) control technique.

LPV control synthesis has been studied by many researchers and applied to several systems [76-79]. This control approach not only captures nonlinear behaviors of plants, but also takes advantages of the well-developed analysis methods for linear systems, leading to optimal controllers with guaranteed robustness. Moreover, LPV synthesis provides gain-scheduled controllers, which are conceptually similar to the existing

controllers used in practice. In general, no significant complexity is introduced in terms of control implementation.

This chapter addresses the LPV synthesis for a 2-3 symmetric tensegrity-membrane system. The main control objective is to deploy the 2-3 system from its initial packaged configuration to the final deployed configuration. A nonlinear simulation is conducted to test the performance of the LPV controller.

8.2. LPV State-Feedback Control

In this section, a brief overview of the key concepts of LPV control is provided. The symbol $\mathbb{R}$ represents the set of real numbers. For a compact subset $\mathcal{P} \subset \mathbb{R}^s$. The parameter variation set $\mathcal{F}_\mathcal{P}$ denotes the set of all continuously differentiable functions mapping $\mathbb{R}$ (time) into $\mathcal{P}$. The LPV model of the open-loop plant can be expressed as:

$$\begin{bmatrix} \dot{\boldsymbol{x}}(t) \\ \boldsymbol{p}(t) \end{bmatrix} = \begin{bmatrix} \boldsymbol{A}(\boldsymbol{\rho}(t)) & \boldsymbol{B}_1(\boldsymbol{\rho}(t)) & \boldsymbol{B}_2(\boldsymbol{\rho}(t)) \\ \boldsymbol{C}_1(\boldsymbol{\rho}(t)) & \boldsymbol{D}_{11}(\boldsymbol{\rho}(t)) & \boldsymbol{D}_{12}(\boldsymbol{\rho}(t)) \end{bmatrix} \begin{bmatrix} \boldsymbol{x}(t) \\ \boldsymbol{w}(t) \\ \boldsymbol{u}(t) \end{bmatrix} \tag{5.90}$$
$$\boldsymbol{\rho} \in \mathcal{F}_\mathcal{P}; \quad \boldsymbol{\rho}(t) \in \mathcal{P}$$

After applying a linear feedback controller, the closed-loop LPV system can be written as:

$$\begin{bmatrix} \dot{\boldsymbol{x}}(t) \\ \boldsymbol{p}(t) \end{bmatrix} = \begin{bmatrix} \boldsymbol{A}_{cl}(\boldsymbol{\rho}(t)) & \boldsymbol{B}_1(\boldsymbol{\rho}(t)) \\ \boldsymbol{C}_{cl}(\boldsymbol{\rho}(t)) & \boldsymbol{D}_{11}(\boldsymbol{\rho}(t)) \end{bmatrix} \begin{bmatrix} \boldsymbol{x}(t) \\ \boldsymbol{w}(t) \end{bmatrix} \tag{5.91}$$

The induced L_2-norm of the transfer function $\boldsymbol{G}_{pw}$ is defined as:

$$\left\| \boldsymbol{G}_{pw} \right\| = \sup_{\rho \in \mathcal{F}_\mathcal{P}} \sup_{\|\boldsymbol{w}\|_2 \neq 0, \boldsymbol{w} \in L_2} \frac{\|\boldsymbol{p}\|_2}{\|\boldsymbol{w}\|_2} \tag{5.92}$$

A key result in LPV synthesis is the following theorem [79]:

Theorem 8.1. For all $\boldsymbol{\rho}(t) \in \mathcal{P}$ and the open-loop LPV plant in Eq. (5.90), the matrix $\boldsymbol{A_{cl}}$ is stable and there is an upper bound γ on $\|\boldsymbol{G_{pw}}\|$, if there exists a symmetric positive-definite matrix $\boldsymbol{X}(\boldsymbol{\rho})$, such that:

$$\begin{bmatrix} \boldsymbol{H}\left(\boldsymbol{\rho}(t)\right) & \boldsymbol{X}\left(\boldsymbol{\rho}(t)\right)\boldsymbol{B}_1\left(\boldsymbol{\rho}(t)\right) & \boldsymbol{C}_{cl}{}^T\left(\boldsymbol{\rho}(t)\right) \\ \boldsymbol{B}_1{}^T\left(\boldsymbol{\rho}(t)\right)\boldsymbol{X}\left(\boldsymbol{\rho}(t)\right) & -\gamma \boldsymbol{I} & \boldsymbol{D}_{11}{}^T\left(\boldsymbol{\rho}(t)\right) \\ \boldsymbol{C}_{cl}\left(\boldsymbol{\rho}(t)\right) & \boldsymbol{D}_{11}\left(\boldsymbol{\rho}(t)\right) & -\gamma \boldsymbol{I} \end{bmatrix} \prec \boldsymbol{O} \tag{5.93}$$

where

$$\boldsymbol{H}\left(\boldsymbol{\rho}(t)\right) = \boldsymbol{A}_{cl}{}^T\left(\boldsymbol{\rho}(t)\right)\boldsymbol{X}\left(\boldsymbol{\rho}(t)\right) + \boldsymbol{X}\left(\boldsymbol{\rho}(t)\right)\boldsymbol{A}_{cl}\left(\boldsymbol{\rho}(t)\right) + \frac{d\boldsymbol{X}\left(\boldsymbol{\rho}(t)\right)}{dt} \tag{5.94}$$

Theorem 8.1 is the generalization of the well-known Bounded Real Lemma for LPV systems. After applying a state-feedback controller $\boldsymbol{u} = \boldsymbol{K}(\boldsymbol{\rho}(t))\boldsymbol{x}$, the matrix $\boldsymbol{A_{cl}}$ can be written as: $\boldsymbol{A_{cl}}(\boldsymbol{\rho}(t)) = \boldsymbol{A}(\boldsymbol{\rho}(t)) + \boldsymbol{B_2}(\boldsymbol{\rho}(t))\boldsymbol{K}(\boldsymbol{\rho}(t))$. Pre-multiplying and post-multiplying Eq. (5.93) by $\boldsymbol{L} = \text{diag}(\boldsymbol{X}(\boldsymbol{\rho}(t))^{-1}, \boldsymbol{I}, \boldsymbol{I})$ and letting $\boldsymbol{X}(\boldsymbol{\rho}(t))^{-1} = \boldsymbol{P}(\boldsymbol{\rho}(t))$, $\boldsymbol{K}(\boldsymbol{\rho}(t))\boldsymbol{X}(\boldsymbol{\rho}(t))^{-1} = \boldsymbol{Q}(\boldsymbol{\rho}(t))$ yield:

$$\begin{bmatrix} \boldsymbol{H}_1\left(\boldsymbol{\rho}(t)\right) & \boldsymbol{B}_1\left(\boldsymbol{\rho}(t)\right) & \boldsymbol{F}^T\left(\boldsymbol{\rho}(t)\right) \\ \boldsymbol{B}_1{}^T\left(\boldsymbol{\rho}(t)\right) & -\gamma \boldsymbol{I} & \boldsymbol{D}_{11}{}^T\left(\boldsymbol{\rho}(t)\right) \\ \boldsymbol{F}\left(\boldsymbol{\rho}(t)\right) & \boldsymbol{D}_{11}\left(\boldsymbol{\rho}(t)\right) & -\gamma \boldsymbol{I} \end{bmatrix} \prec \boldsymbol{O} \tag{5.95}$$

where

$$\begin{aligned} \boldsymbol{H}_1\left(\boldsymbol{\rho}(t)\right) &= \boldsymbol{A}\left(\boldsymbol{\rho}(t)\right)\boldsymbol{P}\left(\boldsymbol{\rho}(t)\right) + \boldsymbol{B}_2\left(\boldsymbol{\rho}(t)\right)\boldsymbol{Q}\left(\boldsymbol{\rho}(t)\right) \\ &\quad + \boldsymbol{P}\left(\boldsymbol{\rho}(t)\right)\boldsymbol{A}^T\left(\boldsymbol{\rho}(t)\right) + \boldsymbol{Q}^T\left(\boldsymbol{\rho}(t)\right)\boldsymbol{B}_2{}^T\left(\boldsymbol{\rho}(t)\right) - \frac{d\boldsymbol{P}\left(\boldsymbol{\rho}(t)\right)}{dt} \\ \boldsymbol{F}\left(\boldsymbol{\rho}(t)\right) &= \boldsymbol{C}_1\left(\boldsymbol{\rho}(t)\right)\boldsymbol{P}\left(\boldsymbol{\rho}(t)\right) + \boldsymbol{D}_{12}\left(\boldsymbol{\rho}(t)\right)\boldsymbol{Q}\left(\boldsymbol{\rho}(t)\right) \end{aligned} \tag{5.96}$$

Then, the state-feedback gain is $\boldsymbol{K}(\boldsymbol{\rho}(t)) = \boldsymbol{Q}(\boldsymbol{\rho}(t))\boldsymbol{P}(\boldsymbol{\rho}(t))^{-1}$.

The LMI in Eq. (5.95) imposes an infinite number of constraints on matrices $\boldsymbol{P}(\boldsymbol{\rho}(t))$ and $\boldsymbol{Q}(\boldsymbol{\rho}(t))$, since these constraints must be satisfied for all trajectories of $\boldsymbol{\rho}(t)$ in the set $\mathcal{P}$. In this work, this problem is relaxed by discretizing the set $\mathcal{P}$ via a gridding approach [79].

8.3. Control Design

The LPV control design is based on the control-oriented model discussed in Chapter 6. The generalized coordinates in Eq. (5.17) are used since membrane deflections can be measured easily.

The design objectives for the LPV controller are characterized as follows:

1. *Deployment requirement*: the locations and attitudes of bars, $\boldsymbol{q}$, track the desired trajectory, $\boldsymbol{q}_d$. In this work, $\boldsymbol{q}_d$ is treated as a time-varying signal. Note that, for some symbols representing functions, we neglect the corresponding independent variables for simplicity. For example, we use $\boldsymbol{q}_d$ instead of $\boldsymbol{q}_d(t)$ in this chapter.
2. *Membrane vibration requirement*: the dynamics of the attached membrane can be stabilized.
3. *Tendon requirement*: the tendon rest-lengths do not exceed the corresponding tendon lengths, i.e. tendon lengths are treated as control limits and tendons do not go slack.

According to Eq. (3.19) and Eq. (3.20), for the symmetric tensegrity-membrane system studied in this chapter, the declination angle and azimuth angle of each bar are expressed as:

$$\theta_{ij} = \theta; \quad (i = 1,2,...M; \quad j = 1,2,...N)$$
$$\psi_{ij} = \begin{cases} \psi + \sigma_i + 2j\pi/N; & (i = 1,2,...M; \quad j = 1,2,...N) \\ \psi + \sigma_i; & (i = 1,2,...M; \quad j = N) \end{cases} \tag{5.97}$$

Clearly, Eq. (5.97) indicates that θ and ψ can specify symmetric equilibrium configurations. Based on this definition, it can be easily found that θ and ψ correspond to the declination angle and azimuth angle of bar b_{13}, i.e. $\theta = \theta_{13}$ and $\psi = \psi_{13}$. Therefore, the two scheduling parameters are chosen as: $\rho_1 = \theta_{13}$ and $\rho_2 = \psi_{13}$. Since ρ_1 and ρ_2 are state variables, the 2-3 tensegrity-membrane system is represented by a quasi-LPV model. It is known that methods used to design LPV controllers can be applied to quasi-LPV models [80].

For this example, the parameter space $\mathcal{P}$ is defined as: $\mathcal{P} = \rho_1 \times \rho_2$ = [63°, 77.32°]×[7.5°, 9.21°]. The parameter space is gridded by 6×3 points, which correspond to 18 system symmetric equilibriums. The discretized parameter space is: $\mathcal{P}_\mathcal{D}$ = {63°, 65.86°, 68.73°, 71.59°, 74.45°, 77.32°}×{7.5°, 8.36°, 9.21°}. After linearizing Eq. (5.27) at these equilibriums, we get 18 linearized first order models, whose state variables can be expressed as: $\boldsymbol{x}_z = [\tilde{\boldsymbol{z}}^T \quad \dot{\tilde{\boldsymbol{z}}}^T]^T$. Note that we use the same symbols to represent the variables in the nonlinear equations of motion and the corresponding perturbed variables in the linearized models. There should be no confusion with this notation.

According to the system interconnection shown in Figure 8.1, the exogenous input vector $\boldsymbol{w}$ can be written as: $\boldsymbol{w} = [\boldsymbol{q}_d^T \quad \boldsymbol{n}_d^T]^T$, where $\boldsymbol{n}_d$ is the perturbation at the input of the plant. The regulated output vector $\boldsymbol{p}$ can be expressed as: $\boldsymbol{p} = [\boldsymbol{e}_r^T \quad \boldsymbol{e}_u^T]^T$. Note that the definition of generalized coordinates in Eq. (5.18) indicates that there exists a constant matrix $\boldsymbol{T}_{qx}$ such that $\boldsymbol{q} = \boldsymbol{T}_{qx}\boldsymbol{x}_z$.

The tracking error $\boldsymbol{e_q}$ is defined as: $\boldsymbol{e_q} = \boldsymbol{q_d} - \boldsymbol{q}$. To achieve trajectory tracking using state-feedback control, the integral of $\boldsymbol{e_q}$ with respect to time is introduced as an additional state variable. Thus, the state vector of the LPV model is:

$$\boldsymbol{x} = \begin{bmatrix} \boldsymbol{x_z}^T & \tilde{\boldsymbol{e}}_{\boldsymbol{q}}^{\,T} \end{bmatrix}^T; \quad \tilde{\boldsymbol{e}}_{\boldsymbol{q}} = \int \boldsymbol{e_q} dt \tag{5.98}$$

The matrices $\boldsymbol{P}(\boldsymbol{\rho}(t))$ and $\boldsymbol{Q}(\boldsymbol{\rho}(t))$ in (5.95) are parameterized as:

$$\boldsymbol{P}\left(\boldsymbol{\rho}(t)\right) = \boldsymbol{P_0} + \rho_1 \boldsymbol{P_1} + \rho_2 \boldsymbol{P_2}; \quad \boldsymbol{Q}\left(\boldsymbol{\rho}(t)\right) = \boldsymbol{Q_0} + \rho_1 \boldsymbol{Q_1} + \rho_2 \boldsymbol{Q_2} \tag{5.99}$$

The bounds for the rates of ρ_1 and ρ_2 are set to be ±10 deg/s. According to the method introduced in [78], the resulting LMIs are solved on the set $\mathcal{P}_{\mathcal{D}}$.

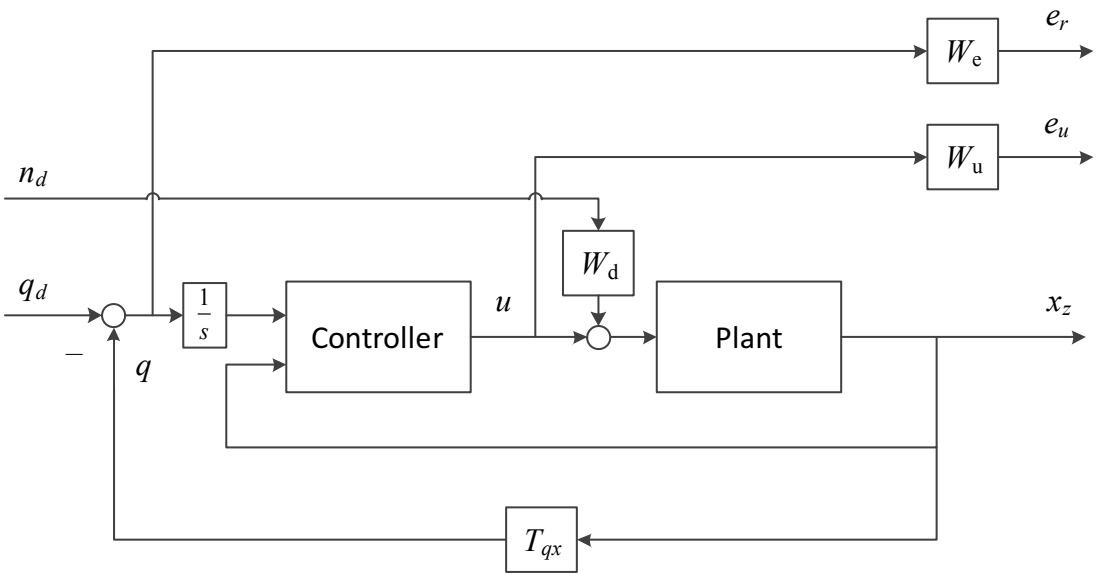

Figure 8.1. System interconnection

The weighting functions used in this work are:

1. To specify the tracking error performance, the weighting function $\boldsymbol{W_e}$ is defined as: $\boldsymbol{W_e} = 0.5\boldsymbol{I}$. Note that, since we focus on state-feedback control in this chapter,

this constant weighting function is used in order not to introduce other state variables.

2. The weighting function $\boldsymbol{W}_{\mathbf{u}}$ is adjusted throughout the design process to prevent the tendons from going slack in simulations. The final weight chosen for the design is: $\boldsymbol{W}_{\mathbf{u}} = 0.05\boldsymbol{I}$.
3. For the disturbance at the input of the plant, the weight $\boldsymbol{W}_{\mathbf{d}}$ is chosen as: $\boldsymbol{W}_{\mathbf{d}} = 0.001\boldsymbol{I}$.

CVX is used to solve the LMIs in (5.95) and the resulting controller has an induced norm $\|\boldsymbol{G}_{pw}\| < 4.18$.

8.4. Simulation Results

For the 2-3 tensegrity-membrane system, the membrane is made of Kapton. The materials for bars and tendons are chosen as wood and Nylon, respectively. The material and geometrical parameters of the system are listed in Table 8.1.

As discussed previously, θ and ψ can specify symmetric equilibrium configurations. Thus, once the reference angles, θ_r and ψ_r, are specified, the reference signal $\boldsymbol{q}_d$ can be determined according to Eq. (5.97) by letting $\theta = \theta_r$ and $\psi = \psi_r$. In this work, the reference angles are generated according to the following equations:

$$\begin{aligned} &\ddot{\theta}_r(t) + 2\xi_r\omega_r\dot{\theta}_r(t) + \omega_r^2\theta_r(t) = \omega_r^2\theta_e; \quad \left(\theta_r(0) = \theta_0; \quad \dot{\theta}_r(0) = 0\right) \\ &\psi_r(t) = \psi_0 \end{aligned} \tag{5.100}$$

where $\xi_r = 1$, $\omega_r = 0.3$, $\theta_0 = 77.32°$, $\theta_e = 63°$, and $\psi_0 = 8.36°$. The subscripts 0 and e indicate the values of the initial and final configurations, respectively. Clearly, the value

of θ_r is generated by a critically damped second order system with the settling time of 15.83 seconds.

Table 8.1. Material and geometrical parameters of the 2-3 system

Components	Parameters	
Membrane	Young's Modulus (E)	165 MPa
	Density (ρ)	1400 kg/m^3
	Thickness (h)	51 μm
	Poisson's ratio (μ)	0.34
Bar	Density	800 kg/m^3
	Length	1.8 m
	Cross section diameter	30 mm
Tendon	Young's Modulus	2 GPa
	Cross section diameter	0.254 mm

The deflections of three points, w_1, w_2, and w_3, on the membrane are monitored. The locations of these three points are characterized by:

$$\begin{aligned} w_1 &= w^r\left(x_f, y_f\right)\Big|_{x_f=0.866\ (\mathrm{m});\ \ y_f=0.5\ (\mathrm{m})} \\ w_2 &= w^r\left(x_f, y_f\right)\Big|_{x_f=1.30\ (\mathrm{m});\ \ y_f=0.75\ (\mathrm{m})} \\ w_3 &= w^r\left(x_f, y_f\right)\Big|_{x_f=0.433\ (\mathrm{m});\ \ y_f=0.75\ (\mathrm{m})} \end{aligned} \tag{5.101}$$

The representative responses of bars, i.e. the responses of bar b_{11} and bar b_{21}, are shown in Figure 8.2. Note that, since the desired deployment trajectory passes through a set of symmetric equilibriums, the responses of other bars in the first and the second stage

are similar to the responses of bars b_{11} and b_{21}, respectively. As mentioned previously, x_{ij}, y_{ij}, and z_{ij} represent the x, y, and z locations of the bar lower end A_{ij}. In Figure 8.2, we can observe that the responses of θ_{11}, ψ_{11}, x_{21}, y_{21}, z_{21}, θ_{21}, and ψ_{21} follow the desired trajectory. No significant tracking error is observed during system deployment. Therefore, it can be concluded that the LPV controller can make the closed-loop system track the desired trajectory accurately.

Transverse deflections of the three points, w_1, w_2, and w_3, are shown in Figure 8.3. It can be seen that the LPV controller can well regulate the behavior of the membrane. There is no significant vibration introduced during system deployment and the maximum deflection is less than 1 mm.

The representative tendon rest-length variations are shown in Figure 8.4. It can be seen that the rest-lengths do not exceed the control limits, which are the corresponding tendon lengths. In other words, tendons do not go slack during system deployment. Note that, for tendon S_{2j}, the tendon elongation is small during system deployment, so the difference between the tendon lengths and rest-lengths shown in Figure 8.4 may not be seen clearly.

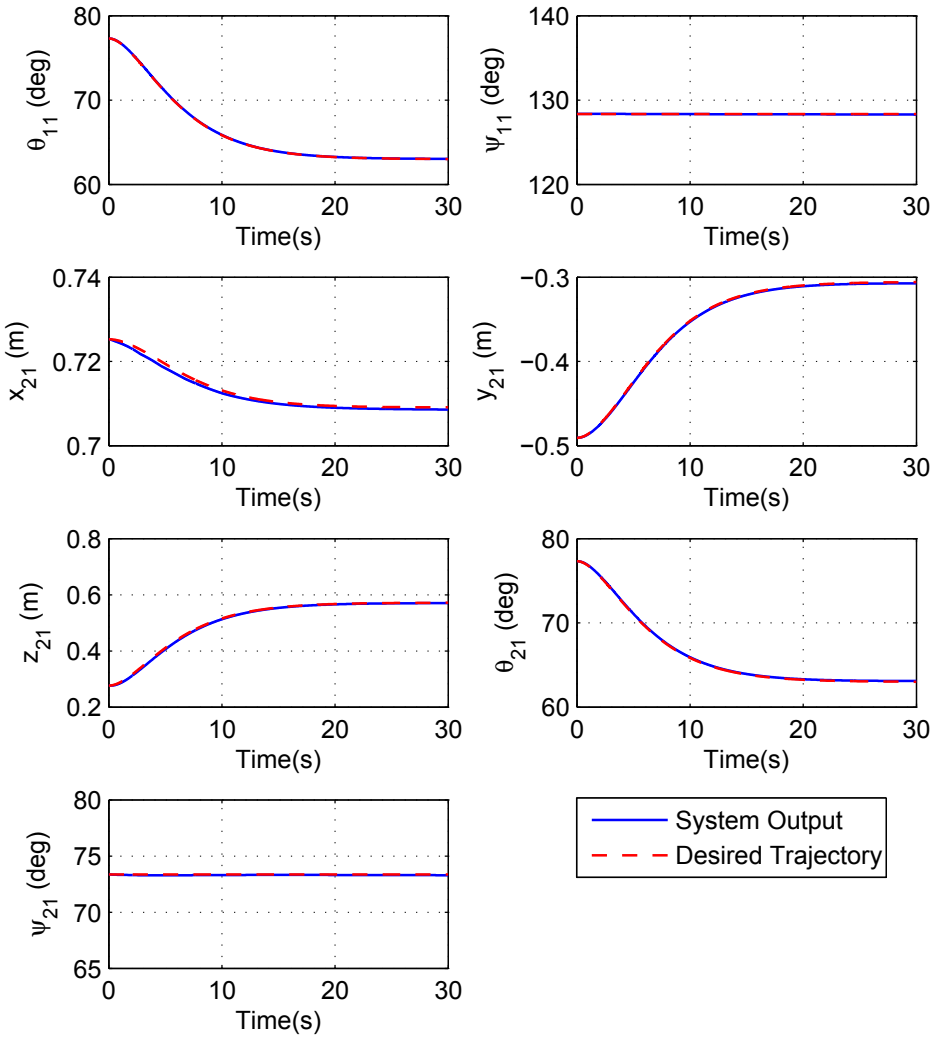

Figure 8.2. Responses of locations and attitudes of bar b_{11} and bar b_{21}

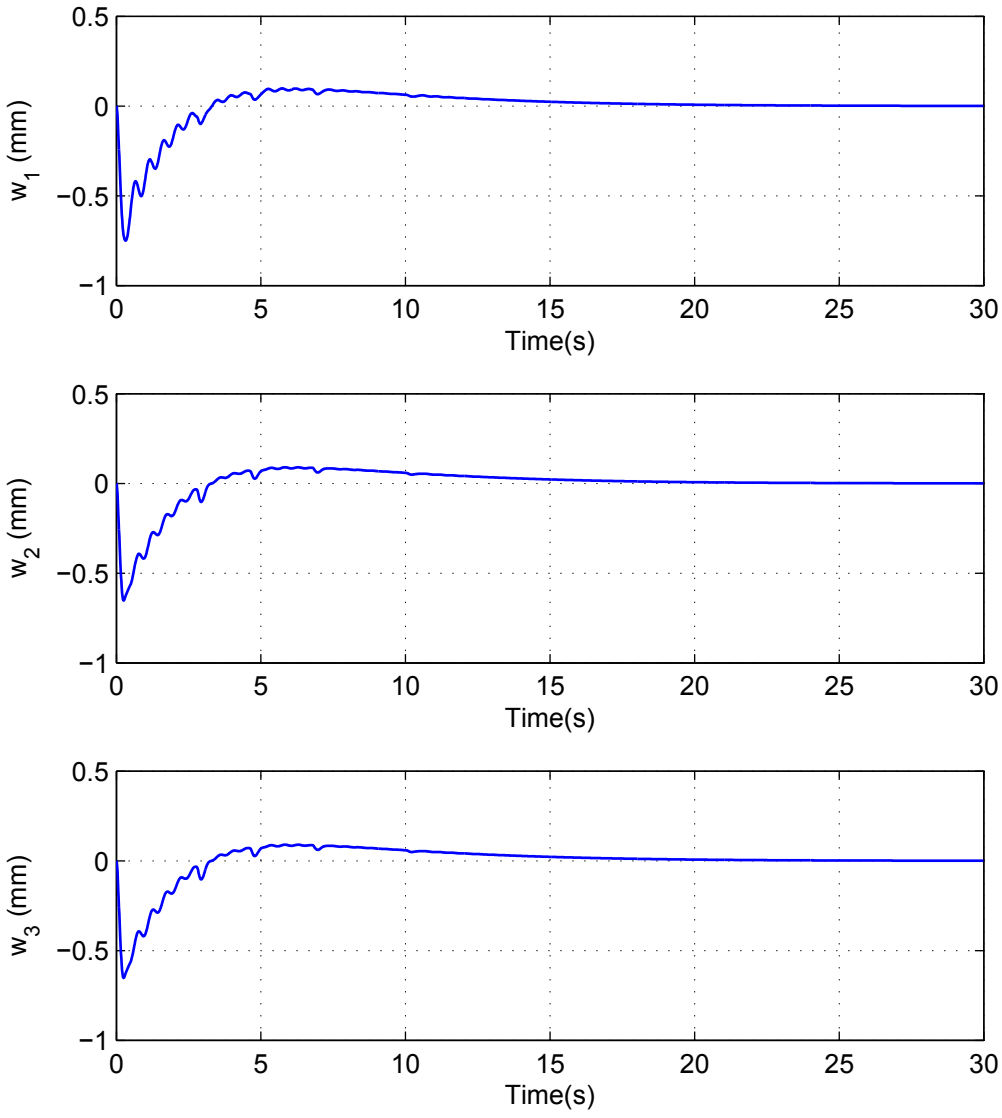

Figure 8.3. Transverse vibrations of three points on the membrane

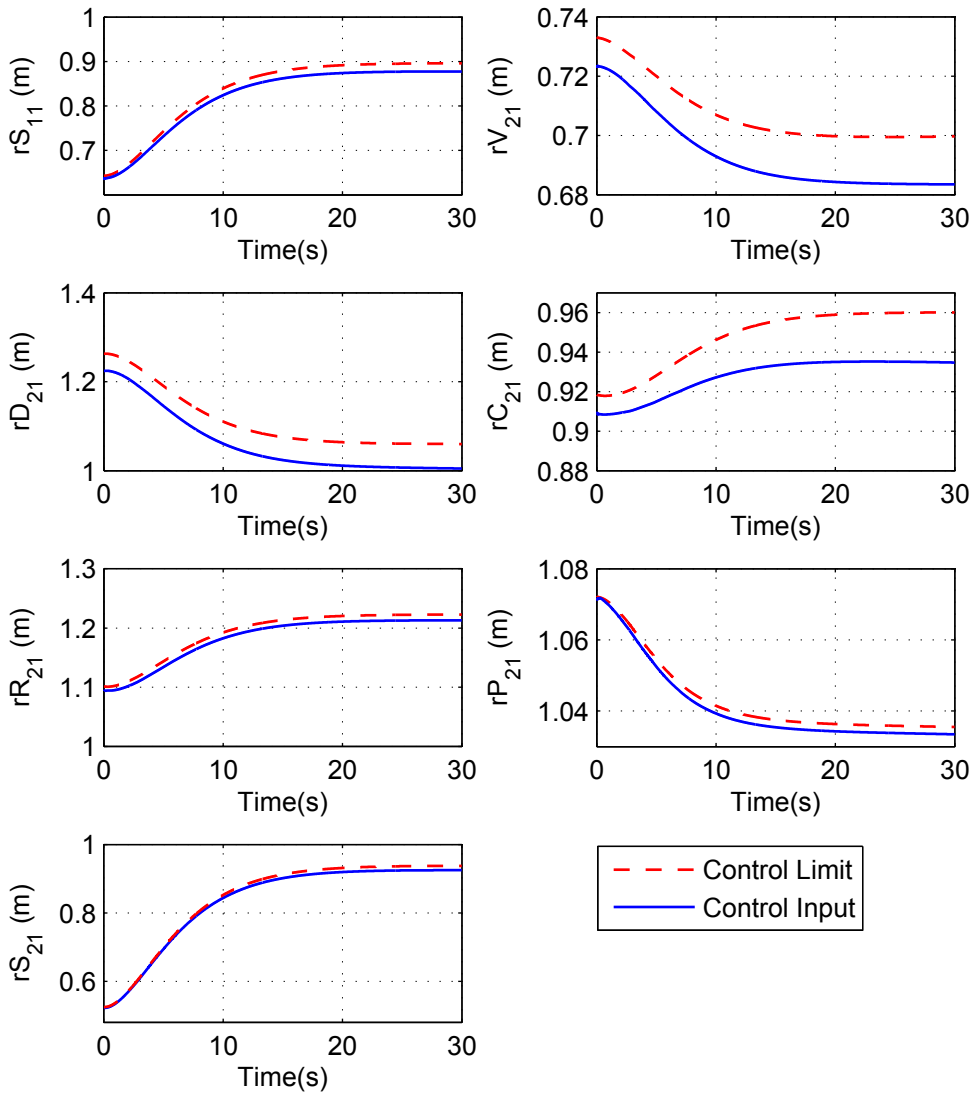

Figure 8.4. Representative tendon rest-length variations

Snapshots of system deployment process are shown in Figure 8.5. We can observe that the tensegrity-membrane system experiences significant shape changes during deployment, while the membrane transverse deflections cannot be clearly seen. This coincides with the results shown in Figure 8.3, where the magnitude of the membrane transverse deflections is less than 1 mm.

During system deployment, the peak compressive load on bars during deployment is 4.7N. The critical load of bars is 1332.3N according to Euler's column buckling formula in Eq. (5.31). It can be concluded that the bars do not buckle during deployment and can be treated as rigid bodies. The maximum von Mises stress in the membrane is 3.53MPa. It is less than the yield stress at 3% for Kapton which is 61MPa [74]. The maximum stress in tendons is 89.3MPa. It is less than the yield stress of Nylon which is 94.8MPa [75]. Therefore, the membrane and tendons do not yield during system deployment.

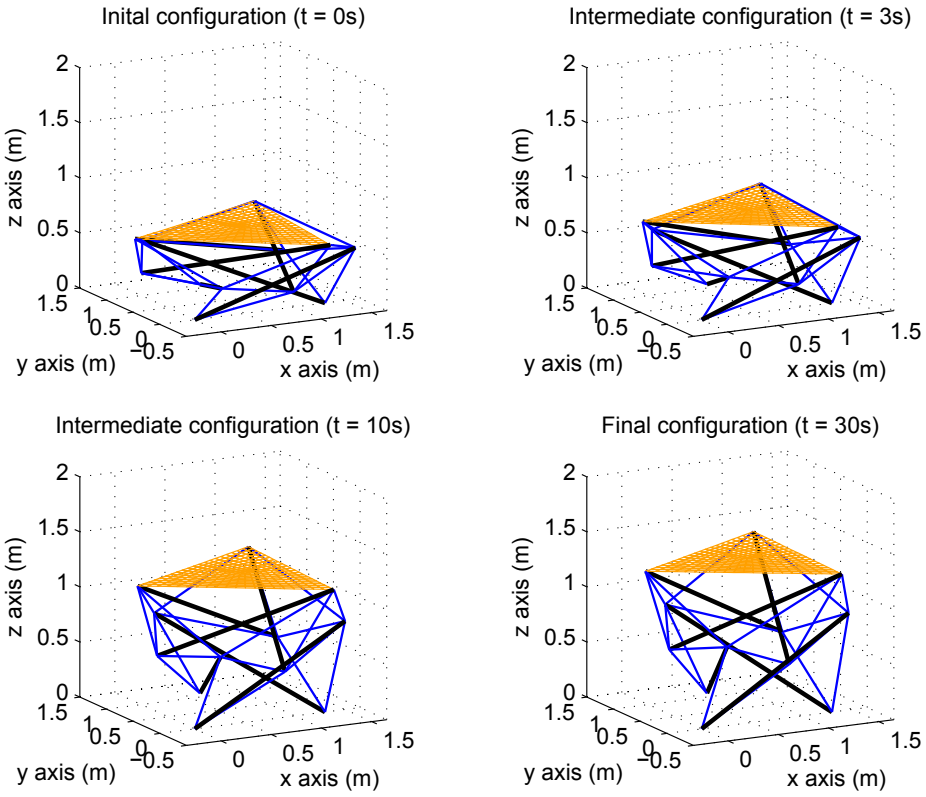

Figure 8.5. Deployment sequence of the 2-3 system

8.5. Conclusions

In this chapter, the details of designing a LPV controller for a tensegrity-membrane system are presented. The system interconnection and weighting functions are

determined based on the control design objectives. The resulting LPV controller is implemented to deploy the tensegrity-membrane system from its initial packaged configuration to its final deployed configuration.

Simulation results illustrate that the LPV controller performs well in making the closed-loop system track the desired trajectory and the tracking error is small. No significant membrane vibration is introduced during system deployment. Moreover, the tendon rest-lengths are less than the corresponding tendon lengths, indicating that tendons do not go stack during system deployment. Clearly, all the control design objectives are met. These results and observations show that it is feasible to use a LPV controller to control and deploy such a complex system.

Chapter 9: Conclusions and Future Work

9.1. Conclusions

The objectives of this work are to study the mechanics of tensegrity-membrane systems and to conduct control design for these deployable systems. Since tensegrity-membrane systems are prestressed systems, a systematic equilibrium finding method is developed to determine the equilibrium conditions of general tensegrity-membrane systems. It is found that the resulting equilibrium conditions can be significantly simplified if tensegrity-membrane systems are in symmetric configurations. Analytical equilibrium conditions can be determined for one-stage symmetric systems, i.e. 1-*N* systems and 1-*N*(D) systems.

The dynamics of tensegrity-membrane systems is studied using two different methods. The nonlinear finite element method is first used to model the systems, yielding two models: the shell-beam-cable model and the membrane-truss-cable model. For these two nonlinear finite element models, tensegrity-membrane systems are treated as nonlinear flexible multibody systems and all systems components, i.e. membranes, bars, and tendons, are treated as deformable bodies. The shell-beam-cable model is developed without specific modeling assumptions for system components, while assumptions for membranes and bars are used for the membrane-truss-cable model to simplify the modeling problem. Then, a control-oriented model is developed based on three key assumptions: 1) geometric nonlinearities of membranes are ignored; 2) bars are rigid bodies; 3) the dynamics of tendons is ignored. The techniques of modeling linear flexible

multibody systems are employed, such as defining floating reference frames, introducing constraints, and implementing modal coordinates.

Numerical analysis of tensegrity-membrane systems is conducted using the three mathematical models. Static analysis of tensegrity-membrane systems is first performed using the shell-beam-cable model in order to check the equilibrium finding method proposed in this work. The shell-beam-cable model is also used to conduct the mesh convergence study. Based on the results of the static analysis and the mesh convergence analysis, modal analysis and free vibration analysis are then performed. Analysis results given by the three models are in good agreement, indicating that the modeling assumptions introduced for the membrane-truss-cable model and the control-oriented model do not cause significant errors in the test scenarios used in this work.

Two control strategies are designed for system deployment. The first control strategy is to use a nonlinear adaptive controller to deploy the system from the initial configuration to the final configuration and to stabilize the whole system using a linear H_∞ controller. The second control strategy is designed based on the state-feedback LPV control theory. A gridding approach is used to discretize the region of system equilibriums and the LPV controller is determined over on this discretized region. The control-oriented model is used for control design and simulation. Simulation results show that these two control strategies can successfully control tensegrity-membrane systems to track the desired deployment trajectories.

9.2. Future Work

This work is the first comprehensive study on modeling and control of tensegrity-membrane systems. Important results related to system statics and dynamics are

presented and discussed. However, there are still problems related to system mechanics that could be addressed in future work. First, the mechanism of wrinkles generated on membranes is not considered in this work. It is known that membrane wrinkling is an important problem in membrane design and analysis. Thus, the influence of membrane wrinkling on the mechanics of tensegrity-membrane systems deserves careful examination. Second, the gravitational field is ignored in this work and it is assumed that the systems are installed on fixed bases. Considering that tensegrity-membrane systems are expected to be implemented in space applications, the mechanics of tensegrity-membrane systems in orbit should be studied. Third, the equilibrium finding method proposed in this work is an approach for system preliminary design. Problems related to the detailed design of tensegrity-membrane systems require further effort.

The control strategies designed in this work are shown to be effective. It should be pointed out that there are several limitations of the control laws discussed in this work, which could be addressed in future work. First, the nonlinear adaptive controller used in this work can regulate the attitudes of bars during system deployment, but the behavior of the membrane cannot be controlled. Thus, a linear H_∞ controller is designed to stabilize the whole system at the final configuration. Clearly, a nonlinear controller which can control the bars and the membrane of a tensegrity-membrane system simultaneously could significantly improve the control performance during system deployment. Second, the state-feedback LPV control theory is used to design the LPV controller. As a result, it is equivalent to assume that all system state variables can be measured accurately and the measurement noise is not taken into account. Clearly, these two assumptions are not

always acceptable in practice. Therefore, further effort should be spent on the design of an output-feedback LPV controller for tensegrity-membrane systems.

References

[1] Cassapakis, C., and Thomas, M., "Inflatable Structures Technology Development Overview", *Proceedings of Space Programs and Technologies Conference*, Huntsville, Alabama, 1995.

[2] Pappa, R.S., Lassiter, J.O., and Ross, B.P., "Structural Dynamics Experimental Activities in Ultralightweight and Inflatable Space Structures", *Journal of Spacecraft and Rockets*, Vol. 40, No. 1, 2003, pp.15-23.

[3] Ruggiero, E. J. and Inman, D. J., "Gossamer Spacecraft: Recent Trends in Design, Analysis, Experimentation, and Control", *Journal of Spacecraft and Rockets*, Vol. 43, No. 1, 2006, pp. 10-24.

[4] Greschik, G. and Mikulas, M. M., "Design Study of a Square Solar Sail Architecture", *Journal of Spacecraft and Rockets*, Vol. 39, No. 5, 2002, pp. 653-661.

[5] Mikulas, M. M. and Adler, A. L., "Rapid Structural Assessment Approach for Square Solar Sails Including Edge Support Cords", *Proceedings of the 44th AIAA/ASME/ASCE/AHS Structures, Structural Dynamics, and Materials Conference*, Norfolk, Virginia, 2003.

[6] Kukathasan, S. and Pellegrino, S., "Vibration of Prestressed Membrane Structures in Air", *Proceedings of the 43rd AIAA/ASME/ASCE/AHS/ASC Structures, Structural Dynamics, and Materials Conference and Exhibit*, Denver, Colorado, 2002.

[7] Kukathasan, S. and Pellegrino, S., "Nonlinear Vibration of Wrinkled Membranes", *Proceedings of the 44th AIAA/ASME/ASCE/AHS/ASC Structures, Structural Dynamics, and Materials Conference*, Norfolk, Virginia, 2003.

[8] Adetona, O., Keel, L. H., Horta, L. G., Cadogan, D. P., Sapna, G. H., and Scarborough, S. E., "Description of New Inflatable/Rigidizable Hexapod Structure Testbed for Shape and Vibration Control", *Proceedings of the 43rd AIAA/ASME/ASCE/AHS/ASC Structures, Structural Dynamics, and Materials Conference*, Denver, Colorado, 2002.

[9] Adetona, O., Horta, L. G., Taleghani, B. K., Blandino, J. R., and Woods, K. J., "Vibration Studies of an Inflatable/Rigidizable Hexapod Structure with a Tensioned Membrane", *Proceedings of the 44th AIAA/ASME/ASCE/AHS Structures, Structural Dynamics, and Materials Conference*, Norfolk, Virginia, 2003.

[10] Berger, K. T., Horta, L. G., and Taleghani, B. K., "Static Testing of an Inflatable/Rigidizable Hexapod Structure", *Proceedings of the 45th AIAA Structures, Structural Dynamics and Material Conference*, Palm Springs, California, 2004.

[11] Leipold, M., Eiden, M., Garner, C. E., Herbeck, L., Kassing, D., Niederstadt, T., and Unckenbold, W., "Solar Sail Technology Development and Demonstration", *Acta Astronautica*, Vol. 52, No. 2, 2003, pp. 317-326.

[12] Fang, H., Lou, M., Hsia, L., and Leung, P., "Catenary Systems for Membrane Structures", *Proceedings of the 42nd AIAA/ASME/ASCE/AHS/ASC Structures,*

Structural Dynamics, and Materials Conference and Exhibit, Seattle, Washington, 2001.

[13] Leipold, M., Runge, H., and Sickinger, C., "Large SAR Membrane Antennas with Lightweight Deployable Booms", *Proceedings of the 28th ESA Antenna Workshop on Space Antenna Systems and Technologies, ESA/ESTEC*, 2005.

[14] Pellegrino, S., "Deployable Membrane Reflectors", *Proceedings of the 2nd World Engineering Congress*, 2002.

[15] Pollard, E. L., Murphey, T. W., and Sanford, G. E., "Experimental and Numerical Analysis of a DECSMAR Structure's Deployment and Deployed Performance", *Proceedings of the 48th AIAA/ASME/ASCE/AHS/ASC Structures, Structural Dynamics, and Materials Conference*, Honolulu, Hawaii, 2007.

[16] Mejia-Ariza, J. M., Murphey, T. W., and Dumm, H. P., "Deployable Trusses based on Large Rotation Flexure Hinges", *Journal of Spacecraft and Rockets*, Vol. 47, No. 6, 2010, pp. 1053-1062.

[17] Murphey, T., Jeon, S., Biskner, A., and Sanford, G., "Deployable Booms and Antennas using Bi-Stable Tape-Springs", *Proceedings of the 24th Annual AIAA/USU Conference on Small Satellites*, Logan, Utah, 2010.

[18] Footdale, J. N., Murphey, T. W., and Peterson, M., "Design and Testing of Self-Deploying Membrane Optic Support Structure using Rollable Composite Tape Springs", *Proceedings of the 54th AIAA/ASME/ASCE/AHS/ASC Structures, Structural Dynamics, and Materials Conference*, Boston, Massachusetts, 2013.

[19] Wagner, R., "On the Design Process of Tensile Structures", *Textile Composites and Inflatable Structures*, Springer Netherlands, 2005, pp. 1-16.

[20] Moncrieff, E., "Systems for Lightweight Structure Design: the State-of-the-Art and Current Developments", *Textile Composites and Inflatable Structures*, Springer Netherlands, 2005, pp. 17-28.

[21] Gründig, L., Ströbel, D., and Singer, P., "Recent Developments in the Analytical Design of Textile Membranes", *Textile Composites and Inflatable Structures*, Springer Netherlands, 2005, pp. 29-45.

[22] Huntington, C. G., *The Tensioned Fabric Roof*, ASCE Publications, 2004.

[23] Zolesi V. S., Ganga P. L., Scolamiero L., Micheletti A., Podio-Guidugli P., Tibert G., Donati A., and Ghiozzi M., "On an Innovative Deployment Concept for Large Space Structures", *Proceedings of the 42nd International Conference on Environmental Systems*, San Diego, California, 2012.

[24] Freeland, R. E., "Significance of the Inflatable Antenna Experiment Technology", *Proceedings of the 39th AIAA/ASME/ASCE/AHS/ASC Structures, Structural Dynamics, and Materials Conference*, Long Beach, California, 1998.

[25] Ingber , D. E., "Cellular Basis of Mechanotransduction", *Biological Bulletin*, Vol. 194, No. 3, 1998, pp. 323-327.

[26] Canadas, P., Laurent, V. M., Oddou, C., Isabey, D., and Wendling, S., "A Cellular Tensegrity Model to Analyse the Structural Viscoelasticity of the Cytoskeleton", *Journal of Theoretical Biology*, Vol. 218, No. 2, 2002, pp. 155-173.

[27] Vera, C., Skelton, R. E., Bossens, F., and Sung, L. A., "3-D Nanomechanics of an Erythrocyte Junctional Complex in Equibiaxial and Anisotropic Deformations", *Annals of Biomedical Engineering*, Vol. 33, No. 10, 2005, pp. 1387-1404.

[28] Skelton, R. E., "Structural Systems: a Marriage of Structural Engineering and System Science", *Journal of Structural Control*, Vol. 9, No. 2, 2002, pp. 113-133.

[29] Fraternali, F., Senatore, L., and Daraio, C., "Solitary Waves on Tensegrity Lattices", *Journal of Mechanics and Physics of Solids*, Vol. 60, No. 6, 2012, pp. 1137-1144.

[30] Fraternali, F., Carpentieri, G., and Amendola, A., "On the Mechanical Modeling of the Extreme Softening/Stiffening Response of Axially Loaded Tensegrity Prisms", *Journal of Mechanics and Physics of Solids*, Vol. 74, 2015, pp. 136-157.

[31] Sultan, C., "Tensegrity Deployment using Infinitesimal Mechanisms", *International Journal of Solids and Structures*, Vol. 51, 2014, pp. 3653-3668.

[32] Tibert, A. G., "Deployable Tensegrity Structures for Space Applications", Ph.D. Dissertation, Department of Mechanics, Royal Institute of Technology, Sweden, 2002.

[33] Sultan, C. and Skelton, R. E., "Deployment of Tensegrity Structures", *International Journal of Solids and Structures*, Vol. 40, No. 18, 2003, pp. 4637-4657.

[34] Skelton, R. E. and Oliveira, M. C., *Tensegrity Systems*, Springer, 2009.

[35] Sultan, C., "Tensegrity: Sixty Years of Art, Science, and Engineering", *Advances in Applied Mechanics*, Vol. 43, 2009, pp. 69-145.

[36] Tibert, A. G. and Pellegrino, S., "Deployable Tensegrity Masts", *Proceedings of the 44th AIAA/ASME/ASCE/AHS Structures, Structural Dynamics, and Materials Conference*, Norfolk, Virginia, 2003.

[37] Tibert, A. G. and Pellegrino, S., "Deployable Tensegrity Reflectors for Small Satellites", *Journal of Spacecraft Rockets*, Vol. 39, No. 5, 2002, pp. 701-709.

[38] Sultan, C., Corless, M., and Skelton, R. E., "Tensegrity Flight Simulator", *Journal of Guidance, Control, and Dynamics*, Vol. 23, No. 6, 2000, pp. 1055-1064.

[39] Sunny, M., Sultan, C., and Kapania, R. K., "Optimal Energy Harvesting from a Membrane Attached to a Tensegrity Structure", *AIAA Journal*, Vol. 52, No. 2, 2014, pp. 307-319

[40] Fuller, R. B., *Tensile-Integrity Structures*, U.S. Patent 3,063,521, 1962.

[41] Calladine, C. R., "Buckminster Fuller's 'Tensegrity' Structures and Clerk Maxwell's Rules for the Construction of Stiff Frames", *International Journal of Solids and Structures*, Vol. 14, No. 2, 1978, pp. 161-172.

[42] Sadao, S., "Fuller on Tensegrity", *International Journal of Space Structures*, Vol. 11, No. 1, 1996, pp. 37–42.

[43] Greenwood, D. T., *Principles of Dynamics*, Upper Saddle River, NJ: Prentice-Hall, 1988.

[44] Shames, I. H., and Dym, C. L., *Energy and Finite Element Methods in Structural Mechanics*, Taylor & Francis, 1995.

[45] Bauchau, O., *Flexible Multibody Dynamics*, Springer, 2011.

[46] Turner, M.R., Clough, R., Martin, H. and Topp, L., "Stiffness and Deflection Analysis of Complex Structures", *Journal of Aeronautical Sciences*, Vol. 23, No. 9, 1956, pp. 805-823.

[47] Oden, J. T., *Finite Elements of Nonlinear Continua*, McGraw-Hill, New York, 1972.

[48] Bathe, K. J., *Finite Element Procedures*, Upper Saddle River, NJ: Prentice-Hall, 1996.

[49] Belytschko, T., Liu, W. K., Moran, B., and Elkhodary, K., *Nonlinear Finite Elements for Continua and Structures*, John Wiley & Sons, 2013.

[50] Levy, S., "Bending of Rectangular Plates with Large Deflections", *NACA Report* 737, 1942.

[51] Epstein, M. and Murray, D. W., "Large Deformation In-Plane Analysis of Elastic Beams", *Computers & Structures*, Vol. 6, No. 1, 1976, pp.1-9.

[52] Crisfield, M. A., *Nonlinear Finite Element Analysis of Solids and Structures, Volume 1: Essentials*, John Wiley & Sons, 1991.

[53] Weaver, Jr., W., Timoshenko, S. P., and Young, D. H., *Vibration Problems in Engineering*, New Jersey: John Wiley & Sons, 1990.

[54] Soedel, W., *Vibrations of Shells and Plates, 3rd Edition*. CRC Press, 2004.

[55] Wehage, R. A. and Haug, E. J., "Generalized Coordinate Partitioning for Dimension Reduction in Analysis of Constrained Dynamic Systems", *Journal of Mechanical Design*, Vol. 104, No. 1, 1982, pp.247-255.

[56] Singh, R. P. and Likins, P. W., "Singular Value Decomposition for Constrained Dynamical Systems", *Journal of Applied Mechanics*, Vol. 52, No. 4, 1985, pp.943-948.

[57] Kim, S. S. and Vanderploeg, M. J., "QR Decomposition for State Space Representation of Constrained Mechanical Dynamic Systems", *Journal of Mechanisms, Transmissions, and Automation in Design*, Vol. 108, No. 2, 1986, pp.183-188.

[58] Masarati, P., Morandini, M., and Fumagalli, A., "Control Constraint of Underactuated Aerospace Systems", *Journal of Computational and Nonlinear Dynamics*, Vol. 9, No. 2, 2014, pp.021014.

[59] Park, K. C., "An Improved Stiffly Stable Method for Direct Integration of Nonlinear Structural Dynamic Equations". *Journal of Applied Mechanics*, Vol. 42, No. 2, 1975, pp. 464-470.

[60] Spong, M. W., "Underactuated Mechanical Systems", *Control Problems in Robotics and Automation*, Springer, 1998.

[61] Spong, M. W., "The Swing Up Control Problem for the Acrobat", *Control Systems, IEEE*, Vol. 15, No. 1, 1995, pp. 49-55.

[62] Spong, M. W., "Energy Based Control of a Class of Underactuated Mechanical Systems", *Proceedings of the 1996 IFAC World Congress*, 1996,

[63] De Luca, A., Mattone, R., and Oriolo, G., "Stabilization of an Underactuated Planar 2R Manipulator", *International Journal of Robust and Nonlinear Control*, Vol. 10, No. 4, 2000, pp.181-198.

[64] Tuan, L. A., Lee, S. G., Ko, D. H., and Nho, L. C., "Combined Control with Sliding Mode and Partial Feedback Linearization for 3D Overhead Cranes", *International Journal of Robust and Nonlinear Control*, Vol. 24, No. 18, 2014, pp.3372-3386.

[65] Barron, A. R., "Universal Approximation Bounds for Superpositions of a Sigmoidal Function", *Information Theory, IEEE Transactions on*, Vol. 39, No. 3, 1993, pp. 930-945.

[66] Pomet, J. B. and Praly, L., "Adaptive Nonlinear Regulation: Estimation from the Lyapunov Equation", *Automatic Control, IEEE Transactions on*, Vol. 37, No. 6, 1992, pp.729-740.

[67] Khalil, H. K., *Nonlinear Systems*, Upper Saddle River, NJ: Prentice-Hall, 2002.

[68] Gahinet, P. and Apkarian, P., "A Linear Matrix Inequality Approach to H_∞ Control", *International Journal of Robust and Nonlinear Control*, Vol. 4, No. 4, 1994, pp. 421-448.

[69] Iwasaki, T. and Skelton, R. E., "All Controllers for the General H_∞ Control Problem: LMI Existence Conditions and State Space Formulas", *Automatica*, Vol. 30, No. 8, 1994, pp. 1307-1317.

[70] Chilali, M. and Gahinet, P., "H_∞ Design with Pole Placement Constraints: an LMI Approach", *Automatic Control, IEEE Transactions on*, Vol. 41, No. 3, 1996, pp.358-367.

[71] Ogata, K., *Modern Control Engineering, 5th Edition*, Upper Saddle River, NJ: Prentice-Hall, 2010.

[72] Shannon, C. E., "Communication in the Presence of Noise", *Proceedings of the IRE*, Vol. 37, No. 1, 1949, pp. 10-21.

[73] Rugh, W. J., *Linear System Theory*, Upper Saddle River, NJ: Prentice-Hall, 1996.

[74] DuPont, "Kapton® HN General-Purpose Polyimide Film", http://www.dupont.com/content/dam/assets/products-and-services/membranes-films/assets/DEC-Kapton-HN-datasheet.pdf

[75] Cambridge University, "Materials Data Book", http://www-mdp.eng.cam.ac.uk/web/library/enginfo/cueddatabooks/materials.pdf

[76] Tan, W., Packard, A. K., and Balas, G. J., "Quasi-LPV Modeling and LPV Control of a Generic Missile", *Proceedings of the American Control Conference*, 2000.

[77] Balas, G. J., Fialho, I., Pack, A., Renfrow, J., and Mullaney, C., "On the Design of LPV Controllers for the F-14 Aircraft Lateral-Directional Axis during Powered Approach", *Proceedings of the American Control Conference*, 1997

[78] Wu, F., Packard, A., and Balas, G. J., "LPV Control Design for Pitch-Axis Missile Autopilots", *Proceedings of the 34th IEEE Conference on Decision and Control*, 1995.

[79] Wu, F., "Control of Linear Parameter Varying Systems", Ph.D. Dissertation, Department of Mechanical Engineering, University of California at Berkeley, 1995.

[80] Tan, W., "Applications of Linear Parameter-Varying Control Theory", MS Thesis, Department of Mechanical Engineering, University of California at Berkeley, 1997.